Title
Photonics and exceptional degeneracy points in optical waveguides for lasing, nonlinear conversion, and chirality applications

ISBN
9798291579329

Author
Herrero Parareda, Albert

Publication Date
2025-08-29

UNIVERSITY OF CALIFORNIA,
IRVINE

Theory and Applications of Exceptional Points of Degeneracy in Optical Waveguides and Optical Chirality

DISSERTATION

submitted in partial satisfaction of the requirements
for the degree of

DOCTOR OF PHILOSOPHY

in Electrical and Computer Engineering

by

Albert Herrero-Parareda

Dissertation Committee:
Professor Filippo Capolino, Chair
Professor Maxim Shcherbakov
Professor Ozdal Boyraz

2025

DEDICATION

TO MY MOM, WHO TAUGHT ME TO BE CURIOUS.

TABLE OF CONTENTS

LIST OF FIGURES

LIST OF TABLES

Page

ACKNOWLEDGMENTS

First, I would like to express my appreciation and gratitude to my PhD advisor, Professor Filippo Capolino, for supporting me during the past five years. I have learnt a lot of things from Professor Capolino that helped to develop my way of thinking such as asking myself questions to understand, being precise when I speak or write, and being patient to learn new topics and improve things. Without the guidance and persistent help of Prof. Capolino, this dissertation would not have been possible. In addition, I would like to thank the committee members, Professor Maxim Shcherbakov and Professor Ozdal Boyraz who have provided helpful feedback and insights.

I would like to thank my colleagues who were involved in research. I thank Nathaniel Furman with whom I collaborated to do the brunt of the research enclosed herein.

I thank Dr. Tarek Mealy who helped me a lot during my first year of PhD. I thank Dr. Alireza Nikzamir, Dr. Kasra Rouhi and Dr. Robert Marosi for working with me and for supporting me. I am happy and appreciative of that teamwork. I thank also all my lab mates Miguel Melo Saavedra, Ben Bradshaw and Amin Hakimi.

I am also grateful for the funding, the Air Force Office of Scientific Research (AFOSR) and the National Science Foundation. The research work in this dissertation was mainly supported by the AFOSR under Award FA9550-18-1-0355 and Award FA9550-20-1-0409.

Most importantly, I am deeply and sincerely grateful to my Dad who was always there for me at every step and gave me the strength and confidence to pursue my goals. I would like to express my thanks to my elder brothers Miquel Herrero Parareda and Lluís Herrero Parareda for their continuous support and care.

VITA

Albert Herrero-Parareda

EDUCATION

Doctor of Philosophy in Electrical and Computer Eng. **2025**
University of California, Irvine *Irvine, California, USA*

Masters of Science in Electronics and Communications Eng. **2023**
University of California, Irvine *Irvine, California, USA*

Bachelor of Science in Engineering Physics **2020**
Universitat Politècnica de Catalunya *Barcelona, Spain*

RESEARCH EXPERIENCE

Graduate Research Assistant **2020–2025**
University of California, Irvine *Irvine, California*

TEACHING EXPERIENCE

Teaching Assistant **2020–2025**
University of California, Irvine *Irvine, California*

JOURNAL PUBLICATIONS

[1] **Albert Herrero-Parareda**, et al., "Lasing at a stationary inflection point," in *Optical Materials Express*, vol. 13, no. 5, pp. 1290–1306, 2023.

K. Z. Abramovich, N. Furman, **Albert Herrero-Parareda**, F. Capolino, and J. Scheuer, "Low-threshold lasing with frozen mode regime and stationary inflection point in three coupled waveguide structure," in *Physical Review A*, vol. 108, no. 6, p. 063504, 2023.

Albert Herrero-Parareda and F. Capolino, "The combination of the azimuthally and radially polarized beams: Helicity and momentum densities, generation, and optimal chiral light," in *Advanced Photonics Research*, vol. 2300265, 2024.

N. Furman, **Albert Herrero-Parareda**, I. Vitebskiy, R. Gibson, B. Thompson, and F. Capolino, "Impact of fabrication disorder on lasing near a stationary inflection point," in *Journal of the Optical Society of America B*, vol. 42, no. 4, pp. 879–889, 2025.

Albert Herrero-Parareda, N. Perez, F. Capolino, and D. Preece, "Experimental generation of optimally chiral azimuthally-radially polarized beams," in *Nanophotonics*, 2025.

A. Nikzamir, **Albert Herrero-Parareda**, N. Furman, Benjamin Bradshaw, et al., "Array oscillator in coupled waveguides with nonlinear gain and radiation resistances saturating at exceptional point," in *arXiv preprint arXiv:2501.14978*, 2025.

DDFB Laser [7] TWG2RA [8] DBE-SHG

CONFERENCE & PREPRINT PUBLICATIONS

[9] **Albert Herrero-Parareda**, N. Furman, T. Mealy, A. Nikzamir, and F. Capolino, "Lasing with multimode guided waves with exceptional degeneracy," in *SPIE Active Photonic Platforms (APP)*, PC121961M, 2022.

A. Nikzamir, N. Furman, **Albert Herrero-Parareda**, T. Mealy, and F. Capolino, "Exceptional points of degeneracy in waveguides with or without loss and gain," in *The Sixteenth International Congress on Artificial Materials for Novel Wave Phenomena (Metamaterials)*, vol. 326, 2022.

Albert Herrero-Parareda and F. Capolino, "Optimally chiral optical trapping," in *SPIE Optical Trapping and Optical Micromanipulation XX*, vol. 12649, p. 96, 2023.

N. Furman, **Albert Herrero-Parareda**, Bradley Thompson, et al., "Impact of waveguide imperfections on lasing near a stationary inflection point," in *SPIE Active Photonic Platforms (APP)*, vol. 12647, p. 44, 2023.

N. Furman, **Albert Herrero-Parareda**, and F. Capolino, "A leaky wave antenna made of two TLs with exceptional point degeneracy," in *The 17th European Conference on Antennas and Propagation (EUCAP)*, pp. 1–3, 2023.

Albert Herrero-Parareda, N. Furman, and F. Capolino, "Beyond the regular band edges: lasing near a degenerate band edge," in *Solid State Lasers XXXIII: Technology and Devices*, PC1286406, 2024.

Albert Herrero-Parareda and F. Capolino, “Optimally chiral light-matter interactions: generalizing structured light illumination in an isotropic medium,” in *Complex Light and Optical Forces XVIII*, PC129010N, 2024.

A. Nikzamir, **Albert Herrero-Parareda**, N. Furman, Benjamin Bradshaw, et al., “Array oscillator in coupled waveguides with nonlinear gain and radiation resistances saturating at exceptional point,” in *arXiv preprint arXiv:2501.14978*, 2025.

ABSTRACT OF THE DISSERTATION

Theory and Applications of Exceptional Points of Degeneracy in Optical Waveguides and Optical Chirality

By

Albert Herrero-Parareda

Doctor of Philosophy in Electrical and Computer Engineering

University of California, Irvine, 2025

Professor Filippo Capolino, Chair

Exceptional points of degeneracy (EPDs), where multiple eigenmodes of a system coalesce in both their eigenvalues and eigenvectors, offer a powerful framework for engineering electromagnetic wave behavior. This dissertation explores the design, analysis, and numerical validation of integrated photonic structures that operate near EPDs to enable novel and enhanced functionalities in lasers, slow-light devices, and chiral light–matter interaction.

We first demonstrate that a silicon-based asymmetric serpentine optical waveguide (ASOW) supports a third-order EPD known as a stationary inflection point (SIP). Using coupled-mode theory and the transfer matrix method, we derive the SIP conditions and confirm its existence through full-wave simulations. The SIP regime enables the so-called frozen mode, characterized by low group velocity and enhanced energy storage, with group delay and quality factor scaling cubically with the waveguide length.

Building on this platform, we explore lasing near the SIP in active periodic waveguides. We show that the threshold gain scales inversely with the cube of the cavity length, significantly reducing the lasing threshold compared to regular band edge lasers, even in the presence of small losses. Further, we investigate a new class of distributed feedback (DFB) lasers based on a double-grating structure that supports a fourth-order EPD, the degenerate band edge

(DBE). These degenerate DFB (DDFB) lasers exhibit threshold gain scaling with the inverse fifth power of the cavity length and enable single-frequency lasing without mirrors.

In a related study, we leverage the degenerate band edge (DBE) condition to enhance second harmonic generation (SHG) in a double-grating periodic waveguide. By operating the structure near the DBE at the fundamental frequency and incorporating second-order nonlinear materials, we achieve strong field enhancement and slow-light effects that significantly boost the nonlinear conversion efficiency. The high density of states and prolonged interaction enabled by the DBE condition lead to improved energy transfer to the second harmonic that is extracted vertically. This work demonstrates the potential of DBE-based photonic structures for compact and highly efficient frequency conversion in integrated nonlinear optical devices.

We also investigate structured light beams engineered for optimal chiral interaction. We investigate and characterize the azimuthally-radially polarized beam (ARPB), which achieves maximal helicity density for a given energy density through longitudinal field components. Theoretical analysis and closed-form expressions are presented, followed by experimental realization using spatial light modulators. We validate that the ARPB's helicity can be precisely tuned by a single phase parameter, enabling full control over its chiral behavior.

Altogether, this work highlights the potential of dispersion-engineered waveguides operating near EPDs for high-performance photonic devices and the construction of structured light beams, offering new avenues for integrated lasers, slow-light components, nonlinear frequency conversion devices, and sensing.

Chapter 1

Introduction

1.1 Motivation of This Work

The advancement of photonic integrated waveguides, delay lines, and solid-state lasers is central to the development of high-speed telecommunication systems, precision sensing platforms, and efficient nonlinear optical devices. This dissertation proposes a new class of integrated photonic structures that exploit exceptional points of degeneracy (EPDs) in lossless and gainless waveguides to achieve unprecedented performance enhancements. EPDs are spectral degeneracies where both eigenvalues and eigenvectors coalesce. They enable unique dispersion engineering capabilities that can result in ultra-slow light propagation, enhanced field confinement, and strong light–matter interaction [3, 4, 5].

Applications leveraging EPDs have been explored across various fields, including solid-state oscillators [6, 7, 8], electron-beam-based oscillators and amplifiers [9, 10], compact delay lines [11], narrowband antennas [12], pulse compressors [13], and high-Q resonators and lasers [14, 15, 16, 17, 18, 19].

Most state-of-the-art designs supporting EPDs in the literature rely on extensive and often time-consuming geometry optimization. In contrast, this work develops a systematic framework for designing waveguides and optical cavities that support high-order EPDs. New figures of merit, theoretical tools, and modeling approaches are introduced to identify and analyze the degeneracy conditions. These EPD-based platforms are then applied to active devices, such as ultra-low-threshold lasers operating near stationary inflection points and degenerate band edges, and to nonlinear photonic structures for efficient harmonic generation. This approach connects fundamental wave physics with practical device implementations and establishes EPDs as a powerful paradigm for integrated photonic technologies.

1.2 History of Exceptional Points of Degeneracy (EPD)

An exceptional point of degeneracy (EPD) is a point in a system's parameter space where both eigenvalues and eigenvectors coalesce simultaneously [20, 21, 22, 23]. The concept of an exceptional point (EP) was discussed in Kato's seminal work on perturbation theory [23]. Unlike traditional degeneracies that refer only to the coincidence of eigenvalues (such as wavenumbers), EPDs involve the collapse of both eigenvalues and the corresponding eigenvectors, leading to a stronger form of degeneracy that governs polarization and modal behavior [24]. Because of this high-order mode mixing, the term "degeneracy" is added to "exceptional point" to form EPD.

In non-Hermitian systems, real eigenvalue spectra can still emerge when the system exhibits parity-time (PT) symmetry [25]. A system is PT symmetric if the combined PT operator commutes with the Hamiltonian [26, 27], where parity reflects spatial coordinates and time reversal swaps gain and loss [28]. The point at which the eigenvalues transition from real to complex, as gain/loss or coupling parameters are varied, marks an EPD. This spectral transition is often referred to as the PT-symmetry breaking point.

In optics, PT symmetry is realized when the complex refractive index satisfies $n(x) = n^*(x)$, where x is a spatial coordinate and * denotes complex conjugation [29, 30, 31, 32]. EPDs also appear in bifurcation theory as branch points in control parameter space, where multiple eigenvalue branches merge [33, 34, 35, 36]. These concepts have further been observed in multilayer waveguiding systems, where EPDs serve as critical points governing wave propagation [37, 38, 39, 40, 41].

The simplest example of an EPD in a waveguide's modal propagation is a second-order degeneracy that occurs at the modal cutoff frequency of a uniform waveguide [42]. Second-order EPDs also appear at the regular band edge (RBE) of lossless periodic waveguides and photonic crystals [43, 44, 45]. Higher-order EPDs, such as third- and fourth-order degeneracies in lossless and gainless waveguides, are of particular interest due to the contributions of evanescent modes. For instance, a third-order EPD corresponds to a stationary inflection point (SIP) [5, 46], and a fourth-order EPD is known as a degenerate band edge (DBE) [17, 4]. These points arise in the modal dispersion relation $\omega(k)$, and their order m determines the flatness near the degeneracy, where $(\omega - \omega_m) \propto (k - k_m)^m$ [47].

The SIP is of special interest because it supports the so-called frozen mode, a wave with vanishing group velocity and enhanced field amplitude away from the edges of the waveguide [3, 4]. Unlike the RBE and DBE, which are adjacent to photonic bandgaps, the SIP exists in a band without gaps. The SIP and the DBE both supports resonances that are fundamentally different than those of the RBE due to their hybrid nature involving both propagating and evanescent modes [48]. Furthermore, the SIP condition is relatively insensitive to small changes in geometry, making it practical for real-world implementations [49].

Theoretical predictions of SIPs and DBEs have been confirmed in both microwave and optical domains. SIPs have been studied in microwave waveguides [50, 51, 52] and in optical waveguides [53, 54, 11]. Experimental demonstrations of frozen modes at microwave frequencies have been reported in reciprocal microstrip waveguides [52]. Similarly, DBEs have been validated experimentally using periodic metallic waveguides [55], microstrip platforms [56, 57], and at optical frequencies in Silicon waveguides [58].

Therefore, these two kinds of EPDs (i.e., the SIP and the DBE) have been demonstrated in systems that are entirely lossless and gainless, particularly through dispersion engineering in periodic coupled-mode waveguides and photonic crystals [43, 5, 56]. Key works have introduced EPD designs that realize second-, third-, and fourth-order degeneracies; RBEs, SIPs, and DBEs, respectively [43, 44, 59, 60, 61, 62, 53, 63, 64, 65]. The combination of theoretical modeling, symmetry-based design, and experimental validation has brought the SIP and the DBE from mathematical abstraction into the realm of practical device design.

This dissertation builds upon this body of work by implementing SIPs and DBEs in realistic photonic waveguides and applying them to conceive new low-threshold lasers and nonlinear devices with enhanced conversion efficiency. Through this, it contributes to advancing the understanding and practical use of EPDs in integrated photonics.

1.3 Applications of EPDs at optical frequencies

EPDs at optical frequencies in lossless and gainless waveguides open new avenues for designing devices with extreme electromagnetic responses. One of the primary applications is in time-delay systems and optical buffers, where the near-zero group velocity near an SIP enables significant enhancement in group delay and quality factor. This behavior can be exploited in optical delay lines, resonators, and photonic circuits requiring compact, high-performance delay elements [3, 4]. The scaling of the group delay with waveguide length near an EPD far exceeds that of conventional slow-light structures, making EPD-based systems particularly attractive for integrated photonic timing and sensing applications.

Another major application is in the development of solid-state lasers with enhanced performance. DBEs have been used to conceive laser cavities with significantly lower lasing thresholds [66] and possibly higher power efficiencies by tailoring the density of states and enhancing light–matter interaction [18, 67]. In particular, the degenerate band edge (DBE) condition has been shown to support single-mode lasing with high power efficiency due to the anomalously high Q-factor and field enhancement at the degeneracy point [68, 19].

Additionally, we show that the DBE enables a new regime for efficient nonlinear optical conversion. The field enhancement and slow-light effect near EPDs lead to a significant increase in the effective interaction length and intensity [5, 66], making them ideal for second harmonic generation (SHG) and other nonlinear optical processes. The ability to engineer phase matching and modal overlap near EPDs allows for compact, integrated nonlinear devices with greatly improved conversion efficiencies.

These unique features make EPDs a powerful design paradigm for a wide range of photonic components operating at optical frequencies, with promising applications in communications, sensing, and quantum computing.

1.4 Interplay between optical and molecular chirality

Besides investigating EPDs in photonic integrated circuits, this dissertation also includes advancements in the field of optical chirality.

The chirality of electromagnetic fields can be quantified through the helicity density, a pseudoscalar field property directly connected to the projection of the spin angular momentum onto the direction of propagation [69]. For monochromatic light, the time-averaged helicity density h is given by [70, 71]

$$h = \frac{1}{2\omega c}\Im(\mathbf{E}\cdot\mathbf{H}^*), \tag{1.1}$$

where $\mathbf{E}$ and $\mathbf{H}$ are the electric and magnetic field phasors, ω is the angular frequency, and c is the speed of light in vacuum.

Importantly, the magnitude of the helicity density is fundamentally bounded by the local energy density u of the field as $|h| \leq u/\omega$ [70]. Light fields that reach this upper bound are said to be *optimally chiral* (OCL), and they represent the most effective polarization configuration for maximizing chiral light-matter interactions.

While circularly polarized light (CPL) is the most common example of optimally chiral light, structured beams offer additional design flexibility. In particular, beams with purely longitudinal electric and magnetic fields at specific locations can achieve optimal chirality without relying on circular polarization in the transverse plane [72, 70]. This characteristic is especially advantageous for probing or manipulating chiral particles along the beam axis, where conventional CPL would fail.

In this dissertation, we focus on the azimuthally-radially polarized beam (ARPB), a superposition of an azimuthally polarized beam (APB) and a radially polarized beam (RPB), which has been shown to exhibit optimal chirality when an appropriate phase shift is introduced between its components [73, 74]. The ARPB is of particular interest because its transverse fields vanish along the beam axis, where the helicity density stems purely from its longitudinal fields, enabling highly selective interaction with chiral particles placed along the beam center.

Furthermore, we experimentally demonstrated the generation of optimally chiral ARPBs using vectorial beam shaping techniques, achieving precise control over their helicity density. By varying a single beam parameter, we showed the ability to continuously tune the helicity density across its full range of possible values, a feature that holds great potential for applications in sensing, enantioselective trapping, and nanoscale manipulation of chiral matter.

1.5 Organization of the Dissertation and Contents

The dissertation is organized into Chapters that involve the theory and applications of dispersion engineering in optical devices, plus two additional chapters on the optimally chiral ARPB.

Chapter 2: In this chapter, we advance the theory of lasers operating near a stationary inflection point in active periodic optical waveguides. Using the ASOW structure from previous work [1], we demonstrate that lasing near the SIP leads to a threshold gain that scales as the inverse cube of the waveguide length. We show this scaling persists even with small distributed losses, and that lasing near an SIP is preferred over lasing near the closest RBE. The chapter also analyzes the impact of gain and loss on the dispersion properties and coalescence of eigenmodes near the SIP, demonstrating the robustness of SIP-induced frozen modes under practical (imperfect) conditions.

Chapter 3: In this chapter, we present a systematic methodology for designing slow-light photonic integrated circuits with a frozen mode based on a special kind of EPD of order three, i.e., the SIP. This is realized through three-way coupled waveguides with lateral gratings operating at telecommunication wavelengths. We provide two designs and analyze sensitivity to geometric perturbations. We have fabricated a periodic waveguide with integrated tapers and demonstrate good agreement with full-wave simulations. These findings confirm the feasibility of integrating SIP-based delay functionalities in standard silicon photonic platforms.

Chapter 4: In this chapter, we advance concepts in lasing in a double grating photonic structure that operates near an exceptional point of degeneracy (EPD) of fourth order. The so-called degenerate DFB (DDFB) laser relies on lasing near an exceptional degeneracy involving four different Bloch eigenmodes, known as a degenerate band edge (DBE), to achieve a robust single-frequency lasing regime. A DDFB photonic cavity operating close to the DBE frequency is shown to display a large quality factor that scales with the fifth power of the cavity length. Upon the inclusion of gain, the DDFB cavity displays an exceptionally low lasing threshold that scales as the inverse of the fifth power of the double grating length, i.e., $\alpha_{D,th} \propto 1/N^5$, where N is the number of waveguide unit cells making the mirrorless cavity. The work proposed here shows a path to single-frequency lasing mode using a mirrorless cavity with minimal device footprint. The DDFB laser is very attractive for various applications including communications, sensing, and spectroscopy.

Chapter 5: In this chapter, an anomalous flat band dispersion provided by a degenerate band edge (DBE) of optical modes in a double grating structure is used to enhance second harmonic generation (SHG) extracted vertically. The DBE is a fourth-order exceptional point of degeneracy (EPD) in a lossless and gainless waveguide, characterized by the coalescence of four eigenmodes that establish a frozen mode in a cavity. At a DBE resonance, the cavity's quality factor scales as $Q \propto N^5$, where N is the number of gratings' unit cells. In our numerical experiments, we observe the peak fundamental-field intensity in the edge-excited cavity scaling as $I_1 \propto N^{3.6}$. This leads to a highly efficient SHG process that is radiated vertically from the cavity without the need for phase matching, with a conversion efficiency scaling as $\eta \propto N^{8.27}$. The resulting theoretical conversion efficiency per-unit-length squared is comparable to the literature. These results establish DBE-based waveguides as promising platforms for miniaturized efficient nonlinear photonic devices.

Chapter 6: In this chapter, we explore the electromagnetic properties of structured light beams engineered for optimal chiral light–matter interaction. Specifically, we study the superposition of azimuthally and radially polarized beams forming an azimuthally-radially polarized beam (ARPB), which supports purely longitudinal electric and magnetic fields on its axis. We introduce a concise formalism to describe the ARPB and derive analytical expressions for its field quantities, including energy, momentum, and helicity densities. We demonstrate that, under optimal conditions, the ARPB achieves maximal helicity density at a given energy density, qualifying it as "optimally chiral light." The beam's chiral characteristics (which are present in the longitudinal direction as well as in the transverse plane) enable highly selective probing of the longitudinal chiral polarizability of nanoparticles. We conclude the chapter by proposing experimental setups for the generation of ARPBs with tunable chirality and orbital angular momentum.

Chapter 7: In this chapter, done as a collaboration with Dr. Preece and Nico Perez, we experimentally demonstrate and characterize the structured light beam studied in Chapter 7, the azimuthally-radially polarized beam (ARPB). Using a dual–spatial light modulator setup, we generate paraxial ARPBs and validate their helicity properties across the transverse plane. We show that the helicity density of the beam can be precisely tuned by adjusting a single phase parameter, enabling continuous control over the beam's chirality. Our findings confirm that optimal chirality (defined by a maximum helicity-to-energy density ratio) is achieved for specific configurations, and that circular polarization is sufficient but not necessary for optimal chirality. These results advance the experimental realization of self-dual and optimally chiral light fields, with strong implications for optical manipulation and sensing of chiral matter.

Chapter 2

Lasing at an Stationary Inflection Point

In this chapter, we demonstrate that lasing can occur near a stationary inflection point (SIP) in a periodic optical waveguide, leading to a laser with a threshold gain that scales inversely with the cube of the cavity length. Using coupled-mode theory and transfer matrix analysis, we show that SIP-based lasers offer significantly lower thresholds and enhanced field localization compared to lasers operating near regular band edges, even in the presence of small losses.

2.1 Introduction

An exceptional point of degeneracy (EPD) is a point in a parameter space associated with the coalescing of the eigenvalues and the eigenvectors of a system, see for example Ref. [75, 76, 77, 78, 79, 80], or [3] where Figotin and Vitebskiy refer to EPDs as stationary points, without explicitly using the term EPD but providing detailed math and physics aspects. It has been shown that EPDs in photonic systems exist when waveguide modes are coupled in the presence of gain and loss, as in PT-symmetric systems [79, 81, 82, 83, 18, 19]. However, systems do not need to have loss and gain to exhibit an EPD. In this paper, indeed, we focus on the stationary inflection point (SIP) formation in periodic lossless and gainless waveguides [84, 85, 86, 87, 88, 89, 5, 90, 91, 92]. The SIP is an EPD of order three [5, 46]. In lossless and gainless waveguides, a second, third, and a fourth-order exceptional degeneracy of Floquet-Bloch eigenmodes are associated with a regular band edge (RBE), an SIP [93, 5], and a degenerate band edge (DBE) [17] in the frequency-wavenumber dispersion relation of the waveguide modes, respectively. In the vicinity of an EPD of order m at (k_m, ω_m), the frequency-wavenumber dispersion relation is approximated as [47, 5]

$$(\omega - \omega_m) \propto (k - k_m)^m, \tag{2.1}$$

which shows that the higher the order of the EPD, the flatter the dispersion diagram in its vicinity. For example, an SIP ($m = 3$) has a flatter dispersion diagram than an RBE ($m = 2$). The DBE has a flatness given by $m = 4$ and it is a degenerate version of the RBE. In contrast to the SIP, the RBE and the DBE have a bandgap on one side of the RBE or DBE frequency, therefore the SIP exhibits physical properties that differ from those of the RBE and DBE. The flatness at the SIP frequency ω_S is associated with the inflection point developed in the dispersion relation of the propagating component of the frozen mode [48], as is illustrated in Fig. 2.1(b). The flatness at the RBE frequency, however, is due to the coalescence of two counter-propagating modes. The common slow-wave resonances near an RBE are fundamentally different than the resonances that couple to the SIP-associated frozen mode because the SIP is not sided by a bandgap [4] and the frozen mode is composed also by evanescent waves. Moreover, the SIP condition is not particularly sensitive to the

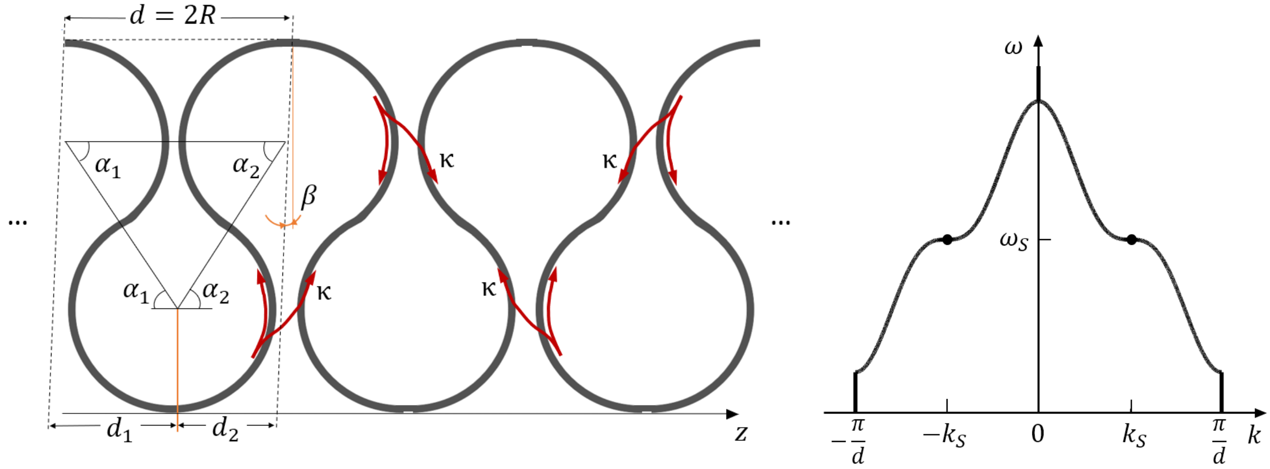

(a) (b)

Figure 2.1: (a) SIP laser made of a periodic ASOW; gain is assumed to be distributed uniformly along the waveguide. The SOI waveguide follows a serpentine path. A unit cell of length $d = 2R$ is defined within the two oblique dashed lines as in [1]. There are bidirectional coupling points between adjacent loops (denoted by red arrows). (b) Dispersion diagram of the propagating modes, with SIPs at ω_S.

size and shape of the underlying photonic structure [49]. The frozen mode regime exhibits exceptional properties including low group velocity, greatly enhanced quality factor and group delay characterized by a strong scaling with the waveguide length [4].

An enhanced group delay allows for large one-pass amplification compared to conventional lasers of the same cavity length [68]. This boost has been observed theoretically in lasing systems operating near an RBE [94] and a DBE [68, 66]. The concept of unidirectional lasing near SIP in a periodic non-reciprocal multilayered structure was discussed in [89]. A fundamental problem with the SIP realization in multilayered structures is that it essentially requires nonreciprocity, which at optical wavelengths is too small to achieve a well-defined SIP in the Bloch dispersion relation. In other words, the model considered in [89] can be practically relevant only at microwave frequencies, where the nonreciprocal effects can be strong enough. By contrast, SIP realization in three-way periodic optical waveguides does not require the use of magneto-optical materials and can be achieved in perfectly reciprocal systems at optical wavelengths. We advance the theory of SIP lasing in a silicon-on-insulator (SOI) reciprocal waveguide, namely in the periodic asymmetric serpentine optical waveguide (ASOW). The ASOW is examined using coupled-mode theory and the transfer matrix method as was done for the waveguides studied in [95, 5], and therefore our analysis is restricted to the linear regime. In the future, we aim to expand on the findings presented in this article by conducting time-domain simulations to provide an insight into mode selectivity and the impact of nonlinear effects in SIP lasers. The principal result of this paper is that resonances near the SIP frequency experience giant power gain when an active material [96] is integrated into the periodic structure. We establish that the lasing threshold corresponding to these resonances scales as N^{-3}, where N denotes the number of unit cells in the finite-length waveguide. The presence of distributed losses, such as those resulting from the roughness or radiation of waveguide bends, naturally leads to an increase in the lasing threshold. For small distributed losses, however, the inverse cubic scaling of the lasing threshold with waveguide length remains intact. In fact, we demonstrate that even though small values of gain and loss distort the dispersion diagram of the modes near the SIP, due to the exceptional sensitivity of the mode wavenumbers at an EPD [3], the distorted modes retain similar characteristics as those exhibited by the frozen mode. The SIP condition is shown to be superior to the RBE condition for enhancing the power gain in cavities with the same gain medium and length. We observe that the SIP resonance induces a lower lasing threshold than the RBE resonance, even if the SIP resonance has a lower quality factor.

The paper is organized as follows: in Section 2.2 the ASOW is defined as in [1] and we show an example of an SIP in ASOW. In Section 2.3 a gain medium is added to the ASOW. The effect of bending losses and gain-induced mode distortion on laser performance is analyzed in Section 2.4. In Section 2.5 we study potential lasing in the vicinity of RBEs close to the SIP and introduce design considerations to prevent it. The results are summarized in Section 2.6.

2.2 SIP in ASOW

The ASOW, introduced in [1] as a modification of the symmetric serpentine optical waveguide in [95], is a SOI periodic asymmetric serpentine optical waveguide depicted in Fig. 2.1(a). It is composed of small rings of radius R connected at angles α_1 and α_2, which are defined at the center of the rings and with respect to the horizontal axis. These rings are also side-coupled to the adjacent rings. Here, the evanescent coupling between adjacent rings is considered point-like, bidirectional, and lossless, as traditionally assumed [97, 98]. The lossless condition ensures $\kappa^2 + \tau^2 = 1$, where κ and τ are the coupling and transmission coefficients, respectively. The unit cell of the ASOW is defined between two oblique lines that descend from the top of two adjacent rings at an angle $\beta = \alpha_1 - \alpha_2$. The unit cell has a length of $d = 2R$, and it is portrayed in Fig. 2.2. It is convenient to split the unit cell into three different sections as was done in [1]: Section A, of which there are four per unit cell, describes a quarter of a circle and adds a phase of $\phi_A = k_0 n_w \pi R/2$ to the waves traveling through it. The term $k_0 = \omega/c$ is the wavenumber in vacuum where ω is the angular frequency, c is the speed of light in vacuum, and n_w is the mode effective refractive index. Sections B and C describe the arcs connecting the top loops with the bottom loop, at the left and right sides of the unit cell, at angles α_1 and α_2 from the horizontal axis, respectively. They describe the asymmetry of the ASOW through the angle difference $\beta = \alpha_1 - \alpha_2$, and have an associated phase of $\phi_B = k_0 n_w 2\alpha_1 R$ and $\phi_C = k_0 n_w 2\alpha_2 R$. For an SIP to form, three eigenmodes must collapse on each other (in terms of wavenumber and polarization states, i.e., eigenvalues and eigenvectors), which requires them to belong to the same irreducible wavevector symmetry group. A way to do that is by setting $\beta \neq 0$ [1], which breaks the glide symmetry of the ASOW, though the SIP has been found also in glide symmetric waveguides [46].

The electromagnetic guided fields are modeled in terms of the forward and backward waves [1]. Figure 2.2 shows the three ports at both the $n-1$ and n sides of the unit cell, and

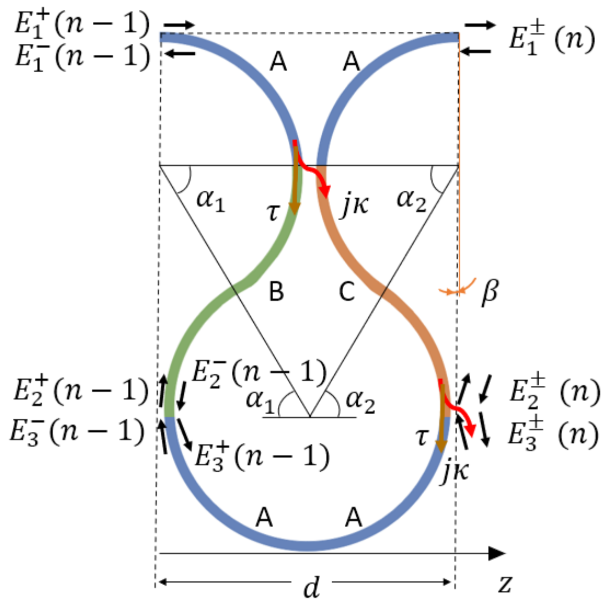

Figure 2.2: The n-th unit cell of the ASOW is divided in four Sections A, a quarter of a circle long; Sections B and C, the arcs connecting the top and bottom loops at the left and right sides of the unit cell, respectively. The angles α_1 and α_2 determine the lengths of Sections B and C (respectively), and their difference β determines the asymmetry of the unit cell. Besides the coupling to adjacent unit cells via Port 1, at each left and right sides of the unit cell, there are also proximity coupling points through Ports 2 and 3, at each side of the unit cell.

the two waves defined at the right side of each port. The state vector $\boldsymbol{\psi}(n)$ with all the six electric field wave amplitudes is defined as

$$\boldsymbol{\psi}(n) = \begin{pmatrix} E_1^+, & E_1^-, & E_2^+, & E_2^-, & E_3^+, & E_3^- \end{pmatrix}^T, \tag{2.2}$$

and its "evolution" from unit cell to cell is given by $\boldsymbol{\psi}(n) = \underline{\mathbf{T}}_u \boldsymbol{\psi}(n-1)$, where $\underline{\mathbf{T}}_u$ is the transfer matrix of the unit cell, given in [1]. The time convention $e^{j\omega t}$ is adopted in this paper. The ASOW is a reciprocal structure; it supports six independent modes (unless an EPD occurs) that appear in symmetric positions with respect to the center of the Brillouin zone (BZ) [5]. The unit cell is engineered so the three modes with the same sign of $\mathrm{Re}(k)$

coalesce at the SIP angular frequency ω_S [1]. The occurrence of the SIP (which is an EPD of order three) is demonstrated by the vanishing of the coalescence parameter σ, whose concept was introduced in [19] for a DBE (where the authors referred to it as a figure of merit or hyperdistance), and applied to an SIP in Refs. [46, 1]. In Fig. 2.3 we show the modal dispersion diagram of an SIP in ASOW, an example which is referred to throughout the paper as the SIP-ASOW. Its SIP frequency is $f_S = 193.54$ THz and it has structure parameters: $R = 6$ μm, $\alpha_1 = 67.4°$, $\alpha_2 = 55.6°$ and $\kappa = 0.5$. The ASOW is made of a rectangular waveguide with a width of 450 nm and a height of 220 nm, whose modal effective refractive index is $n_w = 2.36$ assumed constant in the frequency range of interest [1, 95].

Figures 2.3(a) and (b) depict the real and the imaginary parts of the wavenumber against the angular frequency in the fundamental BZ. Solid black lines represent modes with purely real k whereas dashed colors denote modes with complex k. The propagating modes (black solid line) in Figures 2.3(a) are the same ones shown also in Fig. 2.1(b). At the SIP angular frequency ω_S, the wavenumbers of the three modes coalesce at the two inflection points in reciprocal positions with respect to the center of the BZ, and the imaginary part of all modes vanishes. Figure 2.3(c) shows the dispersion diagram in the complex k space, where the arrows point in the direction of increasing frequency. The three wavenumbers coalescence is very clear in this figure, and at each SIP the angles between the curves are 60°. Figure 2.3(d) shows the coalescence parameter σ, defined as in [1], versus angular frequency. It vanishes at the SIP frequency, clearly showing the coalescence of three eigenvectors and therefore indicating the occurrence of an EPD of order three (the SIP). The two local minima indicate the presence of RBEs at frequencies near the SIP. While the transfer matrix $\underline{\mathbf{T}}_u$ of the unit cell is non-Hermitian and J-unitary at any frequency (see Refs. [18, 19, 99]), at the SIP frequency, $\underline{\mathbf{T}}_u$ is similar to a Jordan canonical matrix; it cannot be diagonalized [17, 5]. The EPD in this paper (the SIP) is found in a lossless and gainless ASOW, demonstrating that the presence of gain and loss is not necessary to produce an EPD.

The three descriptors of an SIP in a loaded finite-length ASOW of N unit cells are the transfer function T_f, the group delay τ_g, and the quality factor Q. The finite-length ASOW is shown in Fig. 2.1(a) where the first and last unit cells are terminated on straight waveguides, without any mirrors and any discontinuity in the waveguide, using Port 1 on either the left or the right sides of the unit cell shown in Fig. 2.2. However, since each unit cell is defined with three ports on each side, Ports 2 and 3 on either end of the finite-length ASOW are terminated without coupling to adjacent cells, as in [1]. The transfer function is defined as

$$T_f(\omega) = \frac{E_{out}}{E_{inc}} = \frac{E_1^+(N)}{E_1^+(0)}, \tag{2.3}$$

where $E_1^+(0)$ is the incident signal and $E_1^+(N)$ is the transmitted wave onto the attached straight waveguide on the right side of Fig. 2.1(a). The group delay is [68],

$$\tau_g(\omega) = -\frac{\partial \angle T_f(\omega)}{\partial \omega} \tag{2.4}$$

where $\angle T_f(\omega)$ is the phase of the transfer function. The quality factor for large N is reliably approximated by [5]

$$Q = \frac{1}{2}\tau_g(\omega_{S,res})\omega_{S,res}, \tag{2.5}$$

where $\omega_{S,res}$ is the resonance frequency closest to the SIP frequency ω_S, referred to as the SIP resonance. For long lossless-gainless periodic waveguides, the asymptotic trend is that $Q \propto$

N^3 [4, 1]. From Eq. (2.5), the group delay at the SIP resonance also scales asymptotically as $\tau_g(\omega_{S,res}) \propto N^3$. The concept of transfer function is used later on to determine the lasing threshold.

2.3 Lasing theory in coupled waveguides with SIP

2.3.1 Steady-state gain medium response

Lasing in the lossless ASOW requires doping it with a gain medium, e.g. Erbium, or with other methods, such as using quantum wells. We assume that the gain bandwidth of the active medium includes the SIP frequency of the underlying passive structure. Assuming the gain is uniformly distributed along the waveguide, the mode complex effective refractive index is [98]

$$n = n_w - jn''_g, \tag{2.6}$$

where the subscript g stands for gain and $''$ indicates the number has an imaginary value. In the first-order approximation, we neglect the effect of gain on the real part of the mode effective refractive index within the frequency range of interest. The conversion between gain modeled as an imaginary part of the mode effective refractive index n''_g and as the gain coefficient α_g (in units of dB/cm) at an angular frequency ω is $n''_g(\omega) = -\alpha_g(100/8.686)(c/\omega)$, where c is the speed of light in m/s. The imaginary part of the mode effective refractive index is negative for gain, i.e., $n''_g < 0$.

2.3.2 One-pass amplification in ASOW

Waves traveling in an ASOW at a frequency close to ω_S experience a high group delay [1], which increases the effective length of the cavity $L_{eff} = c\tau_g$ [68, 100]. In turn, this increases the effective power gain coefficient $g_{eff} = \gamma L_{eff}$ in active devices, where $\gamma = -2k_0 n_g'' f$ is the per-unit-length power gain coefficient [98]. The term f is the filling factor of the active material in the host medium. Therefore, operating the active ASOW at a resonance near ω_S results in an enhanced effective power gain coefficient, which is estimated as

$$g_{eff} \approx -2\omega_{res} n_g'' \tau_g(\omega_{res}) f, \tag{2.7}$$

and the one-pass effective power gain as

$$G_{eff} \approx |T_f(\omega_{res})|^2 e^{g_{eff}}, \tag{2.8}$$

where the T_f and the τ_g (used to calculate g_{eff}) belong to the lossless-gainless finite-length ASOW. This approximation is valid for small values of gain for which the modal properties of the SIP are not significantly perturbed [68, 101]. Section 2.4.2 provides a more in-depth discussion on the effects of gain and loss on the distortion of the modes associated with an SIP by examining its effect on the dispersion diagram and on the coalescence parameter of the waveguide modes. The effective power gain coefficient g_{eff} is rewritten as

$$g_{eff} = -4n_g'' Q f, \tag{2.9}$$

which shows why high-Q lasers, such as those operating near an SIP [1], require less gain than lasers with lower Q factors to provide the same output.

2.3.3 SIP lasing threshold scaling

We define the lasing threshold as the minimum gain required to maintain oscillations within a cavity. In a finite-length waveguide operating at a resonance and with a set gain $n''_g = n''_{th}$, the corresponding value of the effective power gain coefficient $g_{eff}(\omega_{res})$ is calculated using Eq. (2.7). Since the g_{eff} parameter is the actual gain parameter that determines the system to start oscillations, when we set this to assume the threshold value, from Eq. (2.9) one infers that the refractive index gain threshold $n''_{th} \propto 1/Q$. This relationship indicates a trend, because this discussion (as the one in the previous section, where Eq. (2.9) is derived) neglects the fact that the dispersion diagram, hence τ_g and Q, is affected by the presence of gain [68, 101].

For asymptotic gainless and lossless periodic waveguides operating near an SIP, $Q \propto N^3$ [4, 1]. Hence, the SIP lasing threshold, which is calculated at the SIP resonance $\omega_{S,res}$ of an ASOW of finite length, satisfies $n''_{S,th} \propto N^{-3}$ asymptotically. Figure 2.4 depicts this trend for the lossless SIP-ASOW, where the SIP lasing threshold is represented by blue dots. The blue line is the fitting curve $n''_{th} = -0.016 \times N^{-3} + 7 \times 10^{-8}$, calculated for $N \in [5, 40]$. We calculate the SIP lasing threshold with the approach described in Appendix A. The inversely proportional relationship between the quality factor and the lasing threshold in a conventional cavity [102] has been observed having different scaling laws near RBEs ($n''_{th} \propto N^{-3}$), DBEs ($n''_{th} \propto N^{-5}$) in photonic crystals [68] and waveguides [66], and 6DBEs ($n''_{th} \propto N^{-7}$) in periodic waveguides [103]. In comparison, here we have demonstrated that when working near the SIP, the lasing threshold scaling is $n''_{th} \propto N^{-3}$. Note that cavities made of waveguides possessing the SIP have no mirrors at their left and right ends; the cavity effect is due to the "structured" degenerate resonance where the energy distribution vanishes at the cavity edges due to the frozen mode regime, as was shown in [68] for the DBE and in [104] for the SIP.

2.4 Practical considerations

2.4.1 Distributed losses

We consider distributed losses and analyze their effect on the lasing threshold of an active ASOW. Radiation losses due to the waveguide bends in the ASOW are modeled as a positive imaginary part n''_r of the mode effective refractive index, leading to

$$n = n_w - j\left(n''_g + n''_r\right). \tag{2.10}$$

Based on the full-wave simulations in Ref. [2], bending losses are estimated as $n''_r = 2.3 \times 10^{-5}$ for a waveguide with radius $R = 6$ µm and $n''_r = 4.7 \times 10^{-6}$ for $R = 10$ µm. Therefore, the magnitude of the lasing threshold $|n''_{L,th}|$ of the lossy ASOW is

$$|n''_{L,th}| = |n''_{th}| + n''_r, \tag{2.11}$$

which shows radiation losses shift the curve shown in Fig. 2.4 upwards. Other distributed losses can also be modeled as a positive imaginary part of the effective refractive index, causing a further shift of the lasing threshold. In the following, we will show that the considered losses and gain, even though they distort the dispersion diagram, are not large enough to fundamentally modify the properties of the frozen mode associated to the SIP, i.e., the coalescence parameter still tends to vanish (Fig. 2.5), which explains why the SIP lasing threshold still scales asymptotically as a negative cube of the waveguide length.

2.4.2 Gain and loss-induced mode distortion

We discuss the modal dispersion diagram distortion induced by the presence of either gain or loss in the otherwise lossless-gainless SIP-ASOW. Eigenmodes at an EPD display exceptional sensitivity when a system parameter is perturbed by a small quantity [3]. The insertion of gain or loss in the lossless-gainless ASOW perturbs the mode effective refractive index (i.e., of the quasi-TE mode in the infinitely long homogeneous straight rectangular waveguide), by a small quantity Δn. Therefore, the degenerate wavenumber k_S at the SIP frequency splits into three wavenumbers k_q, with $q = 1, 2, 3$, estimated by a first-order approximation of the Puiseux fractional power series [3, 5, 76] as

$$k_q(\Delta n) \approx k_S + a_1 e^{j\frac{2\pi}{3}q}(\Delta n)^{1/3}, \tag{2.12}$$

where a_1 is a constant calculated following the expressions in Ref. [105]. The wavenumber perturbation at and near the SIP frequency, due to gain or loss, is stronger than the wavenumber perturbation at frequencies away from the SIP. This important phenomenon is understood by comparing the result in Eq. (2.12) with the conventional Taylor expansion for the wavenumber perturbation when the frequency is sufficiently far from the SIP, leading to each of the three wavenumbers (in each direction) k_q (with $q = 1, 2, 3$) at any ω away from the SIP to be approximated as $k_q(\Delta n) \approx k_{q,0} + b_q(\Delta n)$, where $b_q = \partial k_q/\partial n$ is the standard coefficient of a Taylor expansion when a perturbation Δn of the modal refractive index n (of the homogeneous straight waveguide quasi-TE mode) is applied. Therefore, when we look at the wavenumber perturbation from the SIP (i.e., when the system operates at the SIP frequency), one has $\Delta k_{SIP} = k_q - k_S \propto (\Delta n)^{1/3}$. This generates a larger wavenumber perturbation than $\Delta k_q = k_q - k_{q,0} \propto (\Delta n)$, i.e., when not working at the SIP frequency. As an example, when $|\Delta n| = 10^{-3}$, i.e., we modify the third decimal digit of the effective refractive index, one has $|\Delta n|^{1/3} = 10^{-1}$ which is much larger than 10^{-3}. Therefore, when in Eq. (2.10) we consider a small $\Delta n = n_g - n_w = -j\left(n_g'' + n_r''\right)$, it is clear that the dispersion diagram at the SIP is more perturbed than at any other frequency. This is confirmed by the following simulations.

Figure 2.5 shows the eigenmode perturbation in a SIP-ASOW without loss but with gain $n_g'' = -8 \times 10^{-6}$, equivalent to $\alpha_g = 2.82$ dB/cm, superimposed on the dispersion diagram of the same waveguide without gain (thin gray line). Figures 2.5(a) and (b) depict the real and imaginary parts of the wavenumbers of the modes. The inset shows the details of the perturbation of the wavenumber due to gain at the SIP. Any wavenumber perturbation is much less visible at any other frequency. The distortion of the SIP due to the presence of gain is observed more clearly in Fig. 2.5(c), which shows the dispersion diagram in the complex k space. The three wavenumbers do not fully coalesce anymore, and they slightly depart from k_S at angles of 120° from each other, as shown in Eq. (2.12). Larger gain would cause an even larger departure from k_S. These observations are in agreement with what was discussed in [101] for an RBE and in [106] for an SIP: adding gain to the lossless-gainless waveguide deteriorates the degeneracy and its exceptional properties. The extent of the deterioration of the properties, however, remains unclear. As discussed in [101], the presence of a small amount of either gain or loss causes a perturbation of the wavenumber (and hence of the group velocity) of the same magnitude.

Despite having explained why the dispersion diagram experiences the largest perturbation in the neighborhood of the SIP, we also show that the EPD-related properties associated to the SIP are however retained. Indeed, with the amount if gain here considered, we still observe the coalescence of the three eigenvectors (i.e., polarization states), that fully describe the degree of the exceptional degeneracy. Indeed, in Fig. 2.5(d) we show that even though the coalescence parameter σ does not fully vanish at the SIP, it is still significantly smaller than unity at ω_S. Therefore, the SIP feature of three eigenvectors approaching each other is still present despite the SIP distortion due to gain. Experimental verifications of the existence of an SIP in non-reciprocal and reciprocal waveguides with small losses were reported in [87, 46], where the distorted dispersion diagrams were reconstructed, which resemble the one shown in Fig. 2.5. Despite the distortion, the modes still exhibit properties typically associated with the frozen mode. Therefore, the SIP condition is relatively resistant to the presence of small values of loss or gain. For increasingly large values of gain, however, the group delay at frequencies near the SIP eventually diminishes (because the SIP gracefully loses its properties), and this effect curbs the effective power gain coefficient g_{eff} in Eq. (2.7).

In summary, despite the stronger perturbation of the wavenumbers in proximity of the SIP frequency compared to other frequencies, the coalescence parameter in Fig. 2.5(d) still shows that the three eigenvectors are close to each other, demonstrating a good degree of exceptional degeneracy. On the other hand, larger and larger gain values would strongly perturb the SIP degeneracy till there is no degeneracy anymore.

2.5 Lasing at SIP versus RBE

It is typical that optical structures capable of supporting an SIP also have RBEs close to ω_S [4, 89, 5, 1, 91, 107, 108]. Tolerances in fabrication might prevent the formation of the SIP, and the laser would then operate near an RBE. The lossless-gainless ASOW is relatively robust to fabrication tolerances because it is formed by a single waveguide with a continuous curvature slope, as seen in Fig. 2.2, and therefore some changes would only cause a shift of the SIP frequency. For example, a perturbation in n_w is expected to occur uniformly, so the SIP would still be formed, although at a different frequency. However, some other perturbations may degrade the quality of the SIP (the coalescence parameter would not approach zero), and therefore the properties of the frozen mode might be compromised.

In some scenarios, despite the occurrence of an SIP, a laser might emit at the RBE resonance frequency $\omega_{R,res}$, the closest to the RBE frequency, if it has a lower lasing threshold than the one associated to the resonance at $\omega_{S,res}$.

To prevent RBE lasing, one potential solution is to increase the frequency difference between the SIP and RBE. Consequently, we consider the free spectral range (FSR), defined by the phase accumulated by propagation along the optical length of an ASOW unit cell without coupling (ie: without the frozen mode). From [95] adapted to the asymmetric case studied in [1] and here, we have

$$\Delta f_{FSR} = \frac{c/n_w}{2R(\pi + \alpha_1 + \alpha_2)}. \tag{2.13}$$

Therefore, the distance between the SIP and the RBE is increased by decreasing R, which effectively stretches the dispersion diagram. A smaller loop radius, however, is associated with higher radiation losses, as shown in Fig. 2.6. As a compromise, we choose $R = 6$ µm in the SIP-ASOW example. In the following discussion, we compare the performance of the SIP-ASOW of different lengths operating either near the SIP or near an RBE (shown in Fig. 2.3). We choose to consider the RBE at a lower frequency (f_R) than the SIP (f_S) because it is the one closest to the SIP (versus the RBE at a higher frequency than the SIP). The frequency difference between these two EPDs is $\Delta f = f_S - f_R = 76.4$ GHz.

Assuming both the SIP and the RBE frequencies fall within the active frequency region of the gain medium, as would be the case for an Erbium-doped waveguide [109], the system may start oscillations at the SIP resonance frequency $f_{S,res}$ or at the RBE resonance frequency $f_{R,res}$. We denote by $n''_{S,th}$ and $n''_{R,th}$ the two gain values that would start oscillations at those two frequencies, respectively. Lasing near the RBE would occur if the RBE lasing threshold, which is calculated at $\omega_{R,res}$ following the method described in Appendix A, satisfies $|n''_{R,th}| < |n''_{S,th}|$. Following the discussion from Section 2.3.3, one would expect lasing near the RBE if the quality factor near the RBE is larger than near the SIP. Figure 2.7(a) shows the RBE quality factor Q_R, calculated using Eq. (2.5) at $\omega_{R,res}$, for different N (in red dots), and the SIP quality factor Q_S, calculated at $\omega_{S,res}$ (in blue dots). Both quality factors are calculated at a loaded ASOW, continued on the rectangular waveguides on the left and right sides without mirrors, as in the inset in Fig. 2.4. We also plot the fitting curves (solid lines) governed by

$$\begin{aligned}
&Q_S \approx aN^3 + b, \\
&Q_R \approx cN^3 + d, \\
&\Delta Q \approx Q_R - Q_S = (c-a)N^3 + (d-b),
\end{aligned} \tag{2.14}$$

with coefficients $a = 69.8$, $b = 5.2 \times 10^4$, $c = 139.6$, and $d = 10^5$. As expected, Q_S and Q_R scale asymptotically as N^3, when the cavity resonant frequency is near the SIP [4, 1] and near the RBE [5], respectively. Their difference $\Delta Q = Q_R - Q_S$ is shown as a dashed black line, also follows the trend $\Delta Q \propto N^3$ for large N, and for the specific SIP-ASOW under consideration, $Q_S << Q_R$. This shows that the SIP-associated frozen mode regime in the current design is not as mismatched to its termination impedances as the cavity associated with the RBE resonance. The small zig-zag distribution of Q_S with waveguide length is discussed in [1].

Because of the $Q_R \propto N^3$ asymptotic scaling, we expect the RBE lasing threshold to also scale asymptotically as $n''_{R,th} \propto N^{-3}$. Indeed, that is what we observe. Fig. 2.7(b) shows $|n''_{R,th}|$ in red dots, fitted by the red solid-line curve, and $|n''_{S,th}|$ in blue dots, which is fitted by the blue curve given by

$$\begin{aligned} n''_{S,th} &\approx eN^{-3} + f, \\ n''_{R,th} &\approx gN^{-3} + h, \\ \Delta n''_{th} &= n''_{R,th} - n''_{S,th} \approx (g-e)N^{-3} + (h-f), \end{aligned} \tag{2.15}$$

with coefficients $e = -0.016$, $f = 7 \times 10^{-8}$, $g = -0.02$, and $h = 6.9 \times 10^{-8}$. The magnitude of the difference between the lasing thresholds for lasers working at the RBE resonance or at the SIP resonance, $\Delta n''_{th} = n''_{R,th} - n''_{S,th}$, is depicted as a dashed black line. The difference in lasing thresholds between the SIP and RBE also scales asymptotically as N^{-3}, resulting in comparable thresholds for large waveguides. Therefore, to balance the preservation of the frozen mode properties with the prevention of accidental lasing near an RBE, the waveguide length should be chosen as a trade-off between achieving a small $|n''_{S,th}|$ and a relatively large $\Delta n''_{th}$.

Figure 2.7(c) shows the lasing threshold against the quality factor of an SIP-ASOW laser operating near the RBE (in black) and near the SIP (in blue), where each dot refers to a finite-length ASOW of N unit cells, with $N \in [5, 40]$. Each ASOW has a higher Q at the RBE resonance (nearest resonance to the RBE frequency) than that at the SIP resonance (nearest resonance to the SIP frequency). Therefore, one would a priori expect the RBE lasing threshold to be lower than the SIP lasing threshold. However, the opposite has been observed. This discrepancy may be attributed to the impact of the field amplitude distribution within the underlying passive cavity on the lasing threshold after the inclusion of gain in the cavity. Indeed, Figure 2.7(c), which compares the SIP-induced lasing threshold with the RBE-induced lasing threshold, shows similar curves than those in Figure 16 in [66], which compares a DBE cavity and an RBE cavity with the same quality factors.The authors show that the lasing threshold induced by the DBE is lower than that induced by the RBE because the field amplitude distribution is greater in the DBE cavity. See also a related discussion in [68] in terms of local density of states distribution within the cavity, for the DBE and RBE cases. However, in this paper, we examine the lasing threshold in the vicinity of two EPDs (an SIP and an RBE) in the same cavity. Our numerical experiments reveal that the SIP-induced lasing threshold is lower than that induced by the RBE, even though the RBE quality factor is larger.Although additional investigation is necessary to understand the difference in the field amplitude distribution in SIP and RBE cavities, and its effect on the lasing threshold, the evidence presented in this paper shows that in an active ASOW, SIP-induced lasing is preferred over lasing near an RBE.

To further illustrate the threshold difference between lasing near the SIP and the RBE, Figure 2.8 depicts the magnitude of T_f (in dB) against ω for a finite-length SIP-ASOW with $N = 25$ for different values of gain. The vertical blue and red dashed lines depict the SIP and the RBE frequencies, respectively. In Fig. 2.8(a) the ASOW has no gain, $n''_g = 0$. The magnitude of the T_f function at the SIP resonance is already higher than at the RBE resonance in the passive ASOW. Then, one would a priori expect the lasing threshold near the SIP to be lower than near the RBE, as it is indeed the case observed. In Fig. 2.8(b) the gain is set to the SIP lasing threshold, $n''_g = n''_{S,th}$, where the $|T_f|$ experiences a local maximum close to ω_S. The peak at the SIP resonance decreases as the gain increases above its threshold. This effect is explained in detail in Appendix A. In Fig. 2.8(c) the gain is further increased to the RBE lasing threshold, $n''_g = n''_{R,th}$, and the maximum of $|T_f|$ occurs instead near ω_R. Further investigation is necessary to determine how the enhanced field amplitude distribution in passive cavities operating near an EPD affects T_f and the lasing threshold of the system with gain. In summary, resonances near the SIP frequency require a smaller effective power gain coefficient g_{eff} to lase than resonances near the RBE frequency. Therefore, though not shown here, we expect that an SIP-based laser has higher lasing efficiency, meaning that it emits more output power with less gain than an RBE-based laser. In all likelihood, the SIP lasing threshold is lower than the RBE lasing threshold due to a combination of factors, which ultimately arise from the contrast between the exceptional properties of the SIP-associated frozen mode and those of the standing wave characteristic of the RBE. Moreover, the threshold difference between lasing near an SIP or an RBE could be increased by using the two degrees of freedom associated with the two left and right terminations, which may affect the RBE and SIP resonances differently.

2.6 Conclusion

Lasing conditions in the vicinity of an SIP have been investigated for an ASOW terminated on a straight waveguide at each end of the ASOW cavity. The ASOW cavity does not need mirrors to display a high quality factor and low gain threshold. The mode mismatch between the SIP-ASOW and the straight waveguide is attributed to the frozen mode, i.e., to its three degenerate modes and the resulting Bloch impedance. By analyzing the degenerate modes in the periodic ASOW, we have shown that the eigenmode distortion due to the presence of a net gain or loss is more severe near the SIP frequency than at other frequencies; however, the properties associated with the three-mode exceptional degeneracy are in part preserved for relatively small values of gain, which can nevertheless bring the system above threshold. We have observed that the quality factor of both the SIP resonance and the RBE resonance scales as a cube of the waveguide length, and the lasing threshold as a negative cube of the waveguide length. While an SIP cavity displays a lower Q factor than an RBE cavity of the same gain medium and length, it also displays a lower lasing threshold. Although we propose that this disparity is caused by the different field distributions in the cavity at the two resonances, it has yet to be confirmed. Nonetheless, our research has revealed that SIP lasing is preferred. While the results here have been shown specifically for the ASOW, the insights and conclusions outlined in this paper can be readily applied to other periodic optical waveguides that display an SIP. Further control of the SIP and RBE lasing thresholds could be exerted by changing the loading at the two ends of the lasing cavity. Future considerations into SIP lasers shall also focus on mode selectivity, the impact of nonlinear effects, and their transient response.

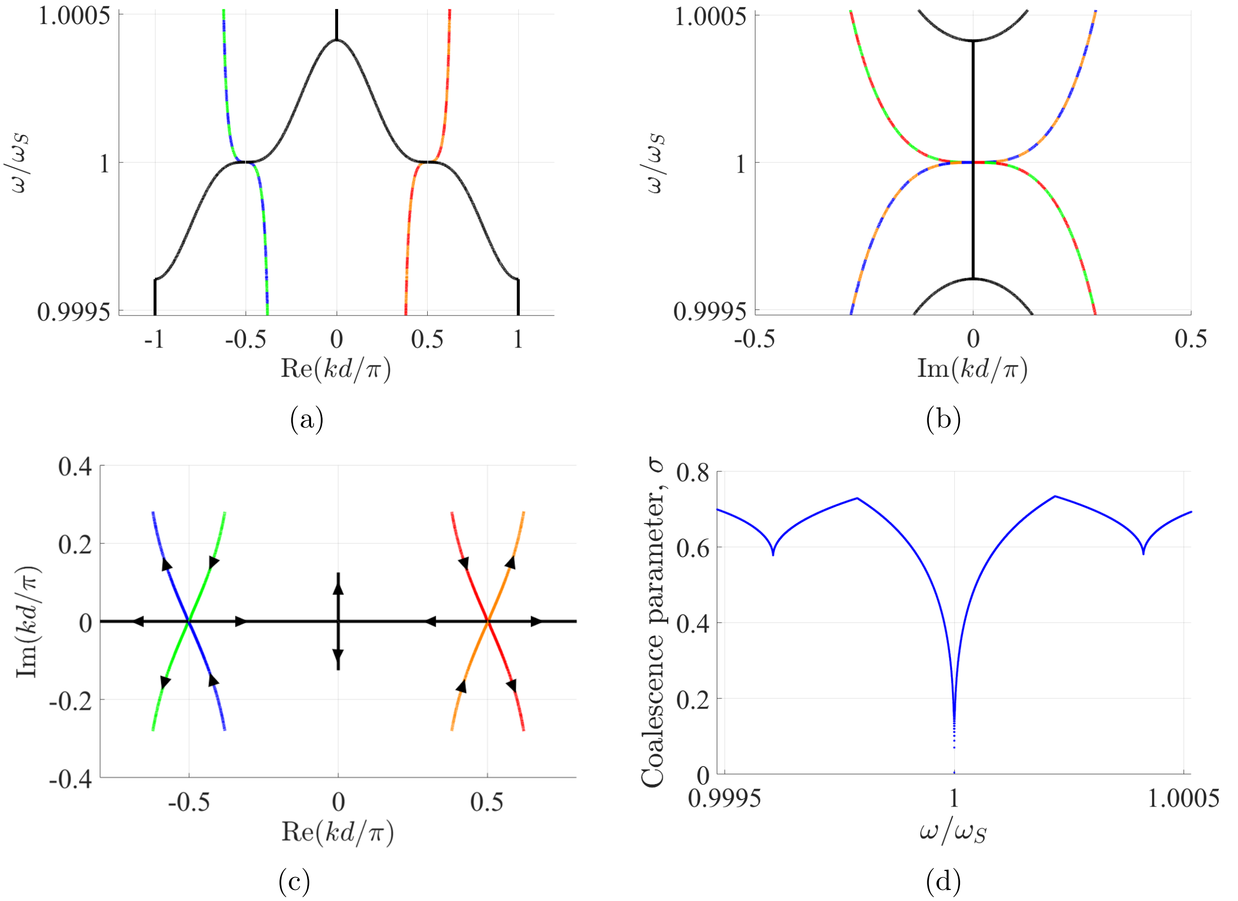

Figure 2.3: Modal dispersion diagram of the lossless and gainless SIP-ASOW. (a) The real part of the eigenvalue versus angular frequency in the fundamental BZ. Solid black: modes with purely real k; dashed colors: modes with complex k (overlapping dashed colors imply two overlapping branches). Three curves meet at an inflection point, with reciprocal k_S and $-k_S$ positions. (b) The imaginary part of k versus angular frequency. At the SIP, the three degenerate modes have $\mathrm{Im}(k) = 0$. The black curve has $\mathrm{Im}(k) = 0$ also near the SIP frequency. (c) Alternative representation of the dispersion diagram in the complex k space. The arrows point in the direction of increasing frequency. (d) Coalescence parameter σ versus angular frequency. The coalescence parameter σ vanishes at an SIP. The local minima of σ indicate the presence of RBEs near the SIP.

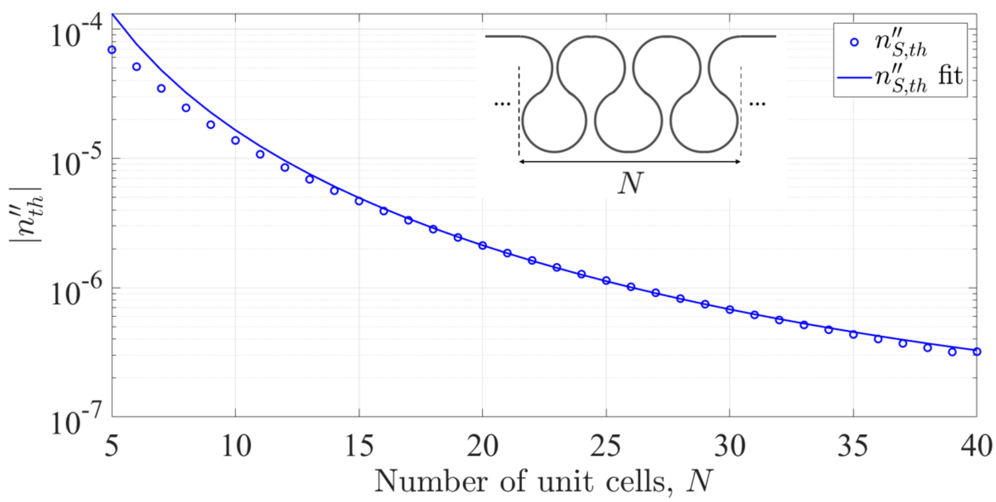

Figure 2.4: Magnitude of the SIP lasing threshold $|n''_{S,th}|$ of a finite-length SIP-ASOW of length N. The SIP lasing threshold is fit by $n''_{th} = -0.016 \times N^{-3} + 7 \times 10^{-8}$, calculated for $N \in [5, 40]$. The inset shows a finite-length ASOW of N unit cells terminated without any discontinuity on straight waveguides. The cavity has no mirrors.

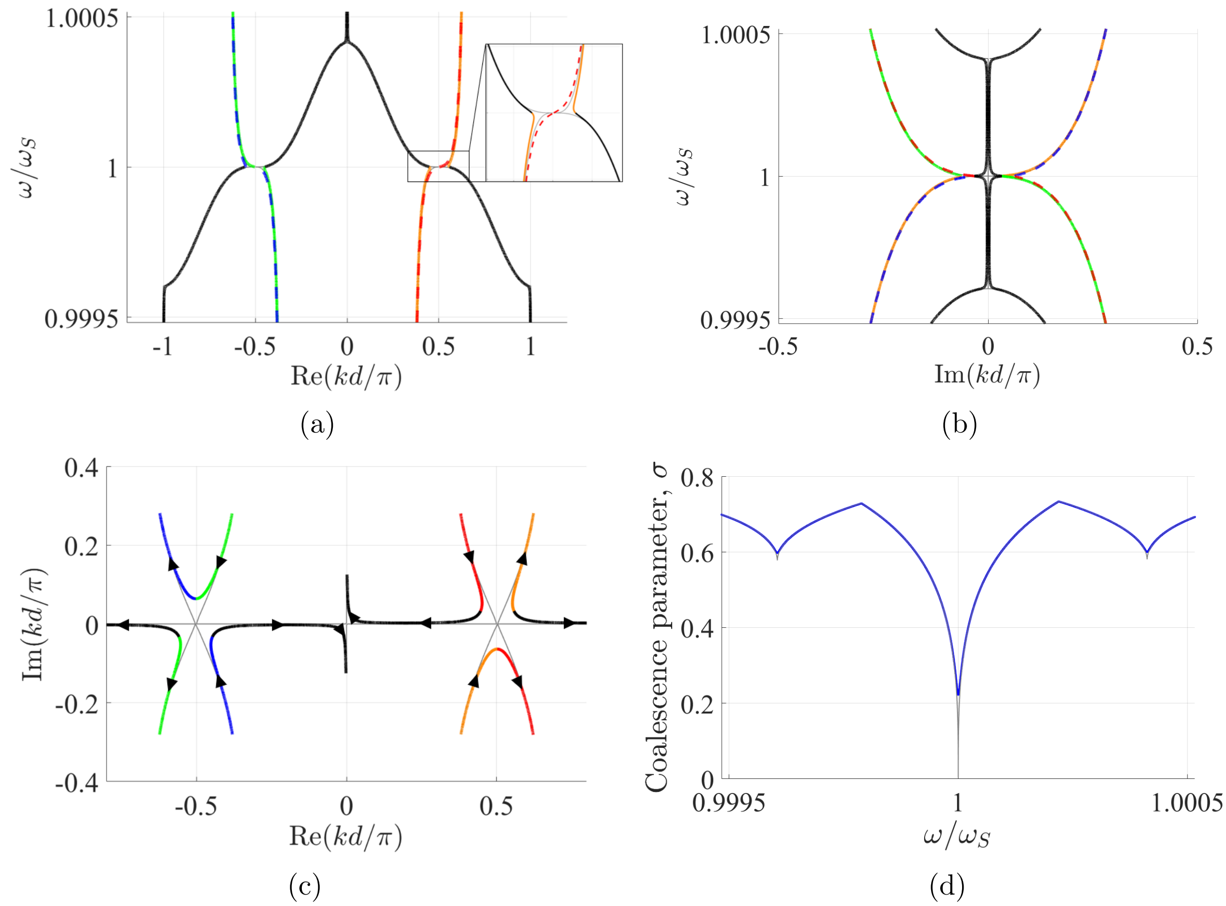

Figure 2.5: Modal dispersion diagram of the SIP-ASOW with a gain of $n''_g = -8\times10^{-6}$, equivalent to $\alpha_g = 2.82$ dB/cm. The black curves represent propagating modes, with purely real wavenumbers; the dashed, colored curves represent evanescent modes. The dispersion diagram for the SIP-ASOW without gain is shown in light grey. (a) Real part of the wavenumber versus angular frequency in the fundamental BZ. The inset shows the eigenvalue distortion is accentuated at the SIP. (b) The imaginary part of k versus angular frequency. Due to gain, $\mathrm{Im}(k) \neq 0$ at all the frequencies, especially around ω_S. (c) Alternative representation of the dispersion diagram in the complex k space. The lack of mode coalescence due to gain is very clear in this figure, with the three modes departing from k_S at 120° from each other as expected from Eq. (2.12). (d) The coalescence parameter σ versus angular frequency. The non vanishing σ indicates the SIP does not fully form, but the dip still demonstrates a degree of exceptional three-mode degeneracy to be exploited for the SIP laser.

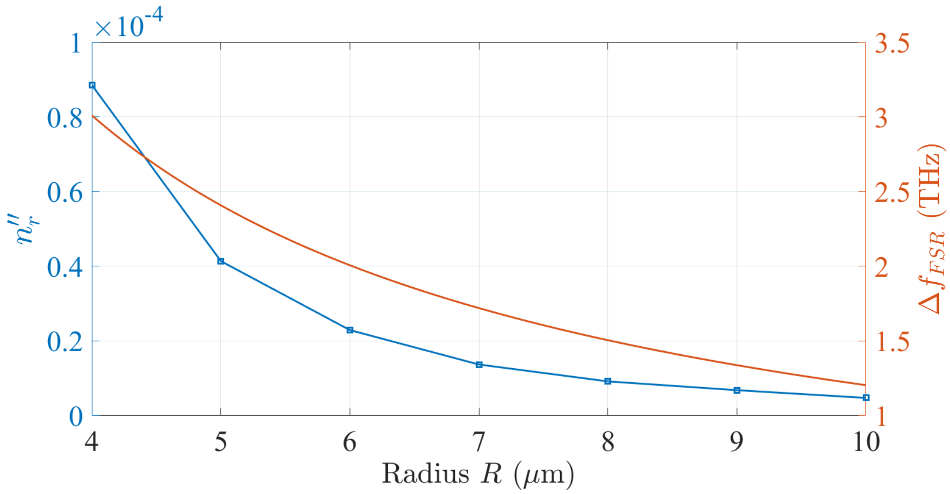

Figure 2.6: The loss values in terms of the imaginary effective refractive index are extracted from [2], and the FSR values are calculated using Eq. (2.13) with the structure parameters from the SIP-ASOW. Low radiation losses imply small FSR, which in turns implies a large spectral density of features like SIP and RBE frequencies.

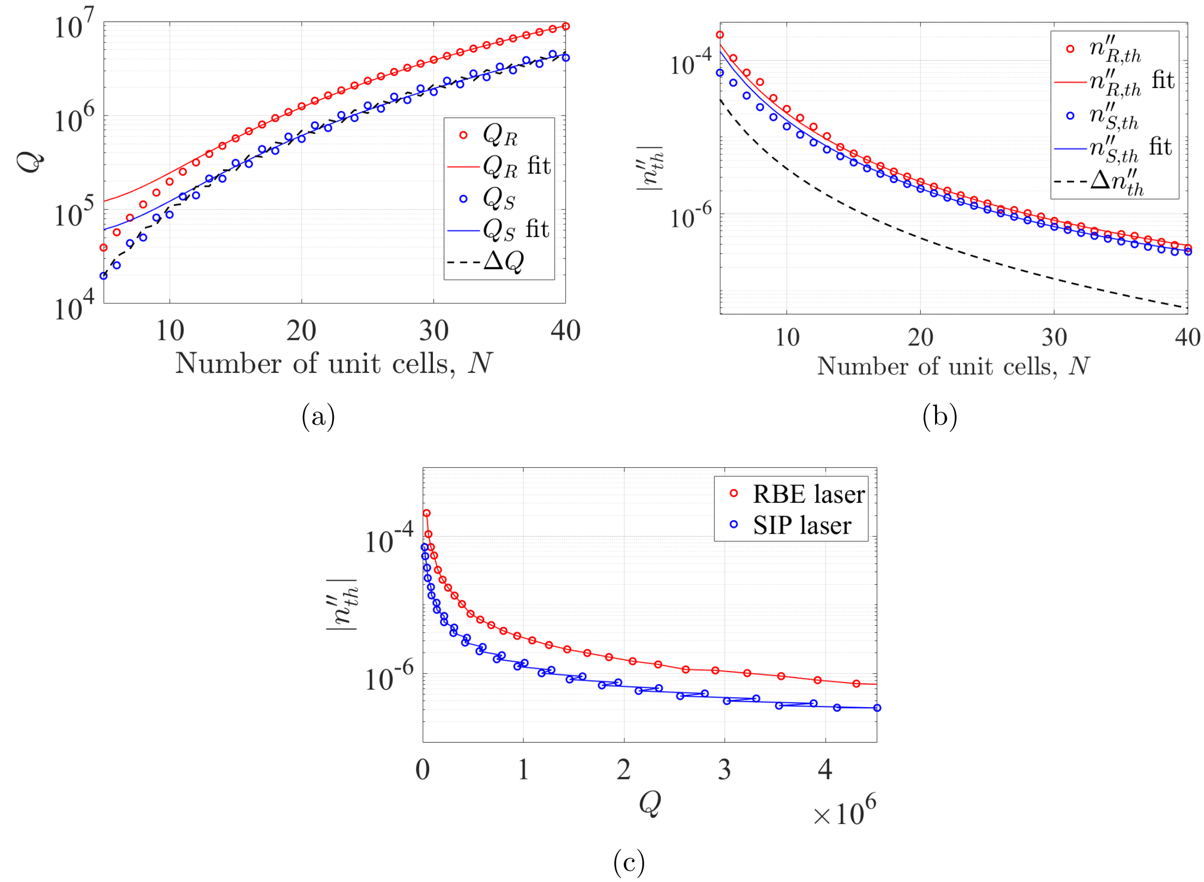

Figure 2.7: Comparison between the SIP and RBE ASOW lasers of different lengths, operating either near the SIP frequency ω_S (in blue) or the RBE frequency ω_R (in red), respectively. (a) The RBE quality factor Q_R (represented by red dots), fitted by the red curve from the first equation in Eq. (2.14); the SIP quality factor Q_S (represented by blue dots) is fitted by the blue curve following the second equation in Eq. (2.14); and their difference $\Delta Q \approx Q_R - Q_S$ is represented as a dashed, black line. The three curves scale as N^{-3}. (b) Magnitude of the RBE lasing threshold (represented by red dots), fitted by the magnitude of the red curve from the first equation in Eq. (2.15); and the magnitude of the SIP lasing threshold (represented by blue dots), fitted by the magnitude of the blue curve following the second equation in Eq. (2.15); and the magnitude of their difference $\Delta n''_{th} = n''_{R,th} - n''_{S,th}$ is represented as a dashed, black line. The three thresholds decrease as N^{-3}. The lasing threshold associated to the SIP resonance is smaller than the RBE one for an ASOW of the same length. (c) Magnitude of the lasing threshold versus quality factor for an RBE -based laser operating near ω_R (in black) and for an SIP -based laser operating near ω_S (in blue). Each dot (red and blue) represents a finite-length ASOW with a given Q provided by some $N \in [5, 40]$. An active ASOW operating near an SIP has a lower lasing threshold and lower quality factor than the same ASOW operating near an RBE.

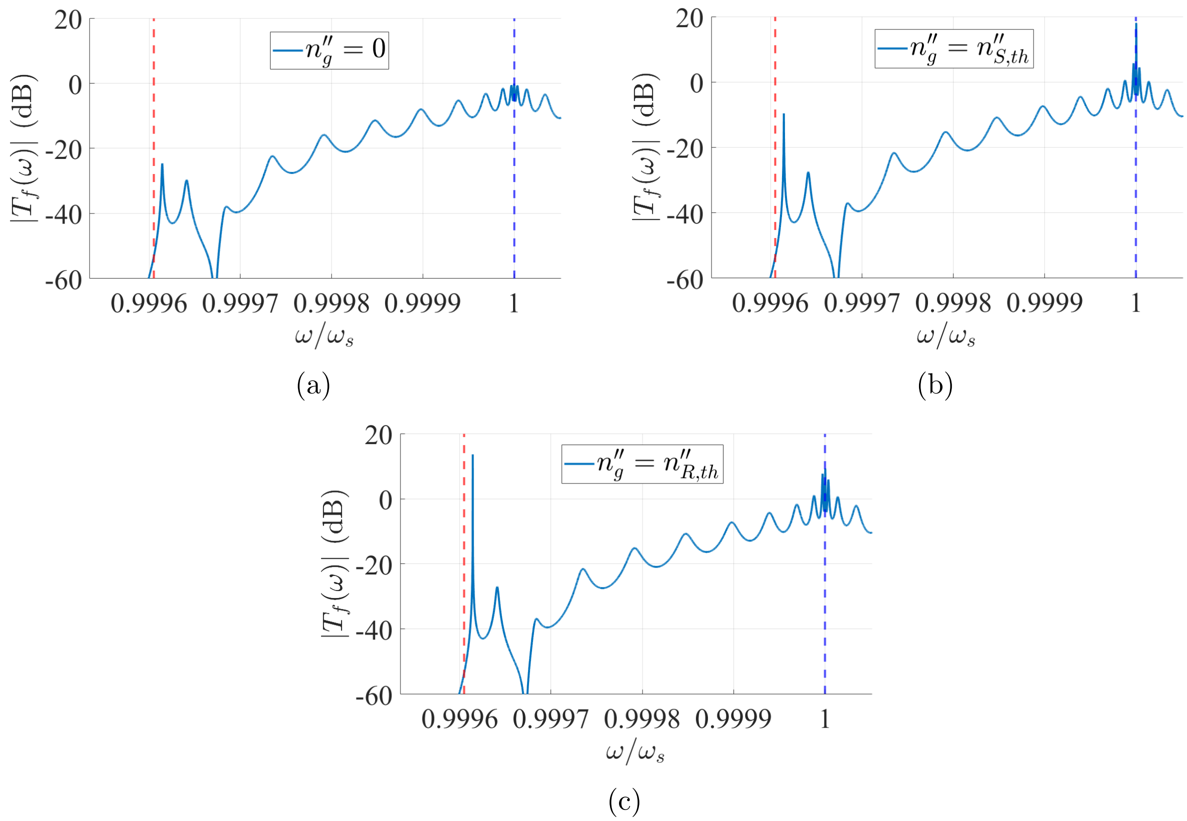

Figure 2.8: The magnitude of the function $|T_f(\omega)|$ in (dB) for the SIP-ASOW with $N = 25$ for different values of gain. The SIP and the RBE frequencies are shown as vertical dashed blue and red lines, respectively. (a) With no gain, resonances accumulate around ω_S. The function $|T_f|$ near the SIP is already higher than near the RBE. (b) With $n''_g = n''_{S,th}$, the highest peak occurs at the SIP resonance frequency. (c) With $n''_g = n''_{R,th}$, $|T_f(\omega_{S,res})|$ is reduced and the maximum occurs at the RBE resonance $\omega_{S,res}$.

Chapter 3

Frozen mode waveguide design

In this chapter, we present a systematic methodology for designing slow-light photonic integrated circuits with a frozen mode based on a special kind of exceptional point of degeneracy (EPD) of order three named stationary inflection points (SIPs). This is realized through three-way coupled waveguides with lateral gratings operating at telecommunication wavelengths. We provide two designs and analyze sensitivity to geometric perturbations. We have fabricated a periodic waveguide with integrated tapers and demonstrate good agreement with full-wave simulations. These findings confirm the feasibility of integrating SIP-based delay functionalities in standard silicon photonic platforms.

3.1 Introduction

The growth of increasingly precise nanometric fabrication practices leads to the development of photonic integrated circuits (PICs) wherein integrated optical devices such as waveguides and resonators are built within a common semiconductor wafer.

Here, we focus on a new design of gainless and lossless PIC waveguides that support an exceptional point of degeneracy (EPD) that is a point in the parameter space of a system where the eigenstates coalesce. Some early studies of guiding systems supporting this kind of EPDs are Refs. [84, 17, 4], where the authors discuss the physical aspects of the same EPD studied here using the term ”stationary point” without resorting to the term exceptional point. In particular, in this paper we focus on the stationary inflection point (SIP) that is an EPD of order three. EPDs feature in a variety of classical and quantum mechanical problems [78], most notoriously in the presence of balanced gain and loss (a condition known as PT-symmetry [79, 81, 18]).

EPDs in periodic photonic devices can be achieved through dispersion engineering without the need for gain or loss [5]. The concept was earlier explored in Refs. [99, 3, 4, 88, 47] without using the term ”exceptional point”. Other examples of dispersion diagrams that show a stationary inflection point are Refs. [110, 111, 95, 112], though not relating it to stationary points or EPDs. The order of the EPD is given by the number of coalescing eigenmodes, and it is very important in determining the properties of the finite-length device. Devices operating near EPDs also display a heightened sensitivity to parameter perturbations, which is part of the reason why the successful fabrication of high-order EPD-based PICs has been difficult to achieve. Only a handful of experimental studies exist in optics, as in [113] for the degenerate band edge and in [114] for the SIP.

One of the most striking properties of the SIP is the coalescence of propagating modes with evanescent modes, resulting in the formation of a frozen mode characterized by an extremely low group velocity ($v_g = \partial\omega/\partial k$) and enhanced field amplitudes away from the cavity's edge. At the edges of the device, propagating and evanescent modes interfere destructively, satisfying the boundary conditions [4] and creating unique field properties and field enhancement. An EPD of order 2 is a regular band edge (RBE) involving only two counter-propagating modes which results in a standard standing wave [5]. Higher order EPDs instead involve evanescent fields as well [99, 3, 5]. The lowest-order EPD to display the frozen mode is known as a stationary inflection point (SIP); it is identified as an inflection point in the Bloch mode dispersion diagram of the waveguide, and it is an EPD of order three [5, 1].

Figure 3.1(a) shows the real branches of the modal dispersion diagram of an SIP-supporting design and (b) shows its group velocity $v_g = 2\pi\partial f/\partial k$ against the Bloch wavenumber k near the SIP. The group velocity reaches a minimum at the SIP wavenumber k_S. Though not shown in Fig. 3.1 because only the propagation branches are shown, there are three modes coalescing at the SIP when considering also the evanescent modes. The frozen mode associated with the stationary inflection point that is an EPD of order 3 cannot be generated with only two counter-propagating modes because evanescent modes are also needed. Therefore, at least three modes (propagating or evanescent) in each direction, properly coupled, are needed, as explained in [4, 47, 5, 1].

Operating near an SIP offers advantages over an RBE: it supports the frozen mode while exhibiting lower sensitivity than higher-order EPDs, and it is not sided by a band gap. Therefore, even though the SIP displays an asymmetric group velocity dispersion (the group velocity variation with frequency), signal distortion can be undone as long as the transmission spectrum of the waveguide is properly characterized. For its unique dispersion, the SIP has been proposed as a strategy to conceive devices that reach large true time delay [91, 115]. It is also investigated to conceive new lasing regimes [15, 116, 117, 118], and nonlinear isolators, because of its unique properties.

We introduce a method for designing periodic PIC waveguides that support an SIP through dispersion engineering. The resulting structures, referred to as three-way coupled waveguides, consist of either two gratings coupled to a central waveguide (TWG2) or a single grating side-coupled to two adjacent straight waveguides (TWG1). The SIP arises from the synchronization of three modes: one propagating and two evanescent, which coalesce into a frozen mode. To achieve this, we develop and analyze three designs (two TWG1s and one TWG2), shown respectively in Fig. 3.2(a) and (b), and design their geometries to account for realistic waveguide cross-sections and fabrication tolerances, using eigenmode-based analysis. To the best of the authors' knowledge, SIP waveguides using these PIC compatible waveguides with lateral gratings have never been shown before. Furthermore, we show that the proposed structures exhibit some resilience to simulation-mesh quality and waveguide dimensions. After the waveguide design and tapeout preparation, we measure the transfer function of fabricated devices. We compare the measured spectral response to the same structure in simulation and investigate the group delay in simulations.

The paper is organized as follows: The methodology to design SIP-supporting three-way waveguides is described in Section 3.2. In Section 3.3, we highlight the expected differences between design and fabrication, leading to a redesign that is more consistent with fabrication methods. The results are summarized in Section 3.4.

3.2 Process steps to design an SIP

To design an SIP-supporting PIC, the *first step* is to couple a waveguide with grating to a straight channel waveguide such that their counter-propagating modes meet near a target point (k_S, f_S) in the Brillouin zone, forming a bandgap around f_S. A third waveguide with an optical mode is then positioned adjacent to the coupled pair. As it is brought closer, the interaction among the three waveguides generates local extrema in the dispersion near f_S. Fine parameter tuning enables the formation of an SIP at the desired location.

Figure 3.3 illustrates the SIP design process using the TWG1 configuration as an example. Panels (a) and (b) show the individual dispersion diagrams of the (a) grating–straight waveguide pair, and (b) the individual third waveguide, respectively. In (c), the lightly coupled three-way structure shows local maxima and minima near (k_S, f_S). In (d), after optimizing parameters such as waveguide widths and gaps, an SIP is achieved, identified by a stationary inflection in the Bloch dispersion diagram with vanishing group velocity at (k_S, f_S). Similar dispersion diagrams are shown in [88] depending on the value of a waveguide parameter.

We designed two TWG2 waveguides and one TWG1 waveguide (TWG2A, TWG2B, and TWG1A) supporting an SIP at f_S in the range $[192, 195]$ THz. Table 3.1 summarizes the parameters for each design. A key figure of merit is the frequency separation Δf_{SR} between the SIP and the nearest RBE, which should be large to ensure stable SIP operation in long waveguides. Generally, Δf_{SR} improves with smaller unit cell periods d, consistent with the increase in free spectral range $\Delta f_{FSR} = c/(n_w d)$ [95]. Previous photonic integrated waveguides supporting an SIP displayed an estimated Δf_{SR} (in GHz) of: 344 [91], 60 [5], 31 [1], 80 [116], 306 [119], and 186 [118]. As shown in Table 3.1, the designs presented here achieve significantly larger Δf_{SR} than previous SIP designs, such as the $\Delta f_{SR} = 1000$ GHz of the TWG2RA discussed later on, owing to their small unit cell periods.

Table 3.1: SIP-supporting waveguide designs

Params (nm)	**TWG2A**	**TWG2B**	**TWG1A**
w	310	300	450
w^+	250	250	480
w^-	420	325	477
g^+	325	325	200
g^-	200	200	291
w_c^+	200	200	200
w_c^-	380	466	-
t^+	200	200	200
t^-	200	200	-
d	350	370	325
f_s (THz)	192.28	193.13	192.95
$k_s d/\pi$	0.983	0.97	0.87
Δf_{SR} (GHz)	540	565	80

Modal dispersion relations were obtained using the full-wave eigenmode solver in CST Studio Suite based on the finite element method. Phase shifted periodic boundaries were applied at two virtual cross-sections spaced by one period, d. The transverse boundary conditions consist of perfect electric conductor (PEC) walls positioned far from the waveguide core, with sufficient silicon dioxide cladding to ensure the evanescent fields decay before reaching the boundaries. Material dispersion is neglected in the frequency range of interest [120]; the refractive indices of the silicon core $n_{Si} = 3.478$ and cladding $n_{SiO_2} = 1.444$ are considered constant with respect to the frequency.

3.3 Wafer tapeout preparation

Generally, SIP-based devices display a high sensitivity to geometric perturbations, as it happens in EPD systems in general, [76, 17, 5]. To preserve the frozen mode, the waveguides are here redesigned to account for fabrication-induced constraints that, even if small, may disrupt mode coalescence. A key limitation in fabrication is the minimum feature size, typically around 100 nm.

A common and predictable issue is waveguide cross-section distortion, where fabricated waveguides taper at the top, resulting in a trapezoidal shape rather than the ideal rectangular cross-section assumed earlier in the design process.

The effects of this variation are illustrated in Figure 3.4, which displays the dispersion diagram for the SIP-TWG2A waveguide with both cross-section types. Introducing a realistic waveguide sidewall angle (i.e., by decreasing the top dimensions based on tilting all walls by a few degrees θ_δ from the 90°) alters the mode profile, resulting in weaker waveguide coupling. The waveguides are nominally 220 nm wide and the top width is adjusted to account for the realistic sidewall angle θ_δ [121]. Due to the resilience of the waveguide geometry to perturbations, even the TWG2A waveguide with tilted walls still exhibits a flattened dispersion diagram that results in large group delay. However, the SIP condition is slightly disrupted and must be restored through fine parameter optimization. This is what we do next.

The updated values of the parameters for the redesigns that support an SIP with trapezoidal cross-sections are shown in Table 3.2. These values refer to the bottom dimensions. The hyphens in the TWG1RA column serve to show that there is no second grating in this structure.

Preparing frozen mode PICs for wafer tapeout requires a tolerance analysis to evaluate device performance after fabrication. While some analytic models treat tolerances as variations in the effective index [117], we directly study how perturbations affect the Bloch dispersion and the formation of the SIP.

Table 3.2: Realistic SIP-supporting waveguide designs

Params (nm)	**TWG2RA**	**TWG2RB**	**TWG1RA**
w	310	300	450
w^+	250	250	480
w^-	420	325	**477**
g^+	**319**	325	200
g^-	200	200	**305**
w_c^+	200	200	200
w_c^-	**340**	**436**	-
t^+	200	200	200
t^-	200	200	-
d	**355**	370	325
f_s (THz)	195.755	197.58	194.16
$k_s d/\pi$	0.867	0.91	0.96
Δf_{SR} (GHz)	1000	664.5	127.6

Fabrication tolerances are generally around $2 - 5$ nm [121, 117] which are either added or subtracted from the nominal geometric parameters. Figure 3.5 shows the dispersion diagram of the TWG2RB design. The nominal case, in black, and perturbed cases with $\Delta = \pm 10$ nm applied collectively to the waveguide widths w, w^+, and w^- in blue and red, respectively.

The Δ perturbation in width leads to the formation of near stationary points in the dispersion, known as tilted inflection points (TIPs) [122]. In the example shown in Figure 3.5, decreasing the parameter values by 10 nm only disrupts the SIP condition slightly. The resulting red curve exhibits a smooth-TIP, a near-inflection point with low but non-zero group velocity. In contrast, increasing the parameter values produces the blue curve, which shows a local maximum and minimum near the SIP frequency. This configuration corresponds to an alternating-TIP, where the group velocity changes sign in the vicinity of the SIP frequency. Such features often appear as intermediate stages in the SIP waveguide design process described in Section 3.2, and in [88] where the authors show the dispersion variation by fine-tuning a waveguide parameter. Comparable asymmetric responses are observed when varying the corrugation widths, gap sizes, or thicknesses in the TWG2RA (not shown), and in the TWG2RB and TWG1RA designs. These results confirm the resilience of the proposed SIP-based waveguides to some geometric perturbations, as even small changes in waveguide dimensions shift the dispersion notably but the modal dispersions still retain a shape that exhibits inflection points that lead to large group delay. The response is also asymmetric with respect to the direction of the variation, as shown by the different behaviors for $\Delta = \pm 10$nm. In summary, we observe the important result that despite perturbations twice as large as the expected fabrication tolerance (2–5nm), the dispersion still exhibits a strong curvature and low group velocity near the SIP. This indicates that while precise fabrication is critical, the SIP regime remains robust under moderate deviations.

In Figure 3.6 we show the redesigned waveguide TWG2RA to exhibit an SIP at $f_{\mathrm{S}} = 195.755$ THz with trapezoidal cross section. We also show the upper and lower branches and their critical points. In particular, the RBE of the blue branch is 1 THz below the SIP of the orange branch. This is the waveguide design that is studied in the next section where we analyze the transfer function and group delay of waveguides with finite length.

3.4 Conclusion

We have introduced a robust design methodology to obtain three-way coupled waveguides that support an SIP at communication frequencies. The process enables tuning the dispersion diagram to support an SIP at targeted frequencies while accounting for fabrication limitations, such as non-ideal cross-sections and tolerances.

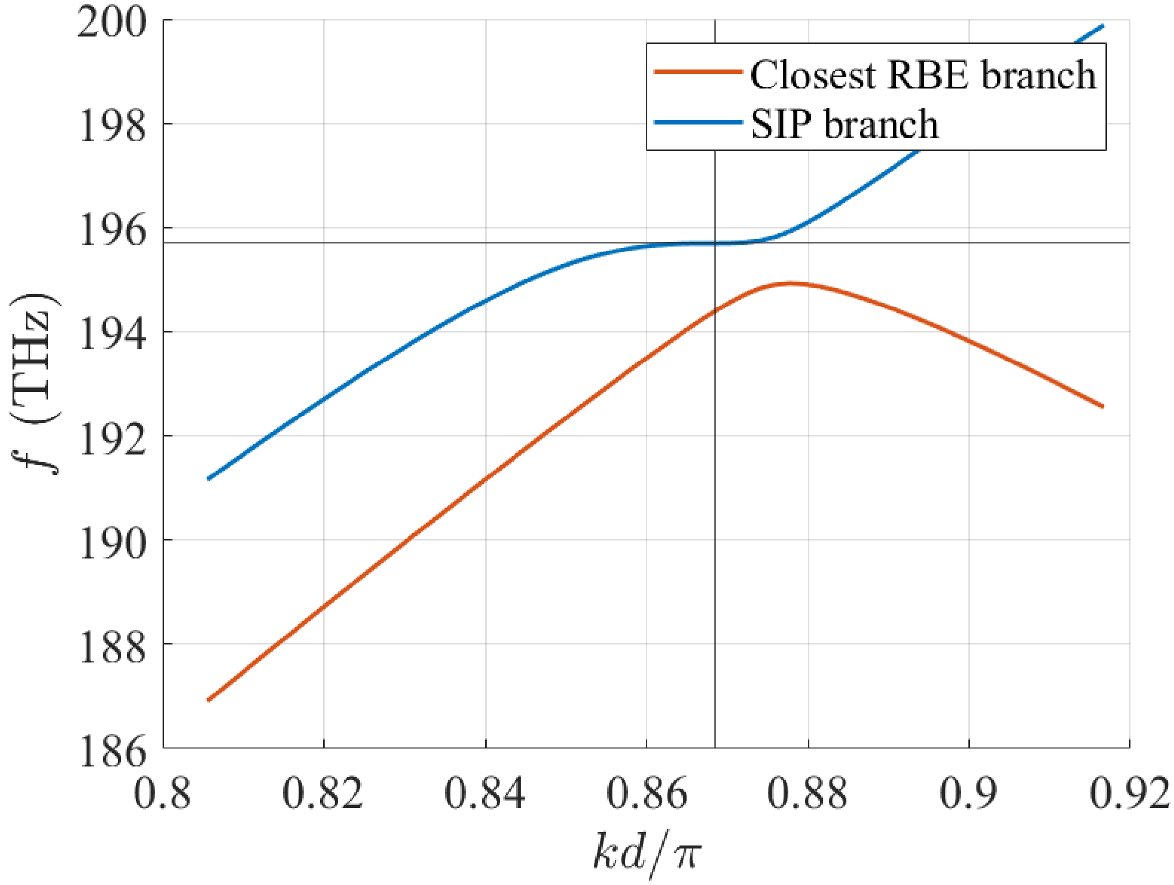

(a)

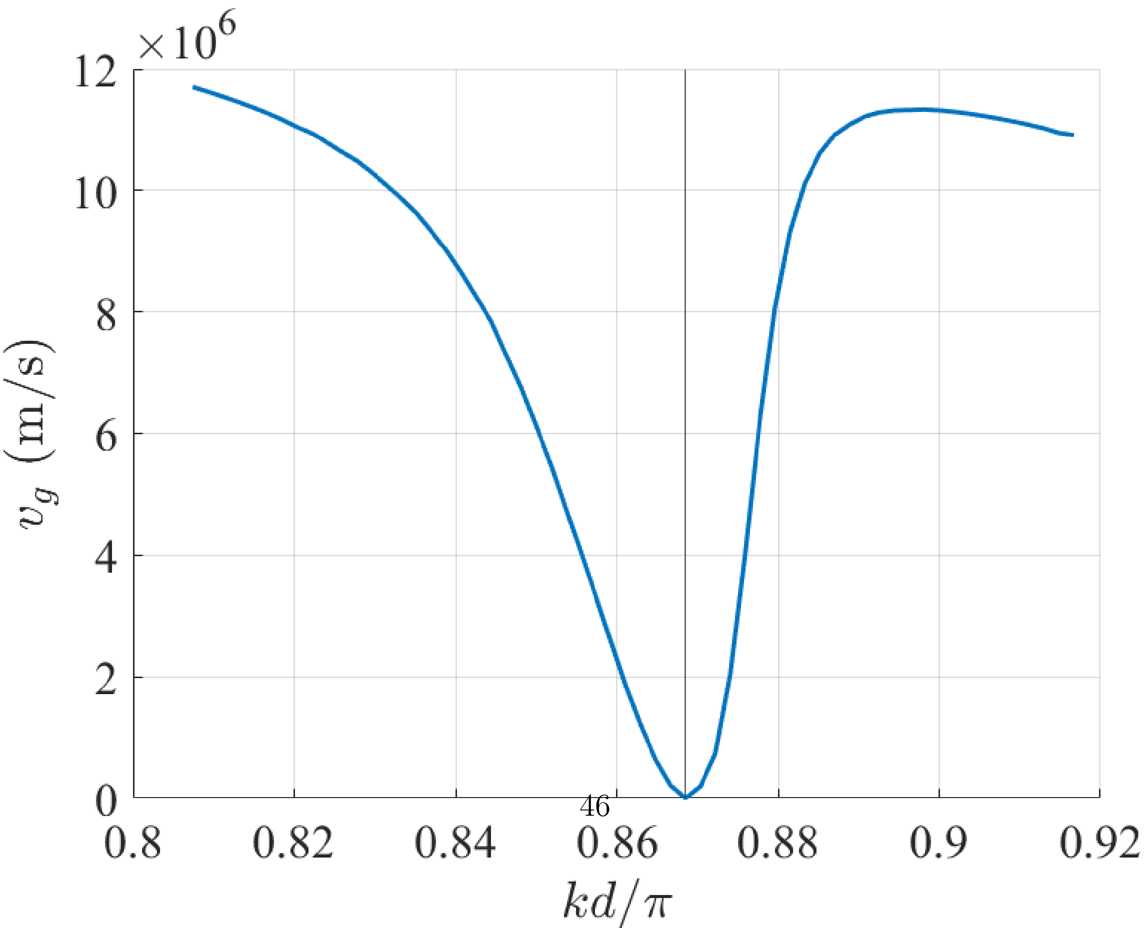

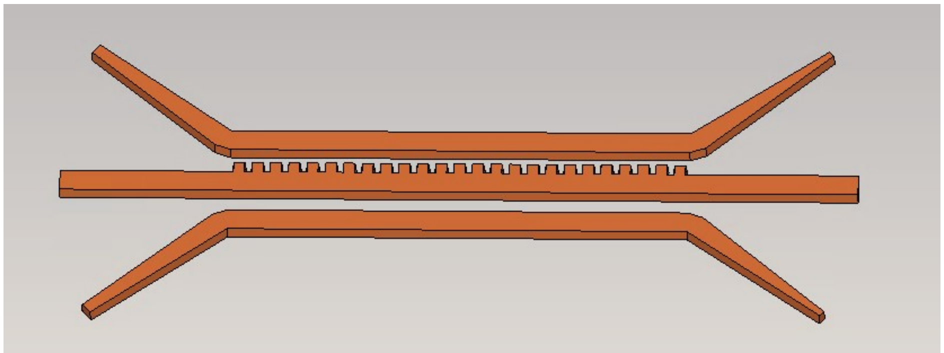

(a)

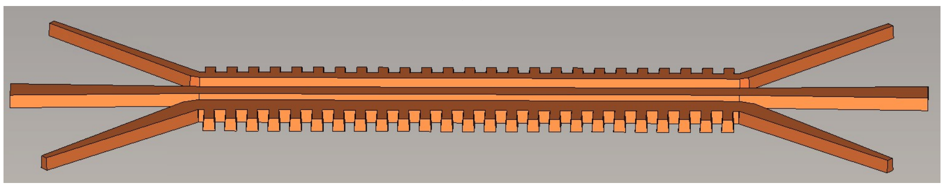

(b)

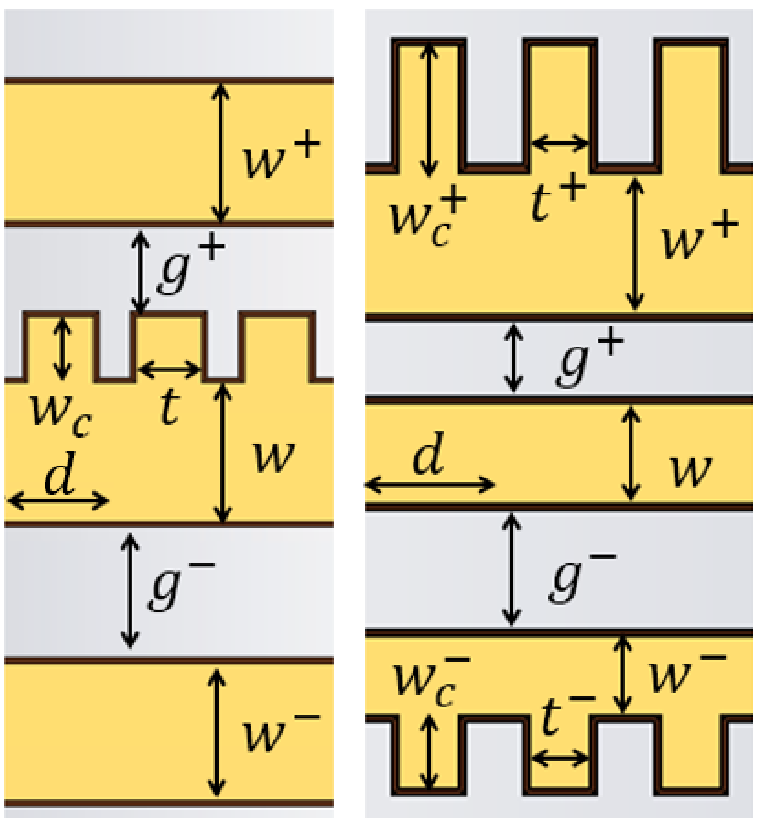

(c)

Figure 3.2: Schematic representations: (a) TWG1 waveguide with a central grating side-coupled to two straight waveguides; (b) TWG2 waveguide made of a central straight waveguide side-coupled to two grating waveguides; (c) top view of the two TWG1 and TWG2 waveguides showing the unit cells.

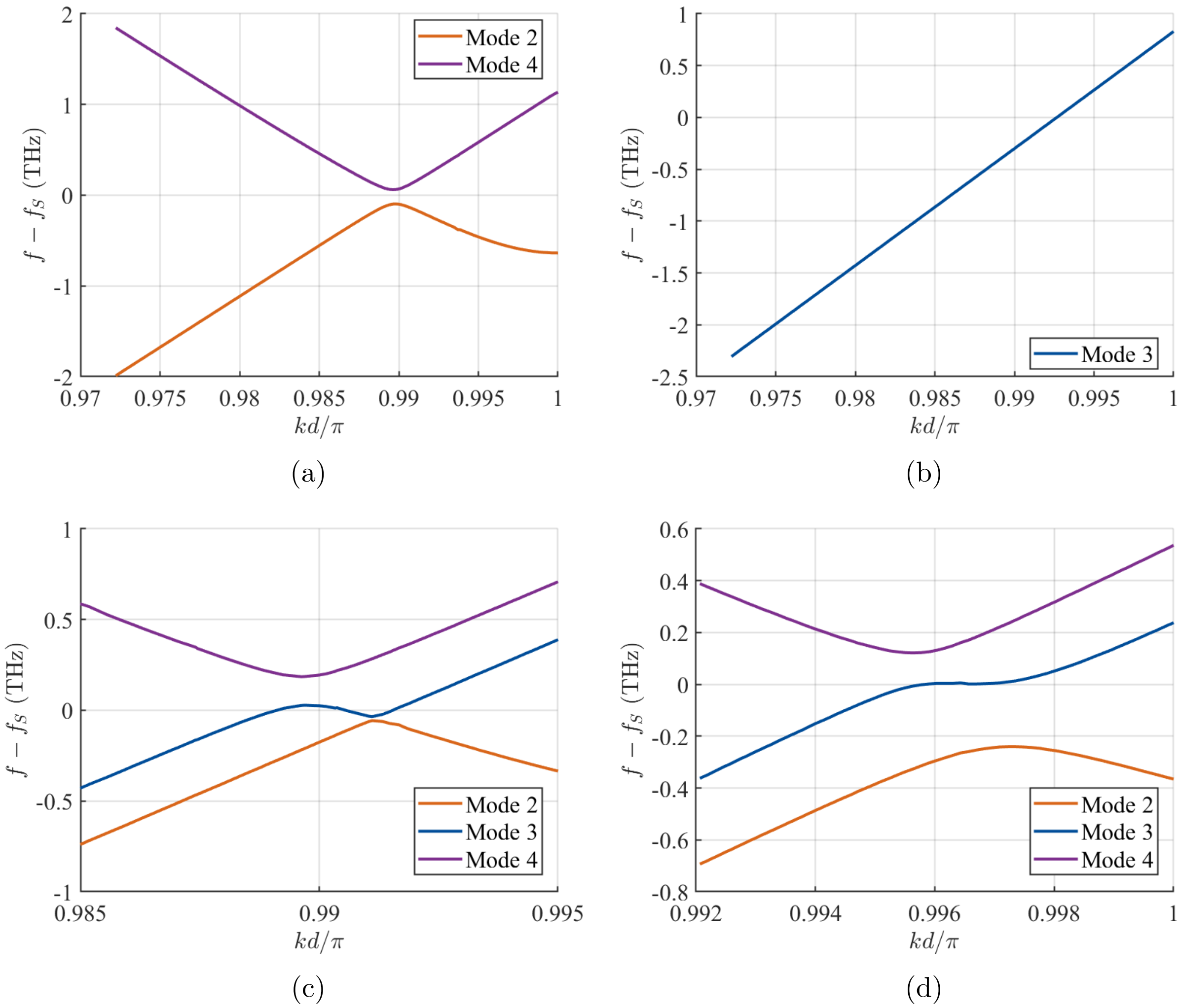

Figure 3.3: Design steps for creating a stationary inflection point (SIP)-based frozen mode photonic integrated circuit (PIC) using the TWG1 configuration. (a) Dispersion diagram of a grating coupled to a straight waveguide, with parameters selected to open a bandgap near the target point (k_S, f_S). (b) Dispersion diagram of an isolated straight waveguide showing a mode near the same target region. (c) Dispersion diagram of the TWG1 configuration, formed by adding the additional waveguide from (b) to the grating–straight waveguide pair in (a). The resulting structure produces the blue dispersion curve with a local maximum and minimum near the target point (k_S, f_S). (d) Optimized TWG1 dispersion diagram after adjusting waveguide gap sizes, where a stationary inflection point (SIP) emerges at the target (k_S, f_S) location (blue curve).

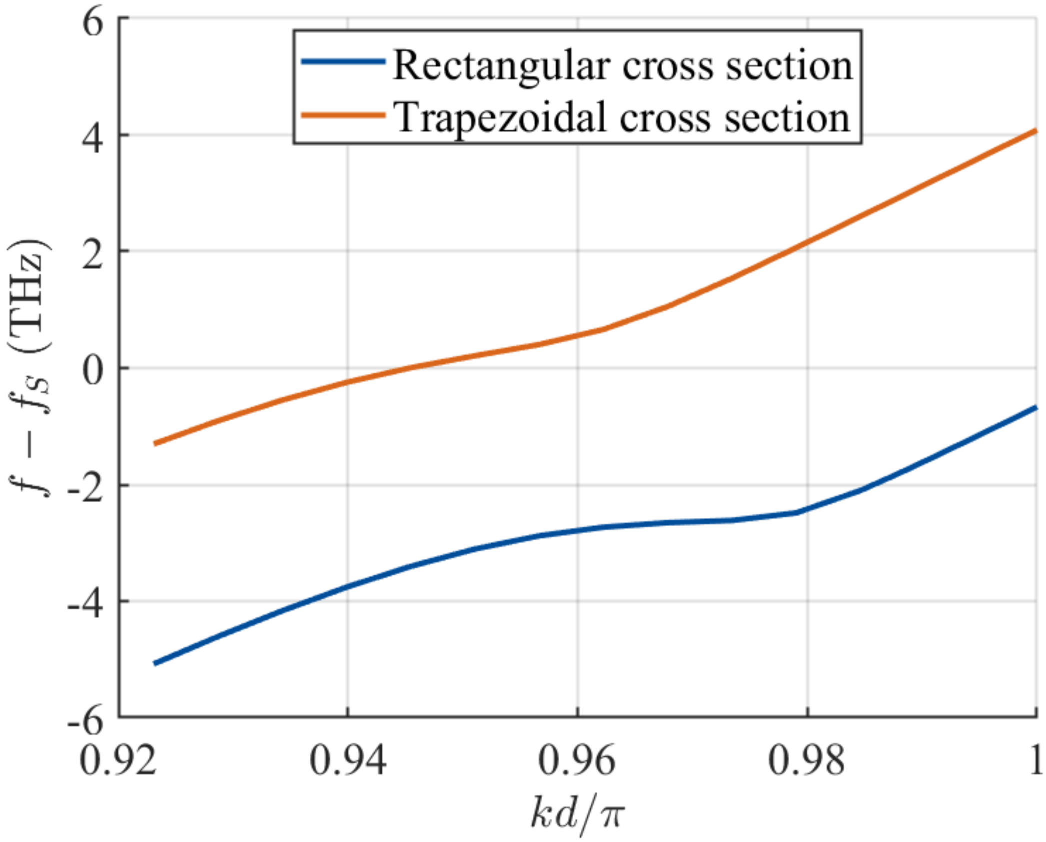

Figure 3.4: Dispersion diagram of the SIP-TWG2A waveguide with a rectangular and a trapezoidal cross section. The trapezoidal geometry alters the mode profile. This slightly disrupts the SIP condition, which must be restored through fine tuning of the waveguide parameters.

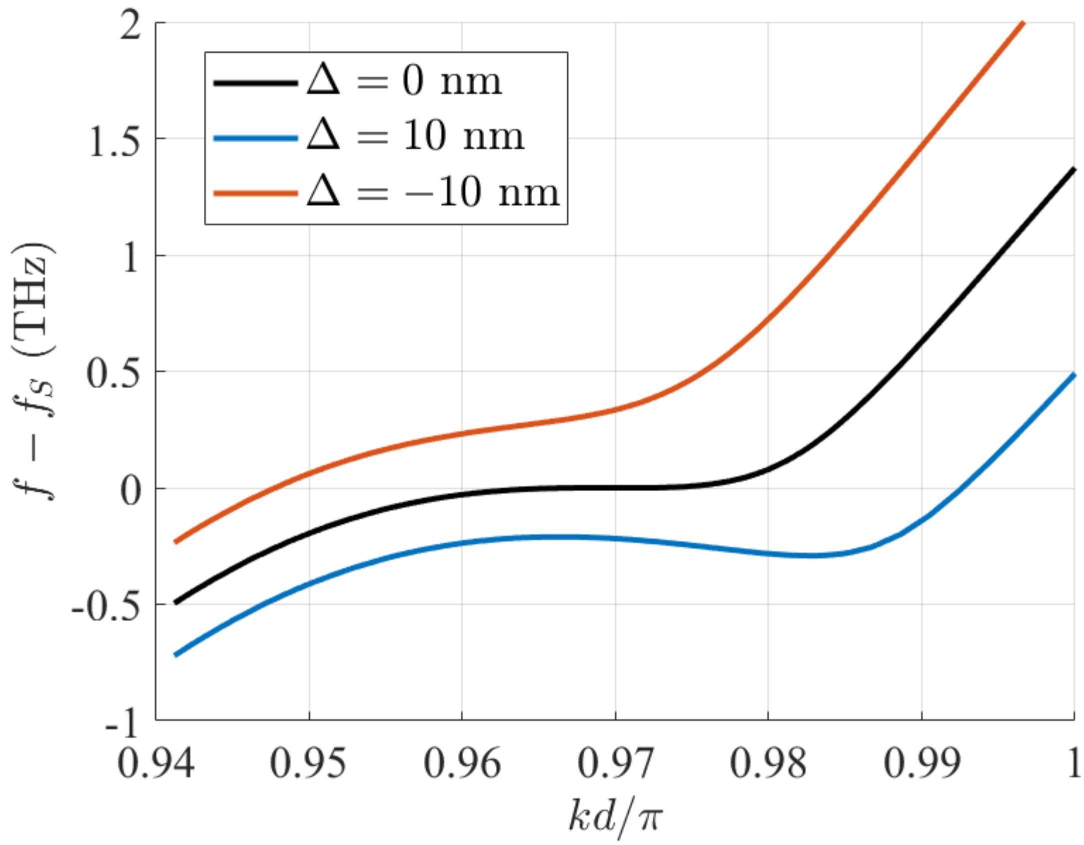

Figure 3.5: Dispersion diagram of the TWG2RB design showing the nominal case (black), and variations with waveguide widths increased (blue) and decreased (red) by $\Delta = 10$ nm. The SIP condition is sensitive to these changes, highlighting the importance of designing for robustness to perturbations.

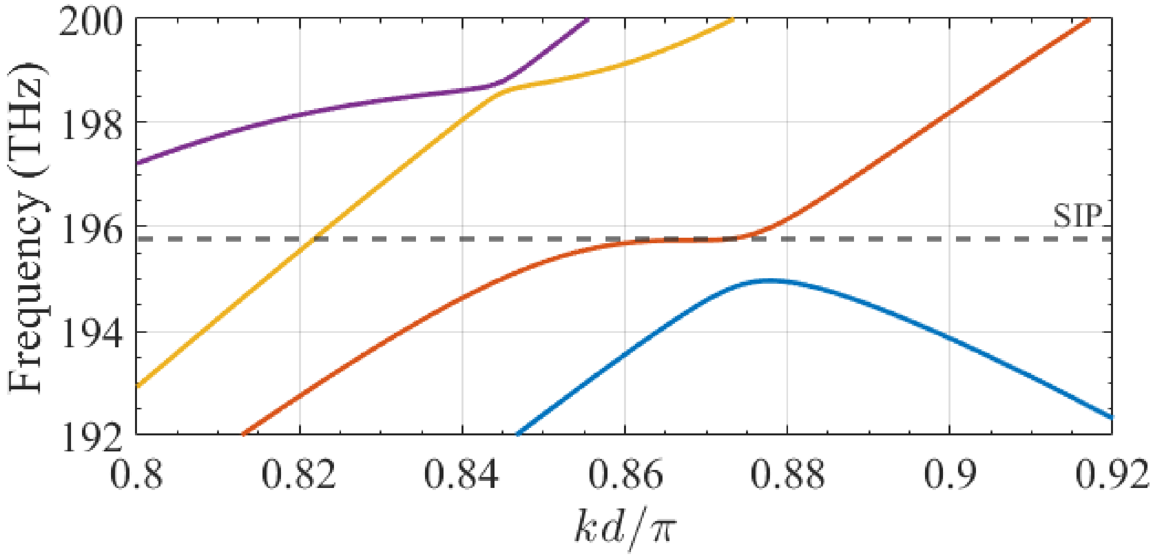

Figure 3.6: Dispersion diagram of the SIP-TWG2RA waveguide with a trapezoidal cross section. The three real-wavenumber modes closest to the SIP mode (orange curve) are also shown. The closest RBE is 1 THz lower than the SIP.

Chapter 4

Advancements in Degenerate Distributed Feedback Lasing

In this chapter, we advance concepts in lasing in a double grating photonic structure that operates near an exceptional point of degeneracy (EPD) of fourth order. The so-called degenerate DFB (DDFB) laser relies on lasing near an exceptional degeneracy involving four different Bloch eigenmodes, known as a degenerate band edge (DBE), to achieve a robust single-frequency lasing regime. A DDFB photonic cavity operating close to the DBE frequency is shown to display a large quality factor that scales with the fifth power of the cavity length. Upon the inclusion of gain, the DDFB cavity displays an exceptionally low lasing threshold that scales as the inverse of the fifth power of the double grating length, i.e., $\alpha_{D,th} \propto 1/N^5$, where N is the number of waveguide unit cells making the mirrorless cavity. The work proposed here shows a path to single-frequency lasing mode using a mirrorless cavity with minimal device footprint. The DDFB laser is very attractive for various applications including communications, sensing, and spectroscopy.

4.1 Introduction

The ability of lasers to generate coherent, monochromatic light makes them essential for high-speed data communications, sensing, and other cutting-edge technologies. Distributed feedback (DFB) lasers are a type of laser diode widely used in these applications due to their stable single-frequency lasing mode operation and narrow linewidth [123, 124, 125, 126]. The DFB laser relies on a distributed feedback mechanism along a single-path waveguide, where the two propagating optical waves are coupled via a longitudinal grating (i.e., a corrugated structure along the direction of propagation of the guided waves) in the material. While the DFB mechanism provides a stronger frequency selectivity than conventional Fabry-Perot cavities, it tends to provide two lasing frequencies which are sensitive to perturbations in the temperature or in the boundary conditions of the structure. Usually, a defect is included in the cavity to provide increased stability [127, 128]. The DFB laser also requires introducing antireflective coatings on the sides of the DFB structure to suppress the Fabry-Perot modes in the cavity and avoid multi-mode lasing [129]. Furthermore, putting a mirror on one side of the DFB structure and an antireflective coating on the other side may create an unbalanced situation that would cause another frequency shift. Affordable DFB lasers with high performance are therefore challenging to produce due to the costly and complex fabrication processes of high-end laser diodes required for single-mode operation [130]. To enhance the performance of DFB lasers, this work proposes the degenerate DFB (DDFB) laser.

Based on the double grating photonic structure introduced in [131], the DDFB lasing mechanism leads to single-frequency lasing mode operation through a degeneracy between four different Bloch propagating and evanescent eigenmodes (whereas a DFB laser generally uses two propagating modes in the longitudinal grating). This regime, which is associated with the formation of a degenerate band edge (DBE) in the Bloch dispersion relation of the waveguide [99, 17, 47, 113, 132, 68, 5, 133], is characterized by vanishing group velocity, enhanced field amplitude [4], and enhanced local density of states [68]. The DBE is a fourth-order

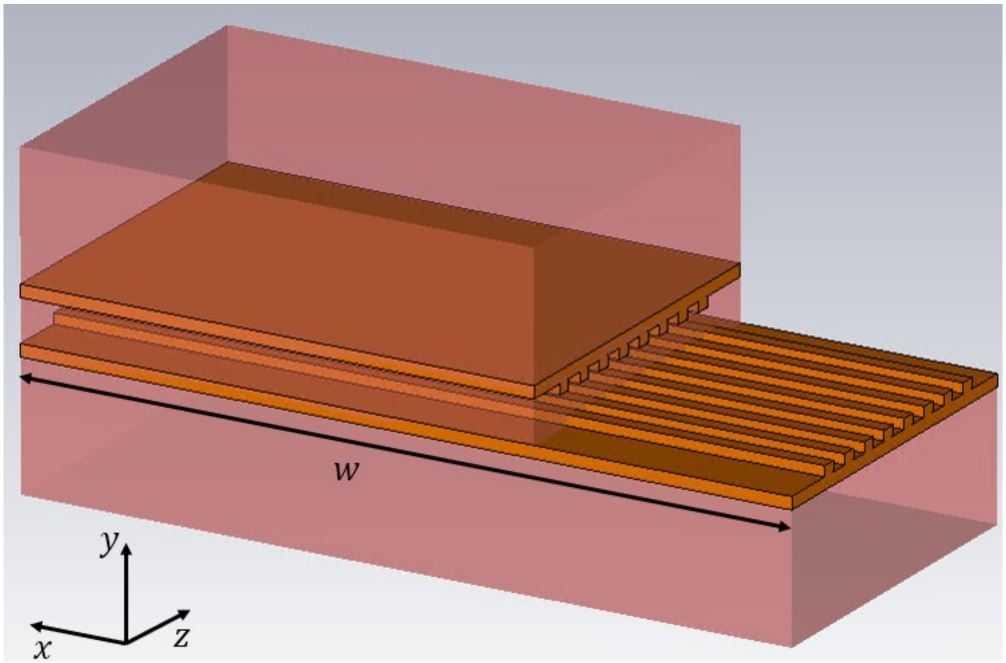

Figure 4.1: Schematic realization of the three-dimensional double grating making the mirrorless DDFB cavity with length of N unit cells along z and width w. The top part is truncated in the drawing to better show the three-dimensional structure. Also, N in this figure is much smaller than N considered in the rest of the paper.

exceptional point of degeneracy (EPD), as demonstrated in [5], that is associated with a very flat band of the dispersion diagram. EPDs are points in the parameter space of a system where the eigenvalues and eigenvectors collapse, or coalesce, on each other [76, 78]. EPDs in photonic systems can exist in the presence of balanced gain and loss, as in PT-symmetric systems [79, 81], and also in lossless and gainless structures as shown in [99, 17], even though the authors did not use the term EPD, and in [5, 66].

The DDFB mechanism discussed here is based on an EPD belonging to this latter class, i.e., a fourth-order EPD in a waveguide without loss and gain called DBE where a very flat dispersion diagram occurs [5]. When operating near the DBE frequency, the waveguide displays a large group delay which increases as the fifth power of the waveguide length, in agreement with the literature [4, 132, 5, 68, 134, 66]. Based on previous theoretical studies on DBE-based lasing [68, 66], once an active material is included [96], the DDFB photonic structure exhibits an enhanced interaction between the gain medium and the degenerate

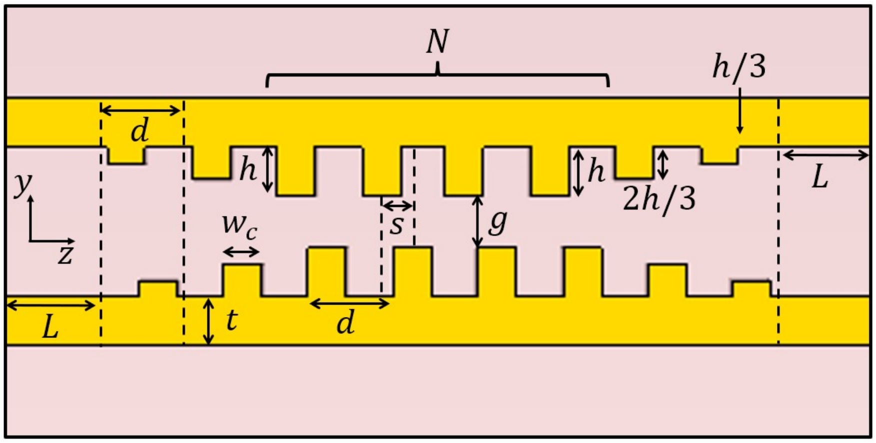

Figure 4.2: Double grating supporting guided longitudinal modes in the z direction, polarized along x. The two oppositely-facing gratings are shifted by a distance s along z to break mirror symmetry, enabling the occurrence of the DBE that has a very flat band in the dispersion diagram provided by Eq. (4.2). The tapering is performed by adding two cells at either end of the structure whose corrugation height decreases by $h/3$ consecutively. Termination regions of length L are added beyond the tapering sections, and their interface is denoted by vertical dashed black lines. The double grating supporting only an RBE used for comparison purposes has mirror symmetry, i.e., $s = 0$.

mode, which generates oscillations. The active DDFB waveguide displays a remarkably low lasing threshold that is here demonstrated to scale as the inverse fifth power of the waveguide length, and that lasing near the DBE frequency is preferred over lasing near the closest regular band edge in the same cavity. We additionally show that a DFB waveguide with the same structure and similar dimensions, supporting only a standing wave Bloch-mode degeneracy at a comparable frequency, exhibits a quality factor scaling as the cube of waveguide length and a lasing threshold scaling inversely with the cube of the length.

The fundamental concept of leveraging regular band edge effects to enhance lasing efficiency was analyzed in [94]. A preliminary concept of the DBE laser was published in [66] based on an ideal coupled mode theory, ideal gain mechanism, and without specifying a realistic structure at optical frequencies. Here, however, as in [131], we implement the DBE in a realistic double grating photonic structure, combining the DFB mechanism with the degenerate mode. Furthermore, the lasing threshold is obtained using full-wave electromagnetic simulations. The resulting DDFB lasing cavity does not require the introduction of defects within, and it provides a comparatively lower lasing threshold than the DFB cavity. Consequently, a DDFB laser shows promise in low-power optical telecommunication systems. In summary, the DDFB laser may offer several advantages over traditional DFB lasers due to the synchronized oscillation of the four degenerate waveguide modes. These advantages include enhanced light-matter interactions, narrower line width, reduced lasing threshold, and increased resilience to external perturbations. An analogous concept has been introduced at radio frequency in [135, 136] and experimentally demonstrated in [137].

This paper is organized as follows: Section 4.2 defines the double grating design, following the approach outlined in [131]. In Section 4.3, we introduce the design considerations and parameters for the waveguide to support a DBE in its modal dispersion relation and investigate its performance without gain. Section 4.4 provides the inverse fifth power scaling of the lasing threshold with cavity length when gain is introduced in the double grating, and how the lasing threshold depends on the reflection coefficient at the two cavity terminations. The performance of a future DDFB laser compared to that of a comparable DFB laser is discussed throughout the paper. The results are summarized in Section 4.5.

4.2 Double grating distributed feedback waveguide

The DDFB photonic structure advanced here features a double grating configuration where a standard grating is coupled with another grating. The second grating is obtained after performing a mirror operation with respect to the x, z plane and a translation s in the z direction. The waves in each optical grating couple with the waves in the other grating, forming a coupled double grating structure that supports four modes (when considering both directions). The translation s breaks mirror symmetry, which would otherwise prevent the formation of a four-wave degeneracy (the DBE) in two coupled periodic waveguides. The example of the double grating, shown in Fig. 4.1, is based on silicon-on-insulator (SOI) technology, although it can be built with photonic materials (such as SiN, InP, $LiNbO_3$, GaAs, AlGaAs, etc). In periodic media, Bloch modes with small group velocities display a strong impedance mismatch with the external waveguide connections [138, 139]. Hence, the coupling efficiency of light from an external medium into the slow-wave modes in the cavity is inversely proportional to the group velocity of the Bloch mode [140]. To slightly mitigate the abrupt discontinuities at the cavity terminations, and also to partially decrease radiation induced by an abrupt change in waveguide periodicity [141, 142], we taper the last two unit cells on each side by reducing the corrugation height h by one-third, as shown in Fig. 4.2. This tapering aims to reduce radiation losses caused by abrupt changes at the edges of the cavity and potentially improve coupling with external waveguides. The two unit cells involved in the tapering on each side are henceforth not included in the number of unit cells N of the finite-length cavity.

Beyond the tapering, the cavity is connected to straight uniform waveguides with the same thickness t as the rest of the slab. The junction point is denoted by the vertical dashed black lines in Fig. 4.2, which schematically depicts the double grating configuration with tapers and terminations.

We show an example of a double grating waveguide with a silicon core with a refractive index of $n_{Si} = 3.45$, and a silicon dioxide cladding with a refractive index of $n_{SiO_2} = 1.44$ [143]. We assume the materials do not exhibit dispersive behavior in the small frequency range of interest [120], that is, around the DBE frequency $f_D = 193.27$ THz.

We assume that the width w of the coupled gratings is much larger than the wavelength, as shown in Fig. 4.1 and we assume also that the field is invariant in the in the x direction. Hence, due to the field invariance in x, to reduce the computational cost we perform quasi 2D simulations using a width w that is much less than the wavelength and two walls of perfect electric conductor (PEC) boundaries orthogonal to x.

Our objective is to obtain longitudinal modes that propagate in the z direction and are polarized in the x direction (using the coordinate system as shown in Figs. 4.1 and 4.2). The modal dispersion relation of the longitudinal modes in the infinitely-long double grating structure is obtained by modeling one unit cell of the waveguide in the eigenmode solver of CST Studio Suite with phase-shift periodic boundary conditions for a unit cell. The computational domain is terminated by four PEC walls, two orthogonal to the x direction and two orthogonal to the y direction. Along the y direction, the two PEC walls are sufficiently far from the double grating to avoid interference with the evanescent field in the cladding of the longitudinal modes. We verify this by varying the PEC wall distance from the waveguide core and confirming the results remain consistent. Additionally, we also performed checks using perfect magnetic conductor (PMC) boundaries instead, orthogonal to the y direction, obtaining the same result.

4.3 DBE resonance in a DDFB Cavity

The lossless and gainless double grating configuration supporting a DBE at f_D (known as the DDFB waveguide or double grating) is found via a combination of manual and numerical parameter optimization where the second derivative of the dispersion, $d^2\omega/dk^2$, of the Bloch modes at the edge of the Brillouin zone $k = \pi/d$ is minimized, i.e., $|d^2\omega/dk^2|_{\pi/d} \to 0$. Minimizing the magnitude of this derivative ensures the Bloch degeneracy involves all four modes supported by the double grating shown in Fig. 4.2. Minimizing just the magnitude of the group velocity $|v_g| \to 0$ may result in the formation of an RBE instead. The continuous lines in Fig. 4.3 show the real-wavenumber branches of the modal dispersion diagram of the DDFB design with the following parameters (in nm): $t = 81$, $s = 119$, $d = 335$, $h = 102$, $g = 214$, and $w_c = 92$. The solid-orange curve denotes the modes that coalesce at the DBE frequency $f_D = 193.27$ THz with the typical very flat band edge, whereas the solid-blue curve at lower frequencies denotes the modes that coalesce forming a regular band edge (RBE) that occurs in the same double grating structure. The RBE is a second-order degeneracy involving only the coalescence of two counter-propagating Bloch modes in the waveguide, which form a standing wave [99]. Typically, a DFB laser operates in the vicinity of an RBE (generally referred to only as band edge) [144], whereas the DDFB operates in close proximity to the DBE. Near the RBE frequency f_R, the dispersion diagram is approximated as [99]

$$(f_R - f) \approx \frac{h_R}{2\pi}(k - k_R)^2, \tag{4.1}$$

whereas at frequencies near the DBE, the dispersion diagram is approximated as [99, 17, 88, 113, 133]

$$(f_D - f) \approx \frac{h_D}{2\pi}(k - k_D)^4, \tag{4.2}$$

where k_R and k_D are the wavenumbers at the DBE and the RBE, respectively (in this case, it is π/d for both cases). The parameters h_R and h_D indicate the flatness the band edges and are sometimes called the "flatness parameter". In this case, the band edge separates a pass band from a stop band at higher frequencies; therefore, both h_R and h_D are positive. At the DBE, $d^n\omega/dk^n = 0$ for $n = 1, 2, 3$, and $d^4\omega/d_k^4 = -24h_D$. Though not shown in Fig. 4.3 because only the propagation branches are shown, there are four modes coalescing at the DBE when considering also the evanescent modes. This can be easily seen by considering the four quartic roots $(k - k_D) \approx [2\pi(f_D - f)/h_D]^{1/4}$ as clearly shown in [47, 5, 66, 19, 131]. Above the DBE frequency f_D, all four modes are evanescent for the case represented in

Fig. 4.3.

To compare the performance of DFB and DDFB cavities, we introduce another double-grating configuration that supports *only* an RBE (close to the DBE frequency of the DDFB design), and which is henceforth referred to as the DFB double grating or DFB cavity (shown on the top right of Fig. 4.3). In this double-grating RBE design we impose mirror symmetry (by letting $s = 0$), which prohibits the formation of the DBE, and use the same period $d = 335$ nm and comparable waveguide dimensions. The other parameters of the DFB design are (in nm): $t = 80$, $h = 100$, $g = 350$, and $w_c = 80$. Its real-branch modal dispersion diagram is shown with the dashed-yellow line in Figure 4.3. At the edge of the Brillouin Zone $k = \pi/d$, the dispersion of the DDFB design (solid lines) displays a much greater flatness than that relative to a regular DFB design (dashed lines), as seen by comparing the solid orange curve with the yellow dashed one. The reason for the flatter modal dispersion around the DBE frequency compared to the RBE frequency in Fig. (4.3) is that the flatness at the RBE frequency is only due to the coalescence of two modes, whereas the flatness at the DBE frequency is associated with the two propagating waves and two evanescent waves composing the four degenerating modes [48].

Next, we consider a double grating cavity made of N unit cells. For the cavity to display the properties associated with the DBE, a cavity resonance must occur in proximity to the DBE frequency. We call the resonance closest to the DBE the "DBE resonance" with associated frequency $f_{r,D}$, as in [145, 113, 5, 133, 66]. The DBE resonance frequency of the cavity becomes closer and closer to the DBE frequency when increasing the cavity length, following the asymptotic law

$$f_{r,D} \sim f_D - \frac{h_D}{2\pi}\left(\frac{\pi - \varphi}{Nd}\right)^4, \tag{4.3}$$

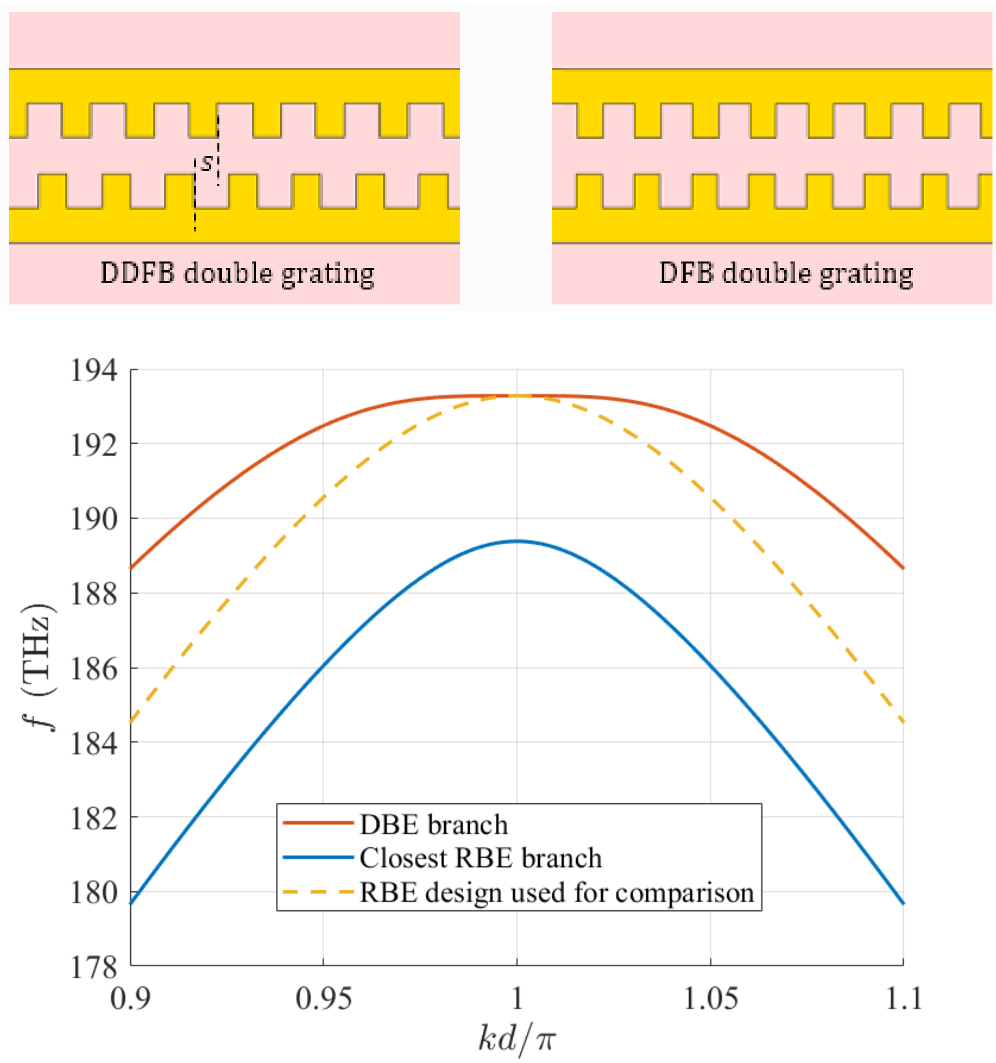

Figure 4.3: Dispersion diagrams of the longitudinal modes for the DDFB and DFB double grating designs. The DDFB double grating has two modal branches (orange and blue solid lines). The branch that includes the four-mode coalescence at the DBE frequency f_D = 193.27 THz is depicted as a continuous orange curve. The evanescent modes coalescing at the middle of the flat-band edge are not shown in the figure. The branch showing the closest RBE at 189.38 THz is depicted as a continuous blue curve. The dashed yellow line represents the modal dispersion diagram of the DFB double grating design with mirror symmetry (i.e., with $s = 0$) that supports only an RBE at a frequency close to f_D, for comparison purposes. The flatness associated with the DBE (see Eq. (4.2)) is noticeably greater than those associated with the RBEs in the two designs.

where $\sim$ denotes asymptotic equality for large N, as discussed in [113, 68, 134, 5, 133, 66]. The angle φ represents a reflection phase of each propagating mode at the edges of the cavity, where also the evanescent waves are strongly excited [113]. The smaller the flatness parameter h_D is, the closer the DBE resonance frequency is to the DBE frequency. (Note that the asymptotic formula reported in [134, 5, 133, 66, 19] should have included also the term φ). Similarly, for the DFB cavity, the resonance closest to the RBE frequency is known as the "RBE resonance" with associated frequency $f_{r,R} \sim f_R - h_\mathrm{R}(\pi/2)/(Nd)^2$.

The resulting frozen mode in the DDFB cavity exhibits comparatively larger field amplitude enhancement and group delay compared to the RBE-associated slow wave resonance [99, 4]. As a result, waveguides operating near the DBE often demonstrate enhanced performance compared to those operating near an RBE [4, 68, 5, 133].

The existence of the DBE at optical frequencies has been experimentally demonstrated in silicon photonic waveguides, as reported in Refs.[132, 58]. These works confirmed the DBE by reconstructing the dispersion diagram and by observing the characteristic quality factor scaling $Q_D \sim N^5$ at the DBE resonance frequencies of cavities made by N unit cells. Additional experimental evidence of the DBE has been reported at microwave frequencies, for instance in [134, 19].

The optical properties of the finite-length DFB and DDFB waveguides are obtained using the FEM solver in CST Studio Suite. In the following simulations, excitation is applied from the left side of the cavity using the even mode of the waveguides at a distance L from the corrugations, as shown in Figure 4.2).The amplitude of the excited mode at the input port is scaled such that the total power carried by that mode equals 1 W.

The quality factors of the lossless and gainless DFB and DDFB cavities are shown in Figure 4.4 for different numbers of unit cells N. Both quality factors are computed for a loaded double grating structure with tapering of the corrugations of two additional unit cells on

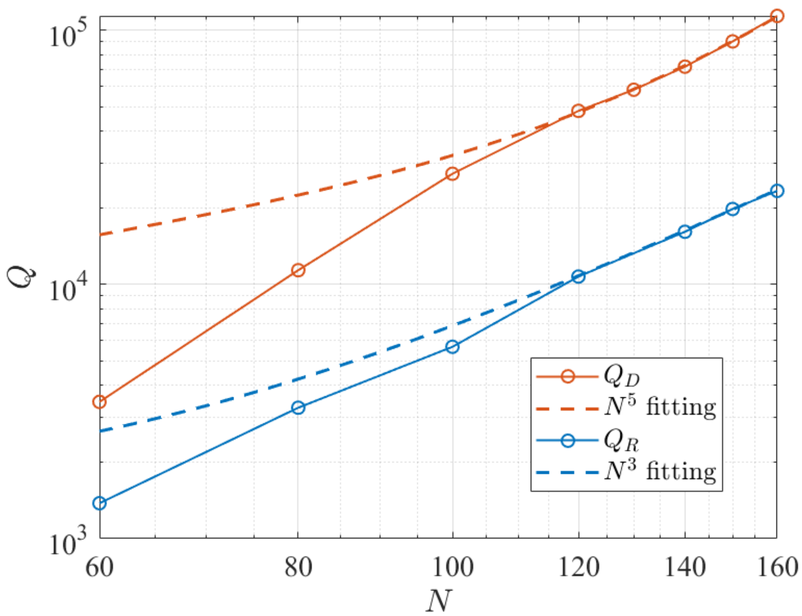

Figure 4.4: Comparison between the loaded quality factors of the DDFB (orange dots) and the DFB (blue dots) cavities (evaluated at their respective resonances) varying grating length. The dashed lines of the same color are the fitting functions that show the asymptotic N^5 scaling of the DBE quality factor Q_D with DDFB waveguide length (orange) and the N^3 scaling of the RBE quality factor Q_R with DFB waveguide length (blue). Both devices have the same period.

either side and uniform waveguides with thickness t, extended continuously on both sides (without mirrors) as illustrated in Figure 4.2. The junction point is denoted by the vertical dashed black lines.

The quality factors are calculated as $Q = \pi f_r \tau_g(f_r)$, where f_r is the resonance frequency for either the DDFB ($f_{r,D}$) or the DFB ($f_{r,R}$) cavity, and $\tau_g(f_r)$ is the group delay at that frequency calculated as [68, 5]

$$\tau_g(f) = \frac{1}{2\pi}\frac{\partial \angle S_{21}}{\partial f}, \tag{4.4}$$

where $\angle$ denotes the phase of the transmission S_{21} from input to output. The transmission is calculated using two ports, one on each side of the resonator along z. Each electromagnetic port spans both gratings in the transverse cross section and extends into the cladding to account for the evanescent fields surrounding the silicon cores. Unless explicitly stated, in the following simulations, $L = 0$ between the port location and the beginning of the coupled gratings.

In Figure 4.4, the orange dots represent the quality factors of the DDFB cavity Q_D, while those of the DFB cavity Q_R are shown as blue dots. The dashed lines of the same color represent their respective fitting trends; $Q_D \approx aN^5 + bN$ for the DBE, where $a = 6.93 \times 10^{-7}$ and $b = 252.18$, and $Q_R \approx cN^3 + d$ for the DFB, where $c = 0.0054$ and $d = 1.478 \times 10^3$. The first term of the Q_D fitting function dominates when $N > 138$, whereas that of the Q_R fitting function dominates for $N > 64$, demonstrating that these fittings describe the asymptotic scaling of the quality factor with waveguide length. The observed N^5 and N^3 asymptotic scaling laws are consistent with the literature for both degeneracies [4, 132, 68, 5, 133, 134]. Besides the two completely different scaling laws, we also observe that the quality factor of the

DDFB cavity is larger than that of the DFB cavity for any N, owing to the exceptional four-mode degeneracy. This result demonstrates that the DBE-associated frozen mode regime in the DDFB design experiences greater impedance mismatch at the cavity terminations compared to the RBE-associated resonance of the DFB design. Consequently, the DDFB laser is anticipated to achieve lasing with a lower lasing threshold without mirrors and to be more resilient to perturbations of its terminations than the DFB laser. This strong mismatch occurs because at the DBE resonance both the coalescing propagating and evanescent modes together are necessary to satisfy the boundary conditions at the two edges of the cavity. Since they have almost coincident polarization states because of the four-wave degeneracy [4, 146], both types of waves have to be large to reconstruct the field at the terminations. This phenomenon results in having propagating modes with large magnitude causing the field enhancement at the interior of the cavity, away from the terminations. This DBE-related phenomenon is substantially different from what happens in conventional uniform Fabry-Perot cavities or in a DFB cavity where there are no evanescent waves needed to satisfy the boundary conditions at the terminations.

The quality factors of the DDFB and DFB cavities can be controlled to some degree by resorting to the concept of waveguide impedance. Figure 4.5 depicts the change in the loaded quality factors of the DDFB (orange dots) and DFB cavities (blue dots) with $N = 60$ as a function of the reflectivities Γ of its terminations at their respective DBE and RBE resonances. Only the case with a relatively small $N = 60$ is shown here to limit the computational burden.

For simplicity, and without losing generality, in this paper we refer to the mirror effect at the two edges of the cavity using the field reflectivity

$$\Gamma = \frac{\eta_t - \eta_w}{\eta_t + \eta_w}, \tag{4.5}$$

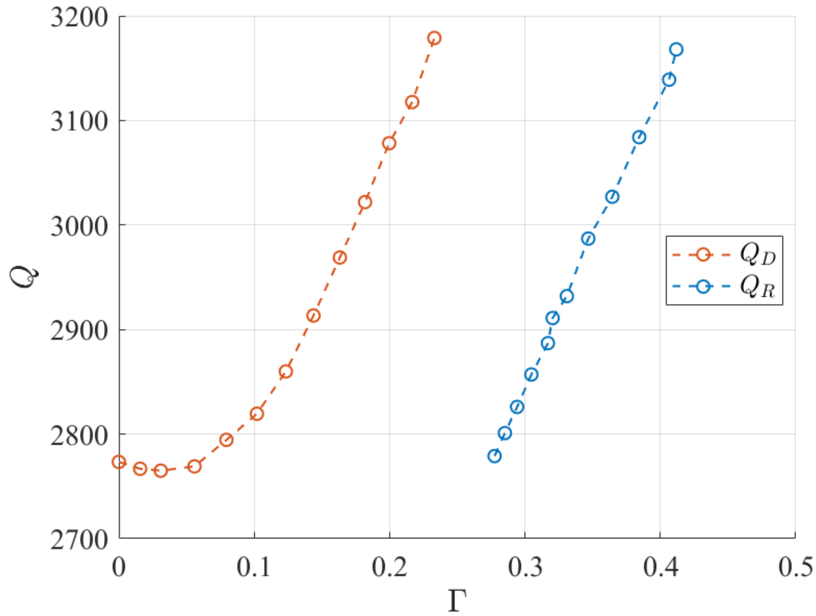

Figure 4.5: Loaded quality factor of the DDFB cavity (orange dots) and of the DFB cavity (blue dots) for $N = 60$ unit cells, against waveguide reflectivity Γ at each of the four terminations. The DDFB cavity does not require waveguide reflectivity at its terminations. Even with vanishing reflectivity, the DDFB cavity has a Q comparable with that of the DFB cavity with higher reflectivity. Note that the DDFB cavity is more resilient to perturbations of its terminations than the DFB cavity.

where η_w and η_t are the wave impedances of the cavity waveguides and outside waveguides (used as "terminations"), respectively. We approximate $\eta_w \approx \sqrt{\mu_0/\epsilon_w}$ where ϵ_w is the *effective* permittivity of the even mode of the two straight coupled waveguides inside the DDFB cavity, without the corrugations. Similarly, $\eta_t \approx \sqrt{\mu_0/\epsilon_t}$, where ϵ_t is the *effective* permittivity of the even mode of the two straight coupled waveguides outside the DDFB cavity, used as termination. We use the ε_w of the even mode of the coupled waveguides, although using the odd mode effective permittivity would yield similar results. It is important to note that this definition of Γ by far does not capture the exact reflectivity at the cavity terminations, which would require a tensorial treatment of the Bloch impedance (see [147] for details on Bloch impedance behavior near EPDs), but it provides only a convenient metric to quantify the additional mirror effect due to the straight waveguide impedance mismatch at the cavity ends. For instance, $\Gamma = 0$ indicates that no straight waveguide impedance discontinuity is present, i.e., the cavity is continued with the same waveguides without any additional mirror effect other than the natural mismatch of the Bloch wave impedance of the DBE mode due to the double periodic grating. An analogous metric is used to quantify the mirror effect at the two ends of the DFB cavity made of two parallel gratings with $s = 0$ (i.e., with mirror symmetry) used for comparison purposes only.

In our simulations, the change in Γ is implemented by modifying the refractive index of the external waveguides' core, in the sections with length $L = 1.2$ μm on each side of the cavity. For the DDFB cavity, the distance between the last corrugation and the refractive index discontinuity (shown by two outermost vertical black dashed lines in Figure 4.2) is approximately 67 nm. For the DFB cavity, the distance is 127 nm. In practice, a distributed Bragg reflector (DBR) would be used to tailor the reflectivities [125] at the edges of the cavity, but here we prefer to use a simpler implementation to focus on the physics results associated with the cavity termination effect rather than on the design of a mirror. Since the DDFB cavity displays significantly larger quality factors than a DFB cavity of the same length, as seen in Figure 4.4, to achieve the same quality factor, the DDFB cavity requires much lower reflectivities than a DFB cavity of the same length. Actually, as visible in the plot, no reflectivity is needed for the DDFB cavity to have a large Q factor. Indeed, the quality factor of the DDFB cavity without reflectivity, i.e., with $\Gamma = 0$, is comparable with that of the DFB cavity of the same length with a higher reflectivity, $\Gamma = 0.3$. Additionally, the DDFB cavity is also shown to be more resilient to variations in the reflectivity Γ of its terminations than the DFB cavity, especially around the mirrorless $\Gamma = 0$ case, where Q_D varies with Γ and forms a small parabola. One of the major conclusions is that there is a large reflection at the two DDFB cavity terminations even when the cavity is made mirrorless, $\Gamma = 0$, i.e., when the two chirped waveguides are connected to two straight waveguides with the same thickness t and material and without corrugations.

The plots in Figure 4.6 show the field at the resonances of the (a) DDFB and (b) DFB cavities

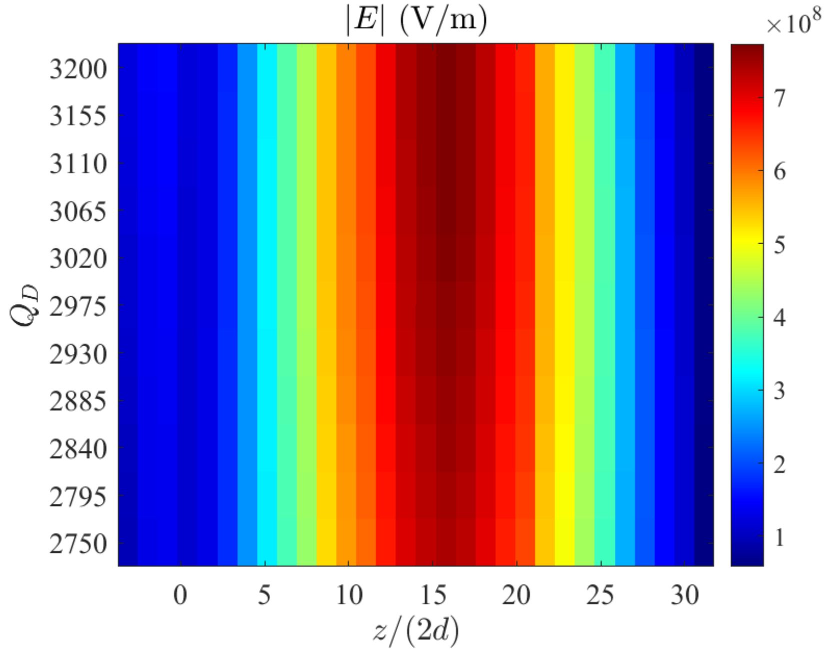

(a) DDFB cavity

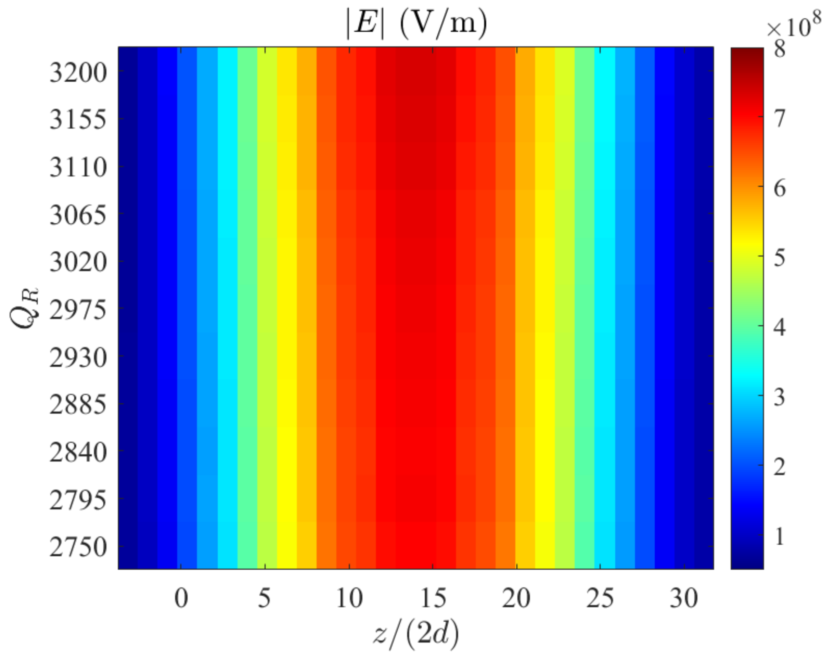

(b) DFB cavity

Figure 4.6: Electric field amplitudes inside the passive (a) DDFB and (b) DFB cavities with $N = 60$, evaluated at their respective structured resonances as a function of the loaded Q-factor of the cavity. The loaded Q-factor is tailored by adjusting the waveguide reflectivities Γ of the terminations. Each cell denotes the average of the field magnitude in two contiguous unit cells within a box of vertical length $t + 50$ nm and horizontal length $2d$ that includes the top waveguide. Note that the field amplitude within the DDFB cavity is stronger than in the DFB cavity, and that such difference grows with increasing N.

consisting of $N = 60$ unit cells as a function of the quality factor, which is controlled via the reflectivity of the cavities' terminations as shown in Fig. 4.5. The plotted fields in both figures correspond to those in the top waveguide, including the evanescent fields extending up to 25 nm above and below the core. The value of each cell in Figure 4.6 is determined as the average of the field magnitude over a box of total vertical thickness $t + 50$ nm, covering two consecutive unit cells along the z direction (the full extent of the corrugation is not included within the box). The strong field amplitudes away from the cavity's edge at the DBE resonance, especially compared to the field amplitudes at the RBE resonance for the same quality factor, demonstrate a uniquely "structured" resonance field that leads to an enhancement of the local density of states [68]. We observe a tight field confinement inside the DDFB waveguide at the DBE resonance that is consistent with the results reported in Ref. [131]. The large relative field magnitude inside the waveguide further confirms the DBE-associated frozen-mode behavior, especially compared with the fields in the DFB cavity of the same length and quality factor. The value of field enhancement in a cavity is markedly reliant on the topology, technology, and length of the optical waveguides (for instance, a different waveguide supporting the DBE reported in Ref. [133] provides a different field enhancement than the illustrative case provided here). In essence, the maximum field enhancement in a cavity with a DBE is generally larger than that of a comparable cavity with an RBE having the same Q factor, length, and analogous topologies. This is also seen in Ref. [66], and such an observation can be generalized to other implementations of cavities supporting a DBE and an RBE. Here we have shown the field enhancement for $N = 60$, however, the maximum field intensity in a DDFB cavity is expected to scale as N^4 near a DBE as demonstrated in previous pioneering work on DBE structures [99], whereas the field enhancement in a DFB cavity should scale as N^2. Also the *local density of states* has been demonstrated to follow the N^4 asymptotic scaling law in [68] in a previous case of a DBE cavity.

These results are important because they demonstrate the superior cavity effect of the DBE-associated frozen mode compared to that of the RBE-associated standing wave.

In summary, the DDFB cavity displays a larger quality factor than a DFB cavity of the same length, displaying a larger scaling power with waveguide length ($Q_D \sim N^5$ as opposed to $Q_R \sim N^3$). When the reflectivity of their terminations is tailored, the DDFB cavity necessitates lower waveguide reflectivities to have a Q of the same value as that of the DFB cavity. These results have been shown here for $N = 60$, but the difference in reflectivity to provide the same Q is even starker for larger N, owing to the N^5 and N^3 asymptotic scaling laws at the DBE and RBE resonances. Analogously, the difference between the maximum field enhancements in the two cavities has been shown only for $N = 60$ to simplify the numerical burden, but their difference is even stronger for larger N, owing to the N^4 and N^2 asymptotic trends for field enhancement at DBE and RBE resonances, respectively, as shown in Ref. [99]. Additionally, the quality factor of the DDFB cavity is more resilient to perturbations of the reflectivity of its terminations than the quality factor of the DFB cavity.

We have also shown that a DDFB cavity exhibits stronger fields away from the cavity's edges compared to a DFB cavity of the same length and quality factor. This happens with approximately half the reflectivity at the DDFB cavity edges than that of the DFB cavity when $N = 60$, with a starker difference expected for larger N.

4.4 DDFB-induced lasing threshold

The goal of this section is to show that the lasing threshold of a DDFB cavity is lower than that of a DFB cavity and determine the scaling law of the DDFB threshold versus grating length. To do so, we consider the gain to be uniformly distributed in the waveguide cladding (i.e., in the bulk) [98, 116]. There are various ways to add gain, including rare-earth material doping, current injection, and the use of quantum wells [96], which increase the field amplitude of the waves traveling in the cavity. Current injection is commonly used to add gain in DFB lasers [129].

Here, we describe the uniform distribution of gain in the cladding as the imaginary part $-n''_g$ of the complex refractive index $n = n_b - jn''_g$, where n_b is the bulk refractive index, and gain corresponds to $n''_g < 0$. Although the used FEM solver (CST Studio Suite) does not directly support a negative imaginary part of the refractive index, the solver allows for a complex relative permittivity. Using the procedure described in [148], we introduce gain to the simulation. The gain region includes the cladding between the two gratings, which increases the interaction between the waves and the gain medium [129]. The conversion between the bulk gain coefficient α_g (in units of dB/cm) and the gain in terms of the imaginary part of a refractive index at an angular frequency ω is approximated by $n''_g(\omega) \approx -\alpha_g(100/8.686)(c_0/\omega)$ where c_0 is the speed of light in vacuum. The complex permittivity of the cladding, ε is written as $\varepsilon = \varepsilon' - j\varepsilon''$, so its imaginary part is $-\varepsilon'' = \mathrm{Im}(n^2) = -2n_b n''_g$.

We define the lasing threshold α_{th} as the minimum amount of bulk gain necessary for an active cavity to start oscillating due to the generation of an instability [96, 125, 66]. Considering that the DBE quality factor scales asymptotically as $Q_D \sim N^5$ for increasingly large N [4, 132, 68, 5, 134], and that typically $\alpha_{th} \propto 1/Q$ [102], we anticipate the lasing threshold calculated at the DBE resonance exhibits an asymptotic scaling with waveguide length such that $\alpha_{D,th} \sim N^{-5}$, consistent with the literature [68, 66].

To determine the lasing threshold of a finite-length DDFB cavity, we gradually increase the gain while monitoring the cavity field for unstable behavior. This is done by tracking the poles of the S_{21} transmission parameter at the DBE resonance, as previously shown in Appendix A of [103], Appendix B of [149] or in [117] for other kinds of exceptional degeneracies. To ensure that lasing at a resonance $f_{r,D}$ near the DBE frequency $f_D = 193.27$ THz is preferred over lasing near the closest RBE at 189.38 THz in the same cavity (the blue curve in Fig. 4.3), we computed the lasing thresholds at the nearest resonances to the two exceptional points for $N = 60$ and $N = 120$ of the same structure. For $N = 60$, the lasing threshold at the DBE resonance (the closest one to the DBE frequency) is $\alpha_{D,th} = 505$ dB/cm, while that near the RBE resonance (closest to the RBE frequency) is $\alpha_{th} = 2390$ dB/cm, resulting in a 4.7 times larger value than the DBE one. For $N = 120$, we have that $\alpha_{D,th} = 40$ dB/cm and the threshold at the RBE resonance is $\alpha_{th} = 295$ dB/cm (that is 7.4 times larger than the DBE one). The lasing thresholds at resonances associated with the DBE are significantly lower than those associated with the nearest RBE. Therefore, in the double grating cavity of Fig. 4.2 that supports both the DBE and the RBE, lasing near the DBE frequency is preferred over lasing at the nearest RBE resonance.

We have just compared the DBE and RBE lasing threshold in the same cavity, assuming first $N = 60$ and then $N = 120$. Now we compare the thresholds in two different cavities made of two different double gratings: the DDFB one (with $s \neq 0$) and the DFB one (with $s = 0$). The DDFB cavity supports a DBE at f_D, and has threshold $\alpha_{D,th}$, whereas the DFB cavity supports an RBE at $f_R \approx f_D$ (shown in Fig. 4.3 with a dashed-orange line), and has threshold $\alpha_{R,th}$. The two thresholds are shown respectively as orange and blue dots in Figure 4.7 for different grating lengths N. The DDFB cavity lasing threshold is always smaller than the DFB one, for any N. The tapering in the cavities is the same as in the results depicted in Figure 4.4.

To determine the asymptotic scaling laws of the threshold for the two DDFB and DFB cavities versus grating lengths, we fit the threshold found numerically with two fitting functions, in orange and blue dashed lines, respectively. For the DDFB cavity, the trend is established by fitting $\alpha_{D,th}(N)$ with the function

$$\alpha_{D,th}^{fit}(N) = 1/(aN^5 + bN^2), \tag{4.6}$$

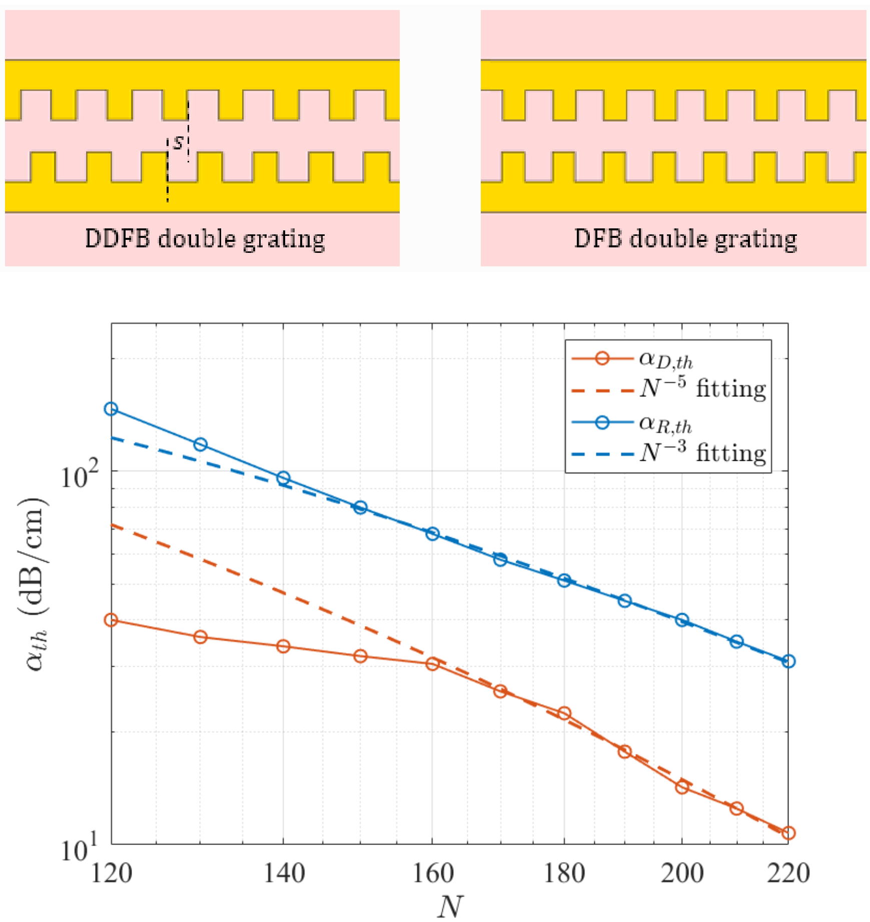

Figure 4.7: Comparison between the lasing thresholds of the DDFB (orange dots) and the DFB (blue dots) cavities of different lengths computed attheir respective DBE and RBE resonances. The dashed lines of the same color are the fitting functions that show the asymptotic N^{-5} scaling of the DBE lasing threshold $\alpha_{D,th}$ with DDFB waveguide length (in orange) and the N^{-3} scaling of the RBE lasing threshold $\alpha_{R,th}$ with DFB waveguide length (in blue).

and we calculate the fit over $N \in (160, 200)$. The fitting coefficients are calculated as $a = 1.29 \times 10^{-13}$ and $b = 6.78 \times 10^{-7}$. The N^{-5} term dominates for $N > 173$. We also verified that the difference $N^5 \times |\alpha^{fit}_{D,th} - \alpha_{D,th}|$ approaches a constant value for large N. This result shows that the lasing threshold follows the expected asymptotic scaling $\alpha_{D,th} \propto 1/(aN^5)$ for large N.

The trend for the lasing thresholds versus DFB cavity length is established in a similar manner, leading to the fitting function

$$\alpha^{fit}_{R,th}(N) = 1/(cN^3 + d), \tag{4.7}$$

with $c = 2.85 \times 10^{-9}$ and $d = 3 \times 10^{-3}$. Since the N^{-3} term dominates after $N = 101$, this result shows the asymptotic scaling threshold $\alpha_{R,th} \propto 1/(cN^3)$ for large N.

The main implications of these trends are twofold. Primarily, the mirrorless DDFB cavity displays significantly lower lasing thresholds than a mirrorless DFB cavity of the same length. For instance, the DDFB and a DFB cavities of $N = 60$ unit cells without mirrors exhibit a quality factor of $Q_D = 3451$ and $Q_R = 1378$, and a lasing threshold of $\alpha_{D,th} = 505$ and $\alpha_{R,th} = 1099$, respectively. The mirrorless DDFB cavity requires less than half the amount of gain (in dB/cm) to start oscillation of the preferred mode than a mirrorless DFB cavity of the same length for $N = 60$. By increasing N to only $N = 120$, $\alpha_{D,th} = 40$ dB/cm while $\alpha_{R,th} = 147$ dB/cm, and such a difference is increasing further for larger N. Because of the different asymptotic lasing threshold laws for the DDFB cavity, $\alpha_{D,th} \propto N^{-5}$, and the DFB cavity, $\alpha_{R,th} \propto N^{-3}$, the DDFB lasing principle is characterized by a different mechanism than that of a DFB laser. This suggests possibilities for device miniaturization and reduced power consumption. Indeed, when the trends are established for large-enough N, the ratio

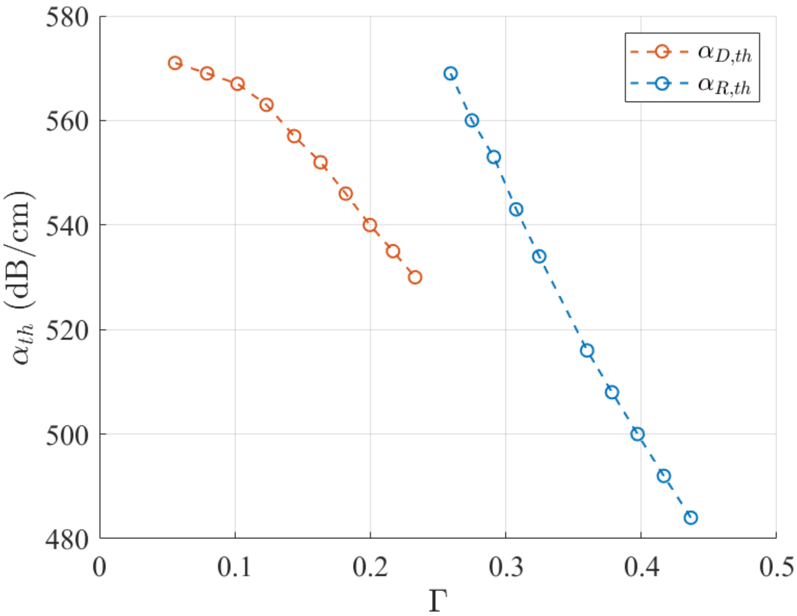

Figure 4.8: Comparison between the lasing thresholds of the DDFB (orange dots) and the DFB (blue dots) cavities with the same length ($N = 60$) as a function of the reflectivities Γ at their terminations. The DDFB cavity necessitates much lower reflectivities than the DFB cavity of the same length to display the same lasing threshold. Additionally, the threshold of the DDFB cavity is more resilient to variations in its terminations than the DFB cavity.

of the thresholds between the two cavities decreases asymptotically as

$$\frac{\alpha_{D,th}}{\alpha_{R,th}} \sim \frac{a}{c}\frac{1}{N^2}. \tag{4.8}$$

The anomalous $\alpha_{D,th} \propto N^{-5}$ threshold scaling law and the $Q_D \propto N^5$ asymptotic scaling of the quality factor shown in Figure 4.4 are bounded by the presence of defects and fabrication tolerances [133].

Figure 4.8 depicts the lasing thresholds of the DDFB (orange dots) and the DFB (blue dots) cavities with the same length $N = 60$ as a function of Γ as defined in Eq. (4.5). Primarily, it shows that the lasing threshold of the DDFB cavity is more resilient to changes in its terminations than that of the DFB cavity of the same length and quality factor. This trend is enhanced when the waveguides are long enough so that the asymptotic regimes for the scaling of the quality factor and lasing threshold at DBE resonances are established.

In summary, we have shown that mirrorless DDFB cavities display much larger quality factors and much lower lasing thresholds than comparable mirrorless DFB cavities of the same length. The quality factor and lasing thresholds of the DDFB cavity scale with waveguide length as the fifth power and inverse fifth power, respectively. In the DFB cavity, they scale as N^3 and N^{-3} instead. A related discussion in [68] regarding the local density of states distribution within the cavity for the DBE and RBE cases supports these claims. Additionally, we have shown that the DDFB cavity displays larger field amplitudes than the DFB cavity even when their loaded Q factors are the same. The lasing thresholds of both cavities can be tuned by adjusting the reflectivities at the cavities' ends. Importantly, the DDFB cavity has also been shown to be significantly more resilient to perturbations of the terminations of the lasing cavity, demonstrating its robustness to external effects.

Though not shown here, the resonance frequencies at which the thresholds are calculated are very close to the DBE resonances $f_{r,D}$ that, by virtue of (4.3), are asymptotically close to the DBE frequency f_D for large N. This means that by increasing the length of the grating, the oscillation frequency should be stable and close to f_D. Furthermore, the lasing frequency should be resilient to changes in load terminations. Indeed, this phenomenon has been already demonstrated in different but highly related studies at radio frequency accounting for nonlinear saturation effects, theoretically and experimentally, in Refs. [135, 136, 137] by varying the cavity loading.

4.5 Conclusion

We have advanced the concept of a degenerate distributed feedback (DDFB) lasing scheme for a cavity that operates in proximity to a DBE that is a special exceptional point of order four in a lossless and gainless multimode waveguide. The optical DDFB double grating is designed to have a degeneracy involving four propagating and evanescent optical modes, providing a degenerate distributed feedback. Consequently, for large N, a DDFB cavity exhibits a large quality factor, an ultralow lasing threshold, and a large stability to perturbations of its terminations. Indeed, we have shown that the DDFB cavity exhibits a quality factor that scales as the fifth power of the double grating length, compared to the third power scaling of a comparable DFB cavity, and that it supports larger intracavity field amplitudes for the same length and quality factor.

The four-mode degeneracy responsible for the DDFB lasing mechanism displays an enhanced interaction with the gain medium, which results in a low lasing threshold that scales as the inverse fifth power with waveguide length, clearly indicating a different lasing mechanism than in conventional lasers. Indeed, we have shown that the DBE resonance consistently has a lower lasing threshold than RBE resonances, indicating that lasing near the four-way degeneracy is preferred. These features of the DDFB lasing mechanism make the DDFB laser potentially very attractive for various applications where these features are important, including long-range spectral communications, sensing, spectroscopy, and more. The degenerate double grating structure proposed in this work is very versatile and can be implemented in various material platforms.

Chapter 5

DBE-SHG title

In this chapter, An anomalous flat band dispersion provided by a degenerate band edge (DBE) of optical modes in a double grating structure is used to enhance second harmonic generation (SHG) extracted vertically. The DBE is a fourth-order exceptional point of degeneracy (EPD) in a lossless and gainless waveguide, characterized by the coalescence of four eigenmodes that establish a frozen mode in a cavity. At a DBE resonance, the cavity's quality factor scales as $Q \propto N^5$, where N is the number of gratings' unit cells. In our numerical experiments, we observe the peak fundamental-field intensity in the edge-excited cavity scaling as $I_1 \propto N^{3.6}$. This leads to a highly efficient SHG process that is radiated vertically from the cavity without the need for phase matching, with a conversion efficiency scaling as $\eta \propto N^{8.27}$. The resulting theoretical conversion efficiency per-unit-length squared is comparable to the literature. These results establish DBE-based waveguides as promising platforms for miniaturized efficient nonlinear photonic devices.

5.1 Introduction

The development of efficient nonlinear photonic integrated circuits is essential for advancing technologies such as quantum information processing, optical signal processing, and ultrafast lasers [150]. A central example is second harmonic generation (SHG), where two photons at a fundamental frequency f_1 convert into one at $f_2 = 2f_1$ [151]. However, SHG efficiency remains low in typical devices due to weak nonlinear coefficients and poor mode overlap. A key figure of merit in nonlinear photonics is how the conversion efficiency scales with device length, since higher-order scaling can enable strong conversion in miniaturized platforms. Addressing this challenge requires new strategies to enhance field amplitudes in compact structures.

Researchers have explored photonic crystals and resonant cavities that localize optical fields [152, 98]. In Ref. [153], the N^8 scaling is demonstrated in an ideal periodic stack under non-phase-matching conditions. However, it relies on the assumption that both f_1 and f_2 lie exactly at the first resonances of their respective band edges, even though resonances approach each band edge differently depending on its curvature, making this assumption impractical in realistic designs.

Recently, BICs have drawn interest for their ability to trap light without radiation losses, leading to strong field confinement and enhanced nonlinear interactions [154, 155, 156, 157]. However, finite-size effects severely deteriorate the BIC mode in practical applications [158]. Alternative mechanisms that exploit dispersion-engineered properties offer new opportunities to enhance nonlinear effects.

In this work, we exploit the concept of exceptional points of degeneracy (EPDs) to enhance the nonlinear SHG efficiency. EPDs are unique points in a system where multiple eigenmodes coalesce (see for example Ref. [78, 80], or [3, 4] where Figotin and Vitebskiy refer to EPDs as stationary points). EPDs in photonic systems can exist in gain and loss balanced

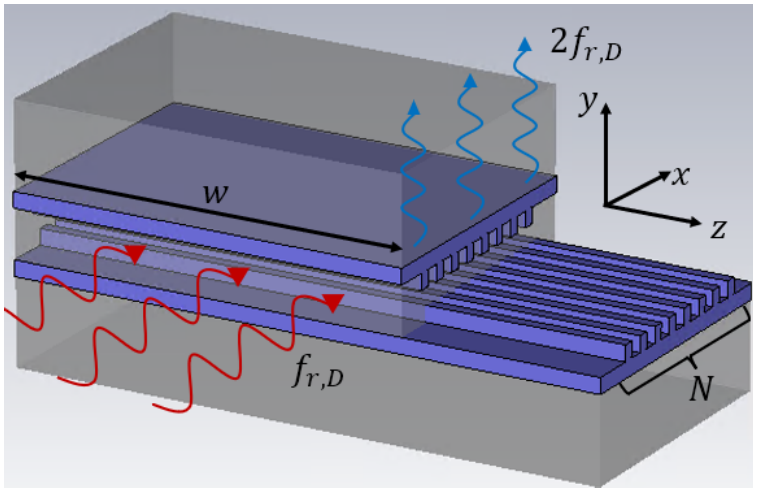

(a)

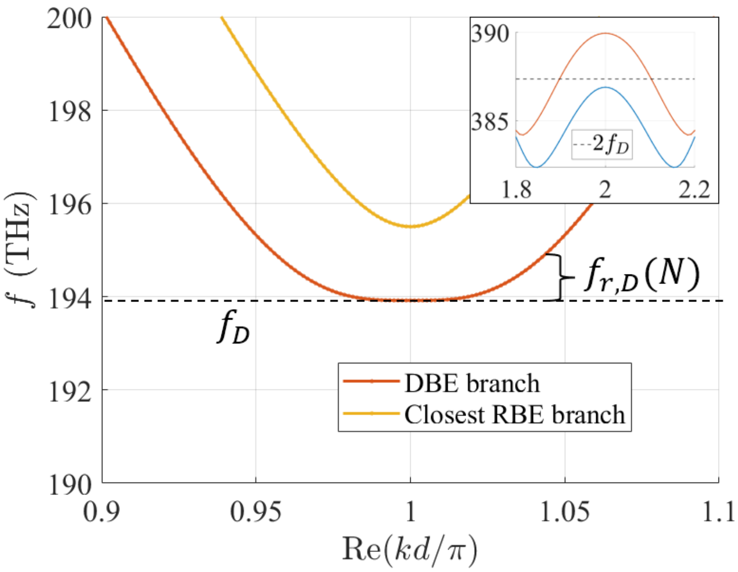

(b)

Figure 5.1: (a) Schematic of the three-dimensional double-grating waveguide composed of N unit cells along the x direction and width w in the transverse z direction. The upper section is partially removed for clarity. A pump wave at the DBE resonance frequency $f_{r,D}$ enters from the left (in the positive x direction) and generates a second harmonic at $2f_{r,D}$, which radiates vertically (in the y direction). (b) Modal dispersion diagram of the structure at the fundamental frequency, with the flat band at the Brillouin zone edge indicating the DBE at f_D (black dashed). The bracket shows the resonant frequency $f_{r,D}$ just above the DBE. The inset shows the dispersion diagram around $2f_D$ (black dashed line). The SHG at $2f_{r,D}$ would not excite a mode near $kd/\pi = 2$.

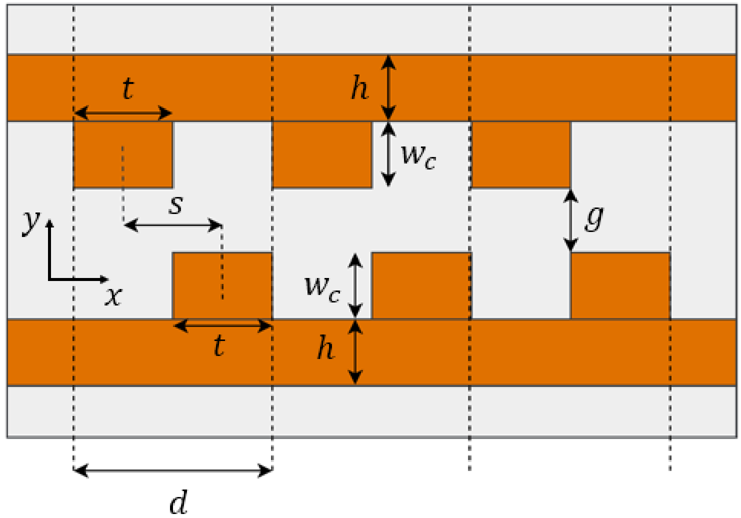

Figure 5.2: Double grating supporting guided longitudinal modes in the x direction, polarized along z (out-of-plane). The two oppositely-facing gratings are shifted by a distance s along x to break mirror symmetry, enabling the occurrence of the DBE that has a very flat band in the dispersion diagram provided in the second equation in Eq. (5.2).

systems, such as parity-time symmetric structures [79, 81, 18], or in purely passive systems through dispersion engineering [3, 5, 119]. The structured resonance mechanism discussed here is based on an EPD belonging to this latter class, i.e., a fourth-order EPD in a periodic waveguide without loss and gain [5], known as the degenerate band edge (DBE). At a regular band edge (RBE), a second-order EPD, two counter-propagating modes merge, leading to a standing wave with zero group velocity [99]. A DBE occurs when two counter-propagating and two evanescent modes merge, forming a frozen mode. DBEs at optical frequencies have been demonstrated in silicon photonic waveguides through dispersion reconstruction and by observing the scaling $Q_D \propto N^5$ in finite-length structures [113, 132]. Further experimental validations exist at microwave frequencies [134, 19].

When operated near the DBE frequency, a finite-length waveguide exhibits strongly enhanced field amplitudes away from the cavity edges and a group delay that scales with the fifth power of the waveguide length [4, 132, 5, 68, 134, 66]. In contrast, the group delay near a regular band edge (RBE) grows only with the cube of the length. The peak field intensities, defined as $I = |\mathbf{E}|^2$, scale asymptotically with the number of unit cells N as

$$\max(I_{\mathrm{RBE}}) \propto N^2,$$
$$\max(I_{\mathrm{DBE}}) \propto N^4, \tag{5.1}$$

which we aim to exploit to achieve a nonlinear conversion efficiency with a larger than N^8 asymptotic scaling, even without exciting Bloch modes at the second harmonic frequency. To illustrate this effect, we design a periodic waveguide composed of two coupled gratings that support a DBE at the fundamental frequency. The second harmonic signal is allowed to radiate vertically out of the structure, following the approach in [159]. This open configuration facilitates practical implementation. Figure 5.1a shows the three-dimensional design: a waveguide made of N periodic unit cells along the x-axis, with a finite width w in the transverse y-direction. For clarity, the upper half of the device is shown partially removed to reveal the full grating geometry. A pump at the DBE resonance frequency $f_{r,D}$ (the closest resonance to the DBE frequency) is launched from the left in the positive x direction. The resulting frozen-mode intensity enhancement leads to efficient SHG, with the generated signal at $2f_{r,D}$ radiating vertically (in the y direction) out of the waveguide. By leveraging the frozen mode effect, we achieve high field intensities at the fundamental frequency (I_1) deep inside the cavity that are shown to scale as $N^{3.6}$, yielding a nonlinear conversion efficiency that scales as $N^{8.27}$.

Figure 5.1b shows the real-branch modal dispersion diagram of the structure, where the DBE appears as a flat region near the Brillouin zone edge at $\mathrm{Re}(kd/\pi) = 1$. The black dashed line represents the DBE frequency f_D, whereas the bracket highlights the narrow spectral distance at which the frozen mode resonance $f_{r,D}$ in a finite-length grating occurs just above the DBE frequency. The inset displays the real part of the modal wavenumbers near the edge of the second Brillouin zone, confirming the absence of Bloch modes at twice the DBE frequency f_D (shown as a dashed black line) near $kd/\pi = 2$.

Our results highlight the potential of combining EPDs with nonlinear processes to overcome current limitations in integrated photonic devices. The proposed strategy provides a scalable and practical solution for enhancing nonlinear interactions, enabling an anomalous scaling of the frequency conversion efficiency in photonic integrated circuits.

The paper is organized as follows: The AlGaAs-based double-grating design that supports a DBE at the fundamental frequency is introduced in Section 5.2, and we analyze its performance in Section 5.3. Section 5.4 presents the features of the DBE-enhanced SHG process. The results are summarized in Section 5.5.

5.2 Design of the DBE-supporting double grating

The model structure chosen to show the enhancement of the field and of the nonlinear conversion efficiency consists of two paired standard gratings, shown in Figure 5.2 and initially presented in Ref. [160]. The structure is created by applying a mirror operation along the x, z plane and a longitudinal translation s on a grating. The coupling forms a system that supports four modes. To obtain a DBE in this structure, its four modes must coalesce with the same frequency, Bloch wavenumber, and polarization. The translation s disrupts the mirror symmetry of the device, a necessary condition to obtain coalescence between the four modes supported by this structure [160]. This waveguide can be designed using any pair of materials (silicon-on-insulator (SOI) technology, SiN, InP, $LiNbO_3$, GaAs, etc.), yet here we choose to design it with a core of $Al_{0.2}Ga_{0.8}As$ so it has a gap wavelength around 750 nm (or 400 THz) [161], the target second harmonic wavelength, with nonlinear coefficient $d_{14} = 125$ pm/V. Around the fundamental frequency $f_1 \approx 193.68$ THz, we have a core refractive index of $n_{c,1} = 3.2837$, and $n_{c,2} = 3.5607$ at the second harmonic frequency $f_2 \approx 387.36$ THz [162].

The cladding is AlGaO with a refractive index of $n_{clad} = 1.6$ [163]. We account for the refractive index difference between f_1 and f_2 in the core, but neglect dispersion within the narrow frequency ranges of interest around each frequency. The cladding index is assumed constant over the entire range.

The goal here is to design the double grating so these four modes coalesce into the DBE-associated frozen mode. This occurs at the DBE frequency $f_D \approx 193.679$ THz and at the edge of the first Brillouin Zone, i.e., $k_D d = \pi$ (where d is the unit cell period), leading to a strong second harmonic nonlinear conversion efficiency η. This occurs because the DBE displays enhanced intensities in the cavity compared to the RBE (as shown in Eq. (5.1)). Near these exceptional points, their dispersions are approximated as [113, 68, 134, 5, 133, 66]

$$\begin{aligned}(f - f_R) &\approx \tfrac{h_R}{2\pi}(k - k_R)^2, \\ (f - f_D) &\approx \tfrac{h_D}{2\pi}(k - k_D)^4,\end{aligned} \tag{5.2}$$

where $f_{D/R}$ and $k_{D/R}$ are the EPD frequencies and the Bloch wavenumbers for the DBE and RBE cases, respectively. The parameters h_R and h_D describe the local flatness of the band edges and are sometimes referred to as ”flatness parameters”. The DBE displays a much flatter dispersion than the RBE in Figure 5.1b, and its flatness is associated with the propagating component of the four-way degenerate mode [48]. At the DBE, $d^n\omega/dk^n = 0$ for $n = 1, 2, 3$, and $d^4\omega/d_k^4 = 24h_D$. For the case presented in this paper, where the band gap is below f_D, h_D¿0. Otherwise, $h_D < 0$. The difference between the DBE resonance frequency $f_{r,D}$ (the closest resonance to the DBE) and the DBE frequency f_D determines the magnitude of the enhanced field amplitudes in the cavity, the linewidth of the resonance, its group velocity, and quality factor Q_D.

The double-grating design that supports a DBE at frequency $f_D = 193.679$ THz is obtained via a combination of manual and numerical parameter optimization. The key design metric is the minimization of the second derivative of the Bloch modes at the edge of the Brillouin Zone $k = \pi/d$, which is the first derivative of the group velocity, $v_g = d\omega/dk$. Specifically, the DBE condition is achieved when $|d^2\omega/dk^2|_{k=\pi/d} \to 0$ which ensures that all four Bloch modes supported by the double grating become degenerate. In contrast, minimizing only the group velocity magnitude $|v_g| \to 0$ at $k = \pi/d$ may yield an RBE instead. The value of the geometric parameters of the double grating was also optimized so that the frequency difference between the DBE and the nearest RBE is large enough to prevent issues with the resonances of the finite-length structure.

The double grating shown in Figure 5.2 is modeled in COMSOL Multiphysics, a full-wave electromagnetic solver based on finite element methods. Our objective is to obtain longitudinal modes that propagate in the x direction and are polarized in the z direction (using the coordinate system as shown in Fig. 5.1a and 5.2). In a practical implementation, the width w of the coupled gratings is much larger than the wavelength, i.e., $w \gg \lambda$. To reduce computational cost, we perform 2D simulations under the approximation $w \ll \lambda$ in the x-direction, which retains the essential modal physics of the coupled gratings. Perfectly matched layers (PMLs) are applied in the vertical y-direction, and the cladding thickness is chosen to ensure field decay before reaching the boundaries. This setup minimizes reflections and ensures proper absorption of outgoing radiation.

The modal dispersion diagram for the infinitely long double grating is computed by simulating a single unit cell of the waveguide using the eigenfrequency study in COMSOL Multiphysics, with periodic boundary conditions. Figure 5.1b shows the resulting purely-real branch of the dispersion diagram. The optimization algorithm uses gradient descent methods to minimize the magnitude of the group velocity dispersion at $k = \pi/d$ and achieve the formation of the DBE by optimizing six geometric parameters: period d, height h, gap g, core width w_c, thickness t, and shift s. The resulting waveguide's parameters are (in nm):

$d = 300$, $h = 150$, $g = 120$, $w_c = 184$, $t = 200$, and $s = 100$. The solid-orange curve denotes the modes that coalesce at the DBE frequency $f_D = 193.679$ THz, while the solid-blue curve at lower frequencies denotes the modes that coalesce forming a regular band edge (RBE) at 195.5 THz that also occurs in the same structure.

5.3 Linear response

Next, we consider a finite double-grating cavity made of N unit cells terminated by regular transmission lines with height h (without mirrors) as illustrated on the sides of Fig 5.2. The properties of the DBE-associated frozen mode are accessed through the closest Fabry-Pérot resonance to the DBE frequency, termed the "DBE resonance" $f_{r,D}$, as in [113, 5, 133, 66]. Similarly, the closest resonance to an RBE is referred to as the "RBE resonance" $f_{r,R}$. These resonances converge to the corresponding EPD frequencies with increasing N, following the asymptotic expressions

$$\begin{aligned} f_{r,D} &\sim f_D + \tfrac{h_D}{2\pi}\left(\tfrac{\pi-\varphi}{Nd}\right)^4, \\ f_{r,R} &\sim f_R + \tfrac{h_R}{2\pi}\left(\tfrac{\pi}{Nd}\right)^2, \end{aligned} \tag{5.3}$$

The scaling of the DBE resonance approaches the DBE frequency with the $1/N^4$ asymptotic difference as shown in [113, 68, 134, 5, 133, 66, 19], while the RBE resonances approach the RBE frequency with the $1/N^2$ asymptotic difference [164]. The angle φ accounts for the presence of the evanescent waves in a DBE resonant cavity [99, 113]. (Note that also the term φ should have been included in [134, 5, 66, 19].) Figure 5.3a confirms this behavior: the DBE resonances (black dots) approach $f_D = 193.679$ THz following the N^{-4} scaling trend of Eq. (5.3). For $N > 200$, the cavity exhibits the asymptotic frozen mode behavior. The small value of h_D, normalized by $1/d^4$ with $d = 300$ nm, validates the extreme flatness of the DBE.

The resulting frozen mode exhibits greater field intensity enhancement and group delay compared to the slow-wave resonance associated with the RBE [4]. As a result, waveguides operating near the DBE typically outperform those near an RBE. For example, the quality factor for an RBE increases asymptotically with waveguide length as $Q_R \propto N^3$, whereas for a DBE it scales as $Q_D \propto N^5$ [4, 132, 68, 5, 133]. Importantly for this study, the maximum field intensity enhancement provided by the DBE-associated frozen mode scales as $\max(I) \propto N^4$, leading to an extraordinary enhancement of the nonlinear polarization excited at the second harmonic frequency.

The linear properties of the finite-length double grating around the DBE frequency are evaluated using the FEM solver in COMSOL Multiphysics. The cavity is excited from the left using the even mode of the input waveguide, launched at a distance $L = 1.8$ μm from the start of the grating. The excitation is a two-dimensional mode with unit incident power (1 W/m). Perfectly matched layers (PMLs) are applied in both the vertical (y) and horizontal (x) directions, with sufficient cladding thickness to absorb outgoing waves before they reach the simulation boundaries.

Fig. 5.3b displays the normalized fundamental-field intensity envelope I_1 in the x direction across the cavity of length Nd for different values of N. The field intensities are evaluated at the center of the top waveguide core and at their respective DBE resonances. The collapse of all normalized curves into a single profile confirms that the normalized intensity distribution inside the cavity remains nearly unchanged with N. Figure 5.3c displays the field amplitudes at the center of the cavity (as orange dots) and at one third of the waveguide length from the center (as blue dots). The solid lines of the same color are the fitting functions $I_{1,fit}(N) = aN^b$, with $a = 4.5 \times 10^{12}$, $b = 3.6$ at the center of the cavity, and $a = 2.5 \times 10^{12}$, $b = 3.36$ at a third of the cavity length ($x = Nd/3$, fit for $N \in [240, 300]$). Both curves are normalized by

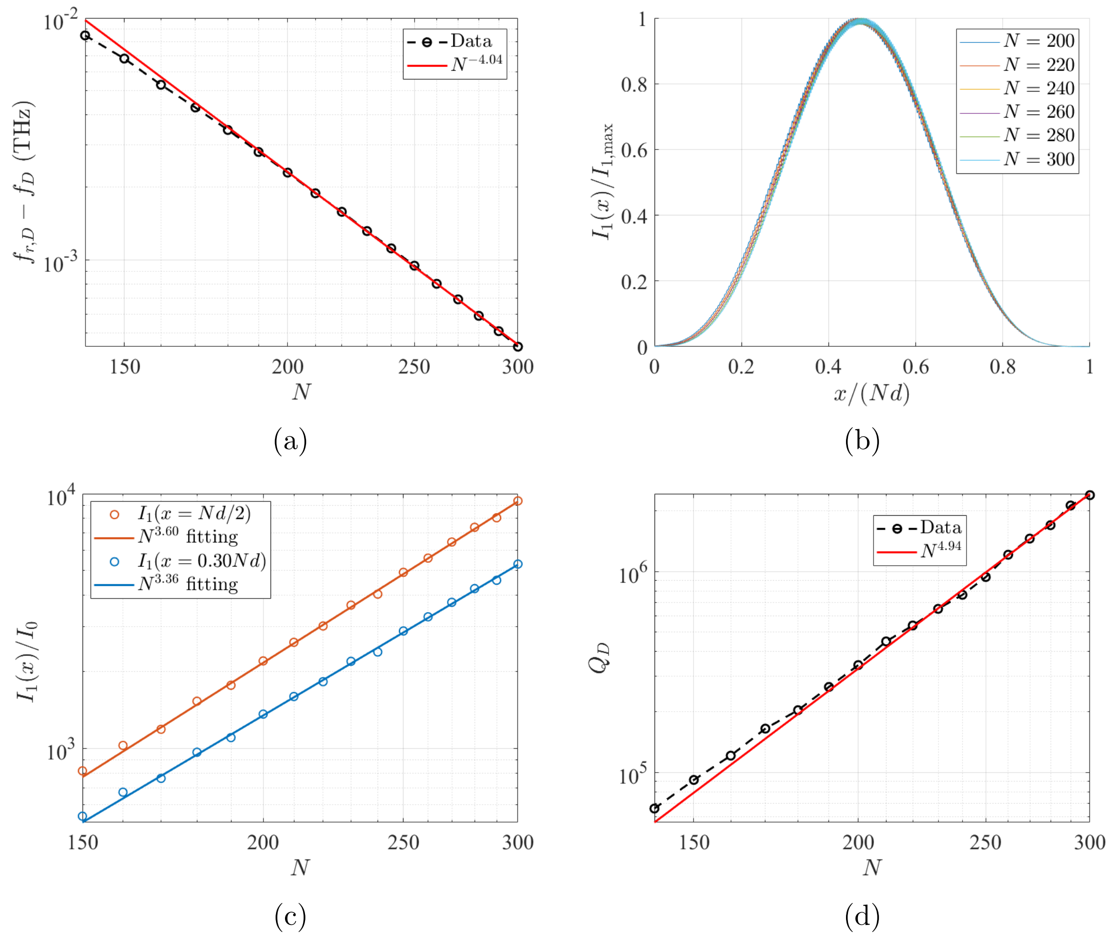

Figure 5.3: (a) Difference between the DBE resonance $f_{r,D}$ and the ideal DBE frequency f_D as a function of the number of unit cells. Black dots show the simulation data; the red line is the fit from Eq. (5.3). (b) Normalized field intensity profiles $I_1(x)/I_{1,\max}$ along the longitudinal position $x/(Nd)$ for various waveguide lengths N, evaluated at the center of the top waveguide core and at their respective DBE resonances. All normalized profiles collapse onto a single curve, indicating that the spatial distribution of the field is preserved as N increases. This confirms that increasing the number of unit cells enhances the field amplitude without altering the shape of the intensity envelope. The intensity peak approaches $x = Nd/2$ for increasing N. (c) Field intensity values $I_1(N)$ normalized by the incident power $I_0 = 3.86 \times 10^8$ $(\mathrm{V/m})^2$, evaluated at the cavity center $x = Nd/2$ (orange) and at one-third of the length from the center $x = Nd/3$ (blue) as a function of N. Solid lines represent power-law fittings of the form $I_{fit}(N) = aN^b$, yielding exponents of $b = 3.6$ and $b = 3.35$, respectively. While these powers are below the expected N^4 asymptotic scaling from Eq. (5.1), these results confirm enhanced intensity growth relative to the N^2 trend typical of regular band edge resonances. (d) Loaded quality factors of the DBE-supporting double grating (represented by black dots and evaluated at its DBE resonance) varying grating length. The dashed lines of the same color are the fitting functions that show the asymptotic N^5 scaling of the DBE quality factor Q_D with waveguide length.

the incident intensity $I_0 = 3.86 \times 10^8$ (V/m)^2. While these exponents fall short of the ideal N^4 scaling predicted by Eq.(5.1), they clearly exceed the N^2 growth near an RBE, underscoring the superior confinement provided by the DBE. The deviation from N^4 is attributed to the discretized and practical nature of the structure. Field enhancement also varies with the waveguide's geometry, platform, and length. Different DBE-supporting designs such as that in Ref. [133] exhibit different enhancement factors.

Figure 5.3d shows the quality factor of the cavity at the DBE resonance as a function of the waveguide length (given by N). The quality factor is computed for a loaded double grating structure extended continuously on both sides (without mirrors or corrugations) as regular transmission lines with height h as illustrated on the sides of Fig 5.2. The quality factor is extracted using the spectral definition $Q = f_r/BW$, where BW is the 3 dB bandwidth of the transmission peak at resonance frequency f_r. This method aligns well with other techniques, as shown in [165]. The quality factors are depicted as black dots, while the solid red line represents the fitting function $Q_{fit}(N) = aN^b$, with $a = 2.43 \times 10^6$ and $b = 4.94$ (for $N \in [200, 300]$). This confirms the expected N^5 scaling of the DBE-associated resonance, consistent with prior work [4, 132, 68, 5, 133, 134]. The steep N^5 scaling arises from a strong impedance mismatch at the terminations, driven by destructive interference between nearly degenerate propagating and evanescent modes at the DBE resonance [4, 146]. This interference necessitates large modal amplitudes to satisfy boundary conditions, resulting in enhanced field amplitudes deep inside the cavity. In contrast, in RBE-based structures the evanescent components are negligible and $Q \propto N^3$. Larger Q also implies increased robustness of the DBE mode against termination imperfections and improved SHG performance away from the cavity edges.

In summary, the DBE-supporting double-grating displays a strong scaling of the DBE resonance frequencies $f_{r,D}$, which approach f_D with an N-dependent difference that decreases as N^{-4}, as shown in (5.3). Additionally, we have shown that the double grating displays a maximum field intensity I_1 at the center of the cavity that scales as $N^{3.6}$ and a loaded quality factor that scales as N^5 with waveguide length (as opposed to $\max(I) \propto N^2$ and $Q \propto N^3$ when operating near an RBE).

5.4 Frozen mode second harmonic generation enhancement

The goal of this section is to demonstrate the extraordinary enhancement of the SHG enabled by the DBE and its scaling laws with grating length. We assume a second-order nonlinear polarization density induced at the second harmonic frequency given by

$$P_z(2f) = -\frac{\varepsilon_0 d_{14}}{\sqrt{3}} E_z^2(f), \tag{5.4}$$

where $d_{14} = 125$ pm/V is the nonlinear coefficient of AlGaAs [166] and E_z is the electric field at the fundamental frequency f_1. The longitudinal modes propagate along the x-direction and are polarized along z. The crystal is cut along the [111] direction so that the polarization of the resulting second harmonic field also lies along z. This choice ensures that any guided Bloch modes at f_2, if present, would be efficiently excited. Below, we show that we have no evidence of guided Bloch mode excitation, confirming non-resonant SHG excitation. Additional details on the polarization response due to the crystal cut orientation are provided in Appendix A.

The energy and momentum conservation conditions [151] in a periodic waveguide become

$$
\begin{aligned}
f_2 &= f_1^+ + f_1^-, \\
k_2 &= k_1^+ + k_1^-, \;\; 2k_1^+, \;\; 2k_1^-
\end{aligned}
\tag{5.5}
$$

where the $\pm$ superscripts refer to the two counter-propagating photons at the fundamental frequency. Since SHG occurs at the resonance of the fundamental frequency, $f_1^+ = f_1^- = f_{r,D}$, and their corresponding wavenumbers are $k_1^+ = \pi/d + \chi$ and $k_1^- = \pi/d - \chi$, where $\chi = (\pi - \varphi)/(Nd)$, as derived from Eqs. (5.2) and (5.3). This implies $k_2 = 2\pi/d$ for all N, in addition to $k_2 = 2\pi/d + 2\chi$ and $k_2 = 2\pi/d - 2\chi$. For large N, these three wavenumbers are all close to $2\pi/d$. Importantly, the DBE-associated frozen mode at $f_{r,D}$ is composed of four waves, rather than the two waves at a resonance near a regular band edge. In fact, it is the coalescence of those waves into the frozen mode which provides the enhanced field amplitude away from the cavity's edges [4, 66].

We now derive approximate expressions for the pump field distribution and the resulting second-harmonic source in terms of Bloch modes. The pump electric field in the finite periodic structure can be expressed as a superposition of the four Bloch modes of the corresponding infinite structure: $E_z(f) = \sum_0^3 A_m e^{ik_1^{(m)}x}$, where the wavenumbers near the DBE take the form $k_1^{(m)} = \pi/d + \chi e^{im\pi/2}$. Here, $k_1^{(0)} = k_1^+$ and $k_1^{(2)} = k_1^-$ are associated with two propagating modes, whereas $k_1^{(1)}$ and $k_1^{(3)}$ are associated with two evanescent modes. Moreover, $\chi = (\pi - \varphi)/(Nd)$ is the distance of the four eigenmodes from the edge of the Brillouin zone, and φ accounts for the phase gathered by the propagating modes when reflected at the two cavity interfaces [113]. The amplitudes $A_m = A_m(x, y)$ are periodic in x with period d. To obtain a simplified representation near the DBE, we approximate the A_m as constants, focusing on one of the Floquet harmonics. At the DBE resonance of the finite structure, the total field is much smaller at the edges of the cavity than in its center, and we know that this phenomenon is due to the strong excitation of evanescent waves at the two cavity interfaces [99]. In other words, the DBE resonance requires that the intensity of the propagating portion of the field be approximately equal to the intensity of the evanescent portion of the field, with the two almost canceling each other at the two interfaces $x = 0$ and $x = Nd$. In addition, the two counter-propagating components should have approximately equal amplitudes and interfere constructively at the center of the cavity. With these prescriptions in mind, we obtain $A_1 \approx -[1 + e^{i(\pi-\varphi)}]/[1 + e^{-(\pi-\varphi)}]A_0$, $A_2 \approx A_0 e^{i(\pi-\varphi)}$, and $A_3 \approx A_1 e^{-(\pi-\varphi)}$. It follows that the pump electric field simplifies to an expression that depends on φ and A_0,

$$\begin{aligned} E_z(f_1) = 2A_0 e^{i\pi x/d} e^{i(\pi-\varphi)/2} \Bigg[& \sin(\chi x + \varphi/2) + \\ & - \frac{\sin(\varphi/2)}{\cosh\left(\frac{\pi-\varphi}{2}\right)} \cosh\left(\chi x - \frac{\pi-\varphi}{2}\right)\Bigg], \end{aligned} \tag{5.6}$$

highlighting the presence of a standing wave formed by the counter-propagating Bloch modes, with a maximum intensity at $x = Nd/2$, as well as the presence of an amplitude term originated by the two evanescent Bloch modes, i.e., the cosh term. We stress that a DBE resonance is only possible if $\varphi \neq 0$. In fact, for $\varphi = 0$, the amplitudes of the evanescent portion of the field would be equal to zero and the field in Eq. 5.6 would reduce to the typical shape of an RBE cavity. Instead, setting the single fitting parameter to $\varphi = -0.46\pi$ yields good agreement of the Bloch model with the numerical simulation, as illustrated in Fig. 5.4. The Bloch decomposition allows the isolation of the contribution of the propagative and the evanescent components of the field. The intensity of these components is reported in Fig. 5.4, along with the total field intensity. The evanescent and propagative portions of the field cancel out at the edges of the cavity, while at the center of the cavity all four Bloch modes add in phase. It is important to notice that the evanescent modes add a non-negligible contribution to the overall pump intensity peak at the cavity center. Indeed, the pump intensity at $x = Nd/2$ can be written as

$$I_{1,\max} = 4|A_0|^2 \left[1 - \frac{\sin(\varphi/2)}{\cosh(\frac{\pi-\varphi}{2})}\right]^2, \tag{5.7}$$

With $\varphi = -0.46\pi$, the parenthesis in Eq. (5.7) evaluates to ≈ 1.28, which means that the evanescent portion of the field is providing almost a 30% increase of pump intensity, which further boosts the nonlinear processes. This enhancement is a hallmark of a DBE cavity. In an RBE cavity, where $\varphi = 0$, only the two propagating Bloch modes interfere constructively at the cavity center, producing the conventional $\sin^2$ intensity profile.

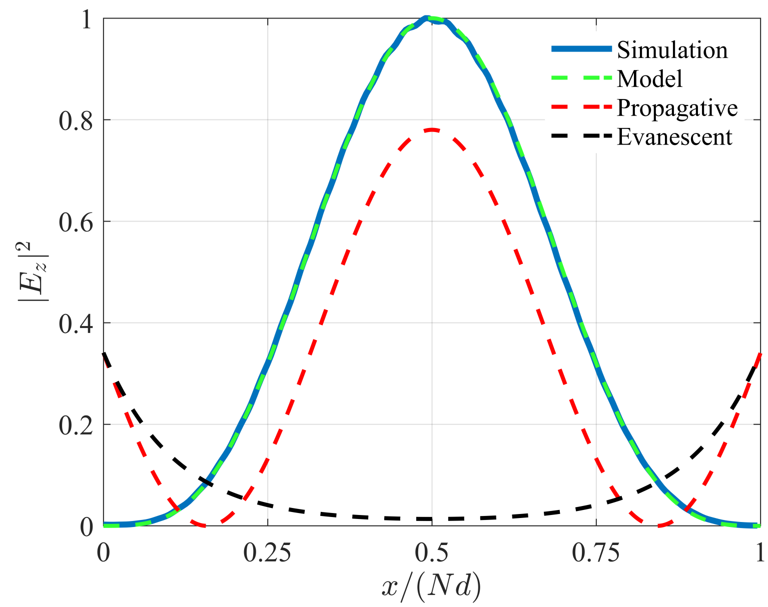

Figure 5.4: Fundamental-field intensity in the cavity at the DBE resonance, for $N = 200$. The Bloch model (green dashed curve, retrieved from Eq. (5.6)), shows excellent agreement with the numerical simulation (blue curve). The red-dashed line is the intensity of the propagating portion of the field, $|A_0 e^{ik^{(0)}x} + A_2 e^{ik^{(2)}x}|^2$, while the dark-dashed line is the intensity of the evanescent portion of the field, $|A_1 e^{ik^{(1)}x} + A_3 e^{ik^{(3)}x}|^2$. All the quantities are normalized with respect to the value of the maximum peak intensity in the center of the cavity.

The z-component of the nonlinear polarization density induced at the second-harmonic frequency,

$$
\begin{aligned}
P_z(2f_1) \propto 4A_0^2\, e^{i\frac{2\pi}{d}x} e^{i(\pi-\varphi)} \Big[& \sin^2\left(\chi x + \varphi/2\right) + \\
& + \frac{\sin^2\left(\varphi/2\right)}{\cosh^2\left(\frac{\pi-\varphi}{2}\right)} \cosh^2\left(\chi x - \frac{\pi-\varphi}{2}\right) + \\
& - \frac{2\sin\left(\varphi/2\right)}{\cosh\left(\frac{\pi-\varphi}{2}\right)} \cosh\left(\chi x - \frac{\pi-\varphi}{2}\right) \sin\left(\chi x + \phi/2\right) \Big],
\end{aligned} \tag{5.8}
$$

reveals: (i) the ability of the structure to emit second-harmonic light in the vertical direction, due to the fact that the source shows the same phase in each period of the structure; (ii) the crucial role of the evanescent modes supported by the DBE cavity in shaping and increasing the overall intensity of the nonlinear source.

As shown in Figure 5.1b, the DBE has a bandgap below f_D, so the fundamental frequency satisfies $f_1 \equiv f_{r,D} > f_D$, with $f_1 \to f_D$ only for $N \to \infty$. The dispersion at the second harmonic, shown in the inset in Figure 5.1b, confirms that no Bloch modes exist near $kd = 2\pi$ at $f_2 \approx 2f_D$. Thus, the conditions in Eq. (5.5) are not met, and the nonlinear polarization does not couple to propagating modes at f_2. The observed SHG is therefore entirely attributed to the non-phase matched nonlinear effect induced by the frozen mode at f_1.

Operating the pump at the DBE resonance $f_1 = f_{r,D}$ implies a second harmonic frequency of $f_2 = 2f_{r,D}$, which asymptotically follows

$$
f_2 \sim 2f_D + \frac{h_D}{\pi}\left(\frac{\pi-\varphi}{Nd}\right)^4, \tag{5.9}
$$

as N increases. Since no guided Bloch modes exist at $f_2 = 2f_{r,D}$, the generated second harmonic radiates vertically through the top and bottom cladding. Due to the strong impedance mismatch at the cavity terminations at the DBE resonances (discussed in Section 5.3), the second harmonic field is concentrated near the center of the cavity and suppressed at the terminations, following the I_1^2 pattern in Fig. 5.3b.

Figure 5.5a depicts the normalized field intensity $I = |\mathbf{E}|^2$ along the cavity (evaluated at the middle of the top waveguide core) for a structure with $N = 330$. The intensity profile I_1 at the fundamental frequency $f_1 = f_{r,D}$ (the DBE resonance) is shown as a solid blue curve, while its squared value I_1^2 is plotted as a solid red curve. The dashed yellow curve represents the normalized intensity I_2 at the second harmonic frequency $f_2 = 2f_{r,D}$. The near-perfect agreement between I_1^2 and I_2 in Figure 5.5a and the results shown in Figure 5.1b are evidence that the second harmonic field arises mostly from the nonlinear polarization density driven by the DBE-enhanced fundamental field. Although periodic structures can, in general, enable the excitation of Bloch modes via field gradient, our results show no significant evidence of such excitation in this case.

Here, we define the nonlinear conversion efficiency η [167, 168] as

$$\eta = \frac{P_2}{P_1^2}, \tag{5.10}$$

where P_1 is the incident power from the left at the fundamental frequency (the DBE resonance) and P_2 is the output power at the second harmonic frequency. Since we perform 2D simulations for a structure invariant along z, here, we assume a nominal width of $w = 1$ µm, as shown in Figure 5.1a and the incident power P_1 over that width is expressed in units of W. As discussed next, P_2 is the power extracted vertically, and it has also a unit of W; hence the efficiency has units of W^{-1}.

The power radiated vertically at the second harmonic is calculated as

$$P_2 = \int_0^{Nd} S_y(x)\ dx, \tag{5.11}$$

where $S_y(x)$ denotes the vertical component of the time-averaged Poynting vector $\mathbf{S} = \Re(\mathbf{E} \cdot \mathbf{H}^*)/2$. $\Re$ is the real part operator, and x is the longitudinal direction as shown in Fig. 5.2. This integration is done at a distance equal to one period d from the end of the top waveguide core to allow the field of higher-order harmonics to decay. The P_1^2 normalization ensures η is independent of the incident power in the undepleted pump approximation [150].

The nonlinear properties of the finite-length double gratings at the DBE resonances are obtained using the FEM frequency domain solver in COMSOL Multiphysics. The structure is excited at the N-dependent DBE resonance frequency $f_1 \equiv f_{r,D}$ from the left in the positive x direction, as in the linear studies in Section 5.3, inducing the nonlinear polarization described in Eq. (5.4). The same boundary conditions used in the linear simulations are applied.

The main result of this paper is the asymptotic scaling of the nonlinear conversion efficiency η with waveguide length, enabled by the exceptional light-matter interaction between the DBE-associated frozen mode and the nonlinear medium in the waveguide core. Figure 5.5b displays η as a function of the number of unit cells N, depicted as black dots. The inset shows the field at the fundamental frequency excited from the left whereas that at the second harmonic at $f_2 \equiv 2f_{r,D}$ is extracted vertically from the structure. The solid red line represents the fitting function $\eta = aN^b$. The parameters have been evaluated as $a = 1.12$ and $b = 8.27$, with a fitting done in the interval $N \in [200, 300]$. This exceptional scaling of the nonlinear conversion efficiency is striking compared to what has been published in the literature so far. It is higher than the scaling $\eta \propto N^8$ reported in [153], found in a doubly-resonant structure. The technique reported in [153] was based on exciting an RBE resonance at f_1 and having f_2 coincident with an RBE resonance at f_2, and despite representing a record high scaling of the efficiency with the number of unit cell of the photonic crystal there employed, it requires a precise condition of double resonance at the two RBEs that is not easy to realize. Indeed, the study in [153] was based on a multilayered photonic crystal where the double resonance condition was found assuming zero dispersion of the materials' parameters.

In our case instead, the scaling is obtained by only choosing f_1 corresponding to the DBE resonance frequency, without requiring the excitation of any Bloch modes at the second harmonic. The DBE-enhanced strong power scaling arises from the fact that the nonlinear conversion efficiency is proportional to the square power of the field intensity I_1, whose maximum has been shown to scale with waveguide length as $\max(I) \propto N^{3.6}$ at the DBE resonances. Since the integral of the Poynting vector in Eq. (5.11) adds an additional N contribution to the leaked power, we expect $\eta_D \propto N^{8.2}$, following the law

$$P_2 \propto N \max(I_2) \propto N \max(I_1^2) \tag{5.12}$$

Our numerical findings return a leaked second harmonic power that leads to an efficiency that scales as $\eta_D \propto N^{8.27}$. These minor discrepancies can be attributed to numerical discretization effects and the difference in the evaluation region: η is computed one period above the waveguide well into the cladding, whereas the peak field intensity is taken at the center of the top waveguide core.

The main implications of this trend are that (i) relying on the DBE for nonlinear interactions (rather than on an RBE) allows for a remarkable miniaturization of photonic integrated nonlinear sources and devices beyond previous estimates, even without phase-matching; (ii) despite the DBE being a condition that requires precise fabrication, our proposed technique only requires the tuning of f_1 with the resonance frequency of the DBE cavity and no phase

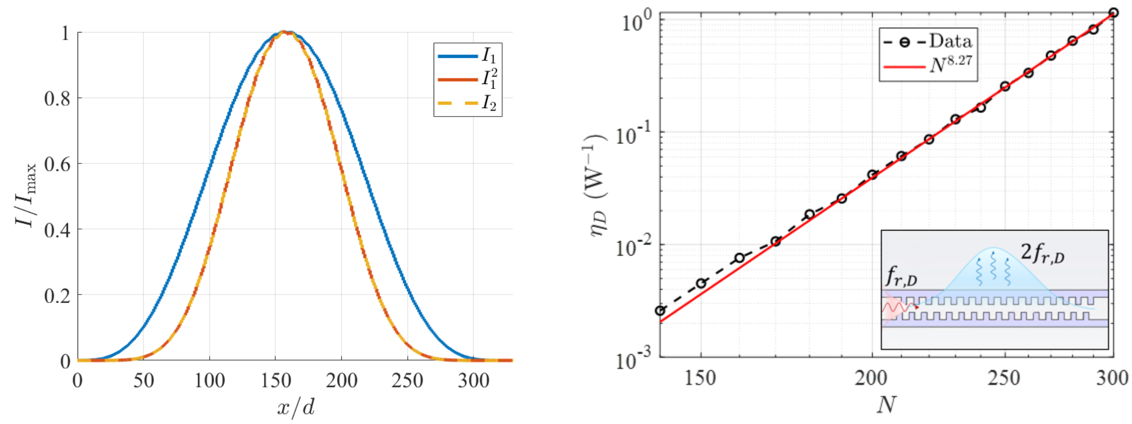

(a) (b)

Figure 5.5: (a) Normalized intensity profiles along the longitudinal x axis of a double grating with $N = 330$ unit cells at the center of the top waveguide core. The solid blue line shows the intensity I_1 at the fundamental frequency $f_1 = f_{r,D}$, while the solid red line represents its squared value, I_1^2. The dashed yellow line denotes the normalized intensity I_2 at the second harmonic ($f_2 = 2f_{r,D}$). The near-perfect overlap between I_1^2 and I_2 confirms that the second harmonic field distribution follows the nonlinear polarization generated by the DBE-enhanced field, and that no guided Bloch modes are substantially excited at f_2. (b) Conversion efficiency of the double grating (black dots) cavities of different lengths computed at their respective DBE resonances. The solid red line depicts the fitting function that shows the asymptotic $N^{8.32}$ scaling of the nonlinear conversion efficiency η_D with waveguide length. The inset denotes that the field at the fundamental frequency $f_1 = f_{r,D}$ is excited from the left and the field at the second harmonic frequency leaks vertically out of the structure.

matching is required at f_2; (iii) in the present double-grating configuration, the generated second harmonic field primarily radiates vertically through the cladding, while the fundamental mode is side-coupled, which may simplify device integration. Note that while the second harmonic has been shown not to couple to guided Bloch modes, edge-induced effects could still excite weakly guided or radiative components at f_2, though this is not observed due to the high degree of matching between the shape of I_2 with that of I_1^2.

For the DBE-supporting double grating with $N = 300$ unit cells (corresponding to a total length of $L = 0.9$ μm), we obtain a second harmonic generation efficiency of $\eta = 1.15$ (W)$^{-1}$. Put differently, the structure converts a 4% of the pump power into vertically emitted second-harmonic light while operating at an input, peak-power density of 10 MW/cm^2, a relatively low intensity level in the realm of nonlinear optics. Note that we have assumed a width

Ref.	Material	Device	Length [mm]	P_1 [W]	P_2 [W]	$\eta = P_2/(P_1^2)$ [W^{-1}]	$\eta_{norm} = P_2/(P_1^2 L^2)$ [$W^{-1}cm^{-2}$]
[169]	AlGaAs	WG	5	1.9×10^{-3}	0.85×10^{-6}	0.2	0.83
[170]	AlGaAs	Suspended wire	1000	8×10^{-4}	3.9×10^{-9}	0.006	6.1×10^{-7}
[170]	AlGaAs	Suspended rib	200	4.0×10^{-4}	2.7×10^{-11}	1.68×10^{-4}	4.22×10^{-7}
[171]	GaAs	Waveguide	2.9	5×10^{-6}	1×10^{-9}	40	475.62
[172]	AlGaAs	Waveguide	0.5	68×10^{-6}	0.12×10^{-9}	0.026	10.38
[173]	AlGaAs	Waveguide	2.17	3.3×10^{-3}	60×10^{-6}	5.5	117
[167]	AlGaAs	Nano wire	12.6	155×10^{-6}	50×10^{-12}	0.002	0.001
[174]	AlGaAs	Waveguide	0.5	0.3×10^{-3}	2.25×10^{-6}	25	10×10^3
This work	AlGaAs	DBE Double grating	0.09	1×10^{-6}	1.15×10^{-12}	1.15	14×10^3

Table 5.1: Comparison of SHG efficiency in various experimental AlGaAs and GaAs waveguides.
* To compare the 2D double grating efficiencies, we have assumed a width $w = 1$ µm. (N=300)*

$w = 1$ µm. A comparison with previously reported experimental AlGaAs devices is provided in Table 5.1. While the resulting efficiency is moderate compared to the highest values reported in the 7th column in Table 5.1, this comparison does not consider differences in device length. Here we normalize the SHG efficiency by L^2 to remove the dependency on the interaction length, as in [173, 167, 170]. Then, our structure yields $\eta_{\text{norm}} = 14 \times 10^3$ $W^{-1}cm^{-2}$, which surpasses all the values in Table 5.1. This result highlights the potential for extraordinary miniaturization of nonlinear devices operating near a DBE. Additionally, these results are obtained without optimizing the design for overlap between the fundamental and second harmonic modes, since no Bloch modes are excited at the second harmonic frequency.

The demonstrated grating design delivers a blueprint for an efficient integrated source of entangled photons. Frequency-degenerate spontaneous parametric down conversion [175], which is a reverse process to SHG, allows free-space pumping at $\lambda_{\text{pump}} = 750$ nm to resonantly generate waveguide-coupled pairs of telecom photons, opening the use of DBEs in quantum optics and secure communications [176].

5.5 Conclusion

We have designed and analyzed a nonlinear grating that supports a degenerate band edge (DBE), a fourth-order exceptional point of degeneracy, as a means to enhance second harmonic generation (SHG) without phase matching and without exciting any Bloch modes at the second harmonic frequency. Operating the mirrorless double grating close to the DBE frequency causes very large field intensities I_1 at the DBE resonance, whose maximum scales as $N^{3.6}$, close to the expected N^4 expected from the literature. Additionally, we have shown the asymptotic $N^{4.94}$ quality factor scaling with waveguide length for a large number of unit cells N up to 300. This behavior is a direct result of the DBE-associated frozen mode regime.

Building on this linear response, we have demonstrated that the resulting field enhancement leads to efficient second harmonic generation. The second harmonic field, which leaks vertically out of the structure, has been shown to follow the same spatial distribution as the square of the fundamental field. Our simulations show that the DBE-enhanced nonlinear conversion efficiency asymptotically scales as $\eta \propto N^{8.27}$ for large N, highlighting the effectiveness of the DBE mechanism in boosting light-matter interactions, even without phase matching and in the absence of Bloch modes at the second harmonic frequency. Additionally, when the efficiency is normalized by the square of the waveguide length, the DBE-supporting double grating displays an efficiency surpassing the state-of-the-art, demonstrating a strong potential for the miniaturization of integrated photonic nonlinear sources.

These results establish the DBE as a powerful mechanism for compact and efficient nonlinear integrated photonic devices. The structure proposed here is compatible with existing material platforms and provides a robust, scalable approach for boosting nonlinear effects in applications ranging from on-chip frequency conversion to quantum photonic systems.

Acknowledgment

The authors declare no source of funding.

Disclosure

The authors declare no conflicts of interest.

Data availability statement

Data underlying the results presented in this paper are not publicly available at this time but may be obtained from the authors upon reasonable request.

Appendix A: Crystal cut dependence on the polarization of the fundamental field and the second harmonic

In an AlGaAs-based waveguide, the relationship between the polarization density vector at the second harmonic $\mathbf{P}_{2f}$ and the electric field at the fundamental frequency $\mathbf{E}_f$ depends on the crystal cut.

For a crystal cut in the [001] direction, with the x axis aligned with that of the waveguide, the second-order nonlinear susceptibility tensor is

$$\chi^{(2)} = \begin{bmatrix} 0 & 0 & 0 & d_{14} & 0 & 0 \\ 0 & 0 & 0 & 0 & d_{14} & 0 \\ 0 & 0 & 0 & 0 & 0 & d_{14} \end{bmatrix}. \tag{5.13}$$

For a crystal cut in the [111] direction, the susceptibility tensor transforms to

$$\chi^{(2)} = \begin{bmatrix} -\frac{d_{14}}{\sqrt{3}} & -\frac{d_{14}}{\sqrt{3}} & \frac{2d_{14}}{\sqrt{3}} & \frac{d_{14}}{\sqrt{6}} & -\frac{d_{14}}{\sqrt{6}} & 0 \\ -\frac{d_{14}}{\sqrt{3}} & \frac{2d_{14}}{\sqrt{3}} & -\frac{d_{14}}{\sqrt{3}} & -\frac{d_{14}}{\sqrt{6}} & -\frac{d_{14}}{\sqrt{6}} & 0 \\ \frac{2d_{14}}{\sqrt{3}} & -\frac{d_{14}}{\sqrt{3}} & -\frac{d_{14}}{\sqrt{3}} & 0 & 0 & \frac{d_{14}}{\sqrt{2}} \end{bmatrix}. \tag{5.14}$$

From this, the out-of-plane (z-component) polarization density at the second harmonic is given by

$$P_z(2f) = \varepsilon_0 d_{14} \left(\frac{2}{\sqrt{3}} E_x^2(f) - \frac{1}{\sqrt{3}} E_y^2(f) - \frac{1}{\sqrt{3}} E_z^2(f) + \frac{1}{\sqrt{2}} E_x(f) E_y(f) \right). \tag{5.15}$$

In the special case where the fundamental field is entirely in the out-of-plane direction, i.e., $\mathbf{E}_f = E_z \hat{\mathbf{z}}$, the expression simplifies to

$$P_z(2f) = -\frac{\varepsilon_0 d_{14}}{\sqrt{3}} E_z^2(f). \tag{5.16}$$

This result is particularly relevant for our waveguide system, as the DBE-associated frozen mode at the fundamental frequency is a TE mode with $E_{1z} \neq 0$, leading to a second-harmonic TE mode with $E_{2z} \neq 0$.

Chapter 6

The Combination of the Azimuthally- and Radially-Polarized Beams: Helicity and Momentum Densities, Generation and Optimal Chiral Light

In this chapter, we show that the superposition of azimuthally and radially polarized beams forms an optimally chiral beam (ARPB) with purely longitudinal fields along its axis, achieving maximum helicity density for a given energy density. We derive closed-form expressions for its field components and electromagnetic quantities, and show that they hold great potential as probes for molecular chirality.

6.1 Introduction

Chirality is a geometrical property of objects that are not superimposable to their mirror images [177]. Chiral molecules, also known as enantiomers, have the same constitution but follow different chemical processes in a chiral environment [178]. As of 2016, 50% of FDA-approved drugs have chiral active ingredients [179], where one enantiomer initiates the desired chemical reaction and the other one acts as an antagonist [180]. Therefore, it is of supreme importance to develop efficient techniques to probe the chirality of enantiomers [181, 182, 183] and to separate them [184, 185].

Recently, a lot of interest has emerged in the interaction between chiral particles and chiral light [186], of which circularly polarized light (CPL) is the most common example [177]. The optical chirality density is [187, 188]

$$\mathcal{C} = \frac{1}{2}(\varepsilon_0 \mathcal{E} \cdot \nabla \times \mathcal{E} + \mu_0 \mathcal{H} \cdot \nabla \times \mathcal{H}), \tag{6.1}$$

where μ_0 and ε_0 are the absolute permeability and permittivity in vacuum, respectively. The symbols $\mathcal{E}$ and $\mathcal{H}$ denote the real electric and magnetic fields. The optical chirality density $\mathcal{C}$ is a specific dynamical property of light that is conserved in vacuum. While it does not directly account for all chiral light-matter interactions [189], $\mathcal{C}$ is relevant in interactions involving the interference between electric and magnetic dipoles exhibited by chiral media [187, 188].

In this paper, we focus on monochromatic fields with the implicit time dependence $e^{-i\omega t}$, where ω is the angular frequency of light. The time-averaged helicity density h is defined as [190, 70, 71]

$$h = \frac{1}{2\omega c}\Im\left(\mathbf{E}\cdot\mathbf{H}^{*}\right), \tag{6.2}$$

in terms of the electric and magnetic field phasors, $\mathbf{E}$ and $\mathbf{H}$, respectively. The symbol $c = 1/\sqrt{\varepsilon_0\mu_0}$ is the speed of light in vacuum. We will focus on h because it is more transparently connected to physical quantities of the field, such as the spin angular momentum density [191] and photon number [192] than the time-averaged version of the optical chirality density, C, whose expression is given in Refs. [188, 182, 193] and in the Supplementary Information of Ref. [70]. In quantum particle physics, the helicity density h is determined by the product of the spin and momentum densities [69], and in electromagnetism it is a locally-independent property related to the dual symmetry between the electric and the magnetic field [194]. For monochromatic fields, the time-averaged helicity and optical chirality densities are related as $C = \omega^2 c^{-1} h$ [70]. Even though they are both real pseudoscalars, the direction of the field components they stem from is important in chiral-light matter interactions, as reported in Ref. [72]. For instance, chiral particles can exhibit an anisotropic chiral polarizability, based on their dipolar description. See Refs. [72, 195] for details. This results in a distinct chiral response when the particles are probed by beams with either transversely or longitudinally polarized fields. Therefore, it is convenient to divide a beam's scalar helicity density into its constituents, i.e.,

$$h = h_{\perp} + h_{z}, \tag{6.3}$$

where $h_{\perp} = \Im\left(\mathbf{E}_{\perp}\cdot\mathbf{H}_{\perp}^{*}\right)/(2\omega c)$ stems purely from the transverse field components, perpendicular to the beam propagation direction, and $h_z = \Im\left(E_z H_z^{*}\right)/(2\omega c)$, originates from the longitudinal components (i.e., along the beam propagation direction).

The chiroptical response of natural chiral systems, however, is very weak [196]. The response depends on the amount of helicity density of light, as observed in the photoinduced forces reported in Ref. [197] (although it is not the main result of the paper) and in Ref. [71], as well as in the dissymmetry factor g in Ref. [187].

The concept of helicity maximization to its upper bound was introduced in Ref. [70], which showed that the magnitude of the helicity density h of a free-space monochromatic field has an upper bound, i.e., $|h| \leq u/\omega$, where u is the energy density of light. As a consequence, optimally chiral light (OCL) was defined as a local property of free-space monochromatic field that exhibits *maximum helicity density at a given energy density*. When light is not optimally chiral, one has $|h| < u/\omega$. Measurement of chirality dipolar polarizability, associated to the geometrical chirality of a sample nanoparticle, with OCL, yields a dissymmetry factor g that is determined solely by the sample's dipolar polarizabilities [70], and not by the electric or magnetic intensity and energy of the beam's light. As shown in Ref. [70], circularly polarized light (CPL) represents a specific case of the broader category known as OCL. CPL exhibits maximum helicity density at a given energy density, and that is why it has been used so successfully to detect the chirality of matter. However, the results in Ref. [70] show that there are countless other examples of structured light that are optimally chiral, and the special beam studied in this paper is a useful and simple example.

Emerging strategies attempt to maximize chiral light-matter interactions by enhancing the optical chirality density using dielectric [198, 199, 185, 200] or plasmonic nanostructures [201, 202, 203]. It is shown in Ref. [204] that the average chirality of the near field of plasmonic nanostructures cannot be significantly higher than that in freely-propagating plane waves. These studies so far have only considered nanostructures illuminated with CPL, whose optical chirality (i.e., helicity) density is caused by purely transverse fields (i.e., $h = h_{\perp}$), or with linearly polarized light [205] for enhanced optical rotation measurements. However, Gúzman Rosales et al. [206] highlighted the importance of longitudinal field components in chiral interactions. Indeed, for a dipolar particle with an isotropic chiral polarizability, a beam with an optical chirality density stemming from transverse fields, such as CPL, can only reveal its chirality on the transverse plane, which could be mistaken with its dielectric or magnetic anisotropy as the sample is simultaneously probed in two directions (x and y) when using CPL [186]. In contrast, a beam with an axial helicity density that originates from purely longitudinal fields, i.e., $h = h_z$, only probes the particle's chiral polarizability along one direction (z). This property is crucial for a few different scenarios: (i) for probing nanoparticle samples that express a dipolar polarizability of tensorial form with only the zz component that is chiral; (ii) for particles characterized by an anisotropic dipolar chiral polarizability, the actual response depends on the beam's polarization, and separately probing the particle with chiral beams featuring purely transverse and longitudinal fields provides complementary information, as shown in Fig. (6) of Ref. [72]; and (iii) for particles that have a transverse electric or magnetic anisotropic polarizability that would confuse the chirality measurements if one uses CPL.

Therefore, it is important to study optimally chiral beams with an optical chirality density that stems from purely longitudinal fields on their axis, i.e., they have $|h_z| = u/\omega$. An example of this kind of beam is the azimuthally-radially polarized beam (ARPB) [72] that is a superposition of an azimuthally polarized beam (APB) [207, 208, 209, 210, 211] and a radially polarized beam (RPB) [212, 213, 214]. In Ref. [215], the authors tightly focus an achiral beam resulting from the *in-phase* superposition of an APB and an RPB to excite a chiral dipole moment in a geometrically achiral nanostructure by carefully adapting the excitation wavelength to balance the induced electric and the magnetic dipole moments in the nanostructure. Here, instead, we examine out-of-phase superpositions of these two beams, which result in chiral ARPBs. The APB, RPB, and ARPB examined in this study are particular instances of the broader category of spirally polarized beams developed by Gori in Ref. [216]. We choose to retain the designation of *azimuthally-radially polarized*

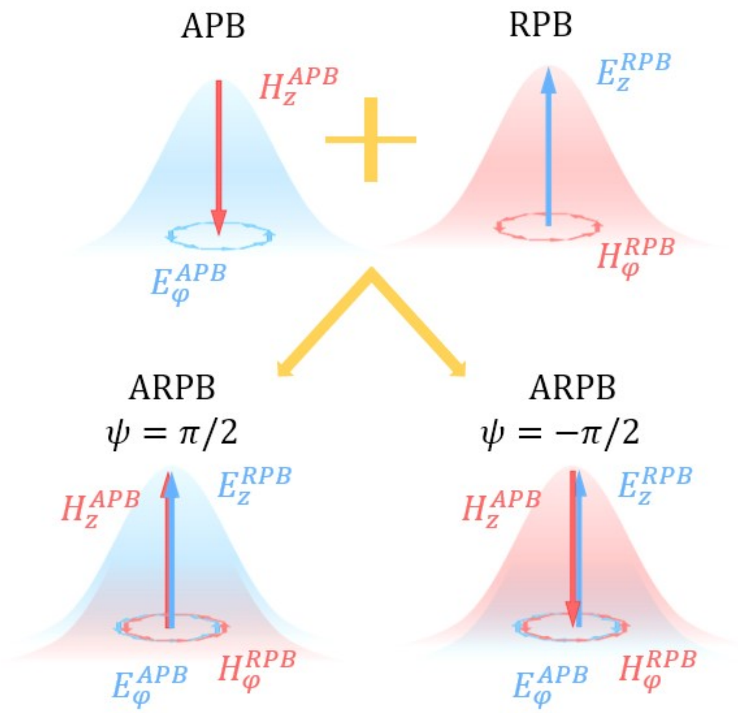

Figure 6.1: Conceptual representation of the APB, the RPB, and the ARPB as their combination with a phase delay of $\psi = \pm\pi/2$. The electric field is represented in blue and the magnetic field in red. The radial components of the fields are not shown. The bell curve denotes the Gaussian-like parameter f. In the ARPB with $\psi = \pi/2$, the electric field $\mathbf{E}$ (blue bell curve) leads in time to the magnetic field $\mathbf{H}$ (red bell curve), and the opposite (lagging) occurs when $\psi = -\pi/2$.

beam from previous work [72, 70, 73, 74] because it encapsulates the combination of an APB and an RPB. This composition results in purely longitudinal electric and magnetic fields on the beam axis, which are important to build an on-axis helicity density that stems *only* from longitudinal field components, i.e., $h = h_z$.

The phase-shift ψ and the ratio of amplitudes $\hat{V}$ between the APB and the RPB can be tuned to produce an ARPB with optimal chirality, which we refer to as an optimally chiral ARPB (OC-ARPB). This occurs when $\psi = \pm\pi/2$ and $\hat{V} = 1$, as initially reported by Hanifeh et al. in Ref. [70]. Figure 6.1 displays schematic views of an APB, an RPB, and two distinct configurations of an OC-ARPB. For $0 < \psi < \pi$, the electric field leads the magnetic field, while the opposite occurs for $-\pi < \psi < 0$. The transverse fields of the ARPB vanish on the beam axis, where the longitudinal fields persist [72, 70, 73, 74]. This spatial separation is shown in Figures 6.2(a) and (b), which respectively depict the propagation of the magnitude of the transverse $\mathbf{E}_\perp = E_\rho \hat{\boldsymbol{\rho}} + E_\varphi \hat{\boldsymbol{\varphi}}$ and longitudinal E_z electric fields of the ARPB.

Both the OC-ARPB and CPL are part of the broader category of OCL. However, the key distinction is that the OC-ARPB exhibits an optical chirality density that originates exclusively from longitudinal fields along the beam axis (i.e., helicity density h_z), the chirality density of CPL completely stems from fields in the transverse-to-z plane (i.e., helicity density $h_\perp$). Therefore, as discussed in Ref. [72], each beam is suitable for different and complementary matter-chirality probing. CPL can only probe the transverse chiral polarizability of particles, however, as mentioned, it also probes the particle's transverse anisotropy, whereas the APRB exclusively measures the longitudinal chirality of a sample oriented in the same direction as the beam. Additionally, the different chirality densities displayed by the ARPB and CPL affect possible designs of chirality-discriminating optical traps, as discussed in Ref. [217]. Preliminary theoretical results also show that illuminating dielectric nanospheres with an OC-ARPB results in almost twice the helicity density enhancement than using a CP Gaussian beam [70]. Other investigations into beams with a chirality density stemming from purely longitudinal fields, including Gúzman Rosales et al [206], study the optical chirality of beams with orbital angular momentum (OAM) [206, 218, 219, 220, 221, 222, 223]. Potential applications of the OC-ARPB (and other forms of vector beams with a chirality density that stems from purely longitudinal fields) include enhancing circular dichroism signals of nanoparticles [224], improving a magnet-free magnetic circular dichroism [225], and measuring the spatial features of chirality of nanoparticles at nanoscale [72].

In this paper, we further advance the concept of a chiral ARPB, defined in terms of an arbitrary relative amplitude $\hat{V}$ and phase shift ψ between the APB and the RPB, as in Refs. [70, 73, 226, 74]. We introduce a concise notation for the APB and the RPB in Section 6.2. The ARPB is described in Section 6.3, and the analytical expressions for its

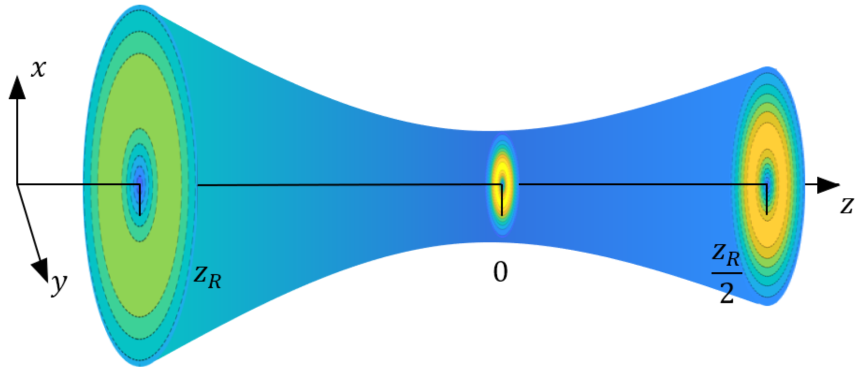

(a)

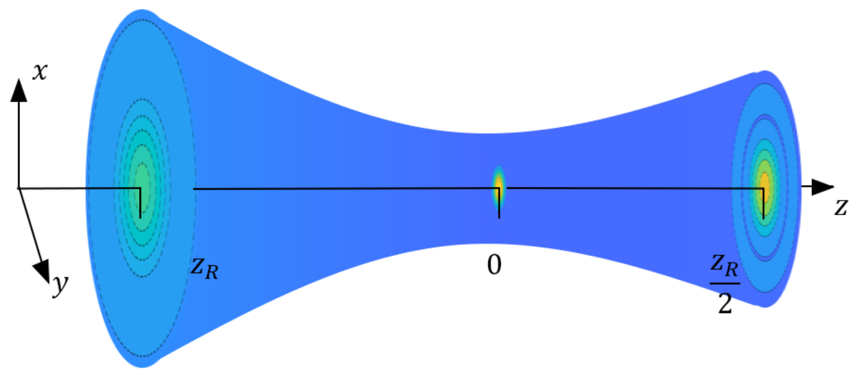

(b)

Figure 6.2: Schematic representation of propagation and localization of the (a) transverse $\mathbf{E}_\perp = E_\rho \hat{\boldsymbol{\rho}} + E_\varphi \hat{\boldsymbol{\varphi}}$, and (b) longitudinal E_z fields of an ARPB with $w_0 = \lambda = 400$ nm. The E_z field is localized on the axis. The same happens for the magnetic field, with H_z localized on the axis.

field quantities are provided in Section 6.4. In Section 6.5, we focus on the OC-ARPB and its exceptional electric-magnetic symmetry. To support future experimental studies, we discuss setups that generate an ARPB in Section 6.6. The conclusions are found in Section 6.7.

6.2 Cylindrical polarization basis

A structured beam with a helicity density that ensues from purely longitudinal fields on its axis is built here by combining two beams that have exclusively longitudinal electric and magnetic field components on their axis. Therefore, combining the APB and the RPB fits this purpose. These beams are obtained as a combination of normalized Laguerre-Gaussian (LG) beams. This class of beams is generally referred to as spirally polarized beams [216], of which the APB and the RPB described herein are specific instances. The APB is obtained by a combination of two circularly polarized LG beams with opposite orbital angular momentum (OAM) and handedness, i.e.,

$$\mathbf{E}^{\mathrm{APB}} = \frac{i\sqrt{2}}{2} V_{\mathrm{A}} \left(u_{1,0}\, \hat{\boldsymbol{e}}_{\mathrm{RH}} - u_{-1,0}\, \hat{\boldsymbol{e}}_{\mathrm{LH}} \right) e^{ikz}, \tag{6.4}$$

where V_A is the complex amplitude of the APB, and the circular unitary vectors are $\hat{\boldsymbol{e}}_{\mathrm{RH}} = (\hat{\boldsymbol{x}} - i\hat{\boldsymbol{y}})/\sqrt{2}$ for right-circularly polarized light and $\hat{\mathbf{e}}_{\mathrm{LH}} = (\hat{\boldsymbol{x}} + i\hat{\boldsymbol{y}})/\sqrt{2}$ for left-circularly polarized light [70]. Thus, in this paper, we restrain our analysis to combinations of LG beams with $u_{\pm1,0}$ (zero axial index and a topological charge $l = \pm1$), [227, 228, 207]

$$u_{\pm1,0} = \frac{2\rho}{\sqrt{\pi} w^2} e^{-(\rho/w)^2 \zeta} e^{-2i \tan^{-1}(z/z_R)} e^{\pm i\varphi}, \tag{6.5}$$

where $w = w_0\sqrt{1 + (z/z_R)^2}$ represents the beam radius, and w_0 is defined as half the beam waist parameter at $z = 0$. The Gouy phase is given by $\zeta = 1 - iz/z_R$, and the Rayleigh range is expressed as $z_R = \pi w_0^2/\lambda$, where λ is the free-space wavelength. The wavenumber is $k = 2\pi/\lambda$.

The magnetic field of the RPB, $\mathbf{H}^{\mathrm{RPB}}$, has an analogous representation as (6.4) after substituting the weight V_A (with unit of Volts) with V_R/η_0, where $\eta_0 = \sqrt{\mu_0/\varepsilon_0}$, is the characteristic impedance of free space. To facilitate our analysis of the helicity density of the resulting ARPB, we have opted to introduce a more concise notation in the cylindrical basis (ρ, φ,

z). The non-zero field components of the APB are

$$
\begin{aligned}
E_{\varphi}^{\mathrm{APB}} &= \tfrac{\rho}{w^2} V_A f, \\
H_{\rho}^{\mathrm{APB}} &= -\tfrac{\rho}{w^2 \eta_0} V_A f \left(A_\rho + i B_\rho\right), \\
H_{z}^{\mathrm{APB}} &= -\tfrac{2i}{k w^2 \eta_0} V_A f \left(A_z + i B_z\right),
\end{aligned} \tag{6.6}
$$

and those of the RPB

$$
\begin{aligned}
H_{\varphi}^{\mathrm{RPB}} &= \tfrac{\rho}{w^2 \eta_0} V_R f, \\
E_{\rho}^{\mathrm{RPB}} &= \tfrac{\rho}{w^2} V_R f \left(A_\rho + i B_\rho\right), \\
E_{z}^{\mathrm{RPB}} &= \tfrac{2i}{k w^2} V_R f \left(A_z + i B_z\right).
\end{aligned} \tag{6.7}
$$

The dimensionless shorthand parameters are

$$
\begin{aligned}
f &= \tfrac{2}{\sqrt{\pi}} e^{-(\rho/w)^2 \zeta} e^{-2i \tan^{-1}(z/z_{\mathrm{R}})} e^{ikz}, \\
A_\rho &= 1 + \tfrac{1}{k z_R} \tfrac{\rho^2 - 2 w_0^2}{w^2} + \left(\tfrac{2 z \rho}{w^2 k z_R}\right)^2, \\
B_\rho &= -\tfrac{4}{w^2} \tfrac{1}{k^2} \tfrac{z}{z_R} \left(1 - \tfrac{\rho^2}{w^2}\right), \\
A_z &= 1 - \tfrac{\rho^2}{w^2}, \\
B_z &= \tfrac{z}{z_R} \tfrac{\rho^2}{w^2}.
\end{aligned} \tag{6.8}
$$

While the parameters A_ρ, B_ρ, A_z, and B_z described in Equation (6.8) are real, but the parameter f is complex and related to the normalized Laguerre-Gaussian (LG) modes as $f = \frac{w^2}{\rho} u_{\pm 1,0} e^{\mp i\varphi} e^{ikz}$. Further elaboration on this subject can be found in Section A of the Supporting Information, where we show the APB electric field in different polarization bases.

Comparing Equations (6.6) and (6.7) shows that the APB and the RPB are electromagnetically dual. When they have the same beam parameters, their fields are related as [74]

$$\begin{aligned} \mathbf{E}^{\mathrm{APB}} &= \eta_0 \mathbf{H}^{\mathrm{RPB}} \left(\tfrac{V_{\mathrm{A}}}{V_{\mathrm{R}}}\right), \\ \mathbf{E}^{\mathrm{RPB}} &= -\eta_0 \mathbf{H}^{\mathrm{APB}} \left(\tfrac{V_{\mathrm{R}}}{V_{\mathrm{A}}}\right). \end{aligned} \tag{6.9}$$

The APB/RPB only has non-zero longitudinal magnetic/electric field on the axis ($\rho = 0$).

6.3 The azimuthally-radially polarized beam

The ARPB is formed by adding an APB and an RPB, with a complex amplitude ratio given by $V_A/V_R = \hat{V} e^{i\psi}$. Since the APB and RPB have magnetic and electric longitudinal fields on their axis, respectively, the ARPB has *both* electric and magnetic longitudinal fields that can be properly phase-shifted to generate *a helicity density that stems from longitudinal fields*, i.e., $h_z = \Im\left(E_z H_z^*\right)/(2\omega c)$. The parameter $\hat{V}$ monitors the relative magnitudes of the two beams, while their relative phase shift ψ is referred to as the phase parameter as in Ref. [72]. The combined fields of the ARPB are

$$\begin{aligned} \mathbf{E}^{\mathrm{ARPB}} = \mathbf{E}^{\mathrm{APB}} + \mathbf{E}^{\mathrm{RPB}} &= \tfrac{f V_R}{k w^2} \left[k\rho \left(A_\rho + i B_\rho\right) \hat{\boldsymbol{\rho}} + k\rho \hat{V} e^{i\psi} \, \hat{\boldsymbol{\varphi}} + 2i \left(A_z + i B_z\right) \hat{\boldsymbol{z}} \right], \\ \mathbf{H}^{\mathrm{ARPB}} = \mathbf{H}^{\mathrm{APB}} + \mathbf{H}^{\mathrm{RPB}} &= -\tfrac{f V_R}{k w^2 \eta_0} \left[k\rho \hat{V} e^{i\psi} \left(A_\rho + i B_\rho\right) \hat{\boldsymbol{\rho}} - k\rho \, \hat{\boldsymbol{\varphi}} + 2i \hat{V} e^{i\psi} \left(A_z + i B_z\right) \hat{\boldsymbol{z}} \right], \end{aligned} \tag{6.10}$$

which are purely longitudinal on the beam axis. Note that the field components in cylindrical coordinates do not show an azimuthal dependence. In Ref. [207], the authors demonstrate that as w_0 of an APB decreases, its longitudinal magnetic field component H_z increases at a faster rate compared to its transverse fields $\mathbf{E}_\perp$ and $\mathbf{H}_\perp$. As a result of the APB/RPB duality shown in Eq. (6.9), this phenomenon is also observed in the longitudinal electric field component E_z^{RPB} of an RPB. Consequently, the longitudinal fields of the ARPB increase more rapidly than the transverse fields as w_0 decreases. This feature is important when we calculate the helicity density that stems from exclusively longitudinal fields, i.e., h_z, in Section 6.4.

6.4 ARPB field quantities

We provide the cycle-averaged densities of specific field quantities of the ARPB that play a critical role in local chiral light-matter interactions [187, 197, 229]. The cycle-averaged energy density of a monochromatic EM field is $u = \varepsilon_0|\mathbf{E}|^2/4 + \mu_0|\mathbf{H}|^2/4$ [230], and the cycle-averaged complex Poynting vector is $\mathbf{S} = (\mathbf{E} \times \mathbf{H}^*)/2$ [231]. Its real part is associated with the linear momentum density $\mathbf{p} = \Re(\mathbf{S})/c^2$ as in Ref. [231], while the imaginary part is associated with the reactive energy flux density of the field. The cycle-averaged spin angular momentum (SAM) density is $\boldsymbol{\sigma} = -\frac{\varepsilon_0}{4i\omega}(\mathbf{E} \times \mathbf{E}^*) - \frac{\mu_0}{4i\omega}(\mathbf{H} \times \mathbf{H}^*)$, and the cycle-averaged helicity density is shown in Eq. (6.2). While the energy and SAM densities naturally split into electric and magnetic field contributions, i.e., $u = u_e + u_m$ and $\boldsymbol{\sigma} = \boldsymbol{\sigma}_e + \boldsymbol{\sigma}_m$, the Poynting vector $\mathbf{S}$ and the helicity density h depend on the interaction between the electric and magnetic fields of the beam. In this section, our focus is exclusively on the final expressions for the field quantities of the ARPB. Additional information about the field quantities of the APB, the RPB, and the ARPB can be found in Section B of the Supporting Information. To make the field quantities easier to comprehend, we express them as a combination of a normalization constant (denoted by the subscript 0) and a dimensionless term. The energy density of an ARPB is

$$u^{\mathrm{ARPB}} = \tfrac{1}{2}u_0 \left(1+\hat{V}^2\right) \left[(k\rho)^2 \left(1+A_\rho^2+B_\rho^2\right) + 4\left(A_z^2+B_z^2\right)\right], \tag{6.11}$$

where $u_0 = \frac{\varepsilon_0|f|^2}{2k^2w^4}|V_R|^2$. Its value does not depend on ψ. The energy density of an ARPB describes an annular ring in the transverse plane. The components of the Poynting vector $\mathbf{S}^{\mathrm{ARPB}}$ of an ARPB are

$$\begin{aligned} S_\rho^{\mathrm{ARPB}} &= iS_0\left[\,\hat{V}^2(A_z - iB_z) - (A_z + iB_z)\,\right], \\ S_\varphi^{\mathrm{ARPB}} &= -2S_0\hat{V}\left(\sin\psi + i\cos\psi\right)\left(A_\rho A_z + B_\rho B_z\right), \\ S_z^{\mathrm{ARPB}} &= \tfrac{1}{2}S_0 k\rho\left[\,\hat{V}^2(A_\rho - iB_\rho) + (A_\rho + iB_\rho)\,\right]. \end{aligned} \tag{6.12}$$

where $S_0 = \frac{\rho|f|^2}{k\eta_0 w^4}|V_R|^2 = 2\rho\omega u_0$. Note that S_0 vanishes on the beam axis, while u_0 does not. When $\hat{V} = 1$, the longitudinal and radial energy flux density, S_z^{ARPB} and S_ρ^{ARPB}, are purely real. Moreover, near its focal plane ($z \approx 0$), the radial component of the Poynting vector of an ARPB with $\hat{V} = 1$ is negligible: $S_\rho^{\mathrm{ARPB}} \propto B_z \approx 0$ W/m^2 (see Eq. (6.8)). Therefore, most of the energy density flows in the z direction and the ratio of active versus reactive energy flux density in the azimuthal direction depends on the phase parameter ψ. For $\psi \neq 0, \pi$, which is the case for chiral ARPBs, there is a nonzero azimuthal linear momentum density $p_\varphi = \Re(S_\varphi)/c^2$. While the ARPB is not a conventional vortex beam since it does not have a phase variation around the axis (usually characterized by $e^{il\varphi}$) [232], it exhibits a power flow around the axis. The reason is because of the out-of-phase combination of an APB and an RPB, which do not individually exhibit an azimuthal power flow (see Eq. (S5) of the Supplementary Information, Section B, for further details). Therefore, the azimuthal power flow necessarily implies the existence of a ψ-dependent orbital angular momentum (OAM) density in the longitudinal direction [233, 234, 235]. The longitudinal OAM density of a field in cylindrical coordinates is calculated as $l_z = p_\varphi \rho - \sigma_z$ (see Eq. (S8) and (S9) of the Supplementary Information, Section B, for more information), which for an ARPB is

$$l_z^{\mathrm{ARPB}} = l_0 \hat{V} \sin(\psi) \left[2(A_\rho A_z + B_\rho B_z) + A_\rho \right], \tag{6.13}$$

where $l_0 = -\frac{\varepsilon_0 \rho^2 |f|^2}{\omega w^4} |V_R|^2$. The longitudinal OAM density vanishes on the beam axis, where the fields are purely longitudinal. Despite being composed of two beams, namely, the APB and the RPB, each with zero longitudinal OAM densities, the ARPB exhibits a non-zero longitudinal OAM density for $\psi \neq 0$. A chiral ARPB carries an l_z that reaches a maximum for $\psi = \pm\pi/2$, which is the case for OCL as discussed in Section 6.5. Additionally, the OAM density of an ARPB can be continuously tuned by varying the phase parameter ψ, in contrast with the discrete azimuthal phase dependence $e^{il\varphi}$ of LG vortex beams, where l is the topological charge [194]. As shown later in Section 6.6, the value of ψ is readily accessible by means of standard optical elements (beam splitters, mirrors, and wave plates), while varying l generally requires elaborate optical elements, including Q-plates [236], spatial light modulators (SLMs)[237], spiral phase plates [238], or cylindrical lenses [239, 240].

The components of the SAM density $\boldsymbol{\sigma}^{\mathrm{ARPB}}$ of the ARPB are

$$\begin{aligned} \sigma_\rho^{\mathrm{ARPB}} &= 2\sigma_0 \hat{V} \sin(\psi) B_z, \\ \sigma_\varphi^{\mathrm{ARPB}} &= -\sigma_0 \left(1 + \hat{V}^2\right) \left[A_\rho A_z + B_\rho B_z \right], \\ \sigma_z^{\mathrm{ARPB}} &= \sigma_0 k \rho \hat{V} \sin(\psi) A_\rho, \end{aligned} \tag{6.14}$$

where $\sigma_0 = \frac{\varepsilon_0 \rho |f|^2}{\omega k w^4} |V_R|^2 = S_0/(\omega c)$ vanishes on axis. While the azimuthal SAM density $\sigma_\varphi^{\mathrm{ARPB}}$ is the sum of the SAM densities of the individual APB and RPB (see Supporting

Information, Section B), the radial and longitudinal components of the SAM density arise from the interaction between the two beams and therefore depend on the phase parameter ψ.

The time-averaged helicity density h^{ARPB} of an APRB, defined in Eq. (6.2), is decomposed based on the field components in cylindrical coordinates as $h = \Im\left(E_\rho H_\rho^* + E_\phi H_\phi^* + E_z H_z^*\right)/(2\omega c)$, leading to $h = h_\rho + h_\phi + h_z$ with

$$
\begin{aligned}
h_\rho &= h_0 \hat{V} \sin(\psi)(k\rho)^2 \left(A_\rho^2 + B_\rho^2\right), \\
h_\varphi &= h_0 \hat{V} \sin(\psi)(k\rho)^2, \\
h_z &= 4h_0 \hat{V} \sin(\psi)\left(A_z^2 + B_z^2\right),
\end{aligned}
\tag{6.15}
$$

where $h_0 = \frac{\varepsilon_0 |f|^2}{2\omega k^2 w^4}|V_R|^2$. The normalization parameters of the energy u_0 and helicity h_0 densities are related as $h_0 = u_0/\omega$. Note that h_0 and u_0 do not vanish on the axis, while S_0, σ_0, and l_0 do vanish there, and that is why there is a special relation between h_0 and u_0. Also, h_ρ and h_ϕ vanish on the beam axis, whereas the term h_z is the only one that does not vanish there. This means that on the beam's axis, h_z reaches the upper bound of $|h_z| = u/\omega$ when $\psi = \pm\pi/2$. This makes the ARPB a tool to detect the chiral dipolar polarizability nanoparticles located on its axis. Since only E_z and H_z make the light helicity density on the beam axis, a detection mechanism based on only these longitudinal field components would not be sensitive to the nanoparticle electric or magnetic anisotropic polarizability. The total helicity density of an ARPB is also related to its energy density (shown in Eq. (6.11)) as

$$
h^{\mathrm{ARPB}} = \frac{u^{\mathrm{ARPB}}}{\omega} \frac{2\hat{V}}{1+\hat{V}^2} \sin(\psi). \tag{6.16}
$$

For $\hat{V} = 1$, the helicity density is in agreement with the expressions in Eq. (13.28) and (13.29) of Ref. [74]. For $\psi = 0, \pi$, the interaction between the fields of the APB and the RPB is minimized; the energy u, linear momentum $\mathbf{p}$, SAM $\boldsymbol{\sigma}$, longitudinal OAM l_z, and helicity h densities of the resulting ARPB are the sum of those of the APB and the RPB (see Section B of the Supporting Information for details). Conversely, for $\psi = \pm\pi/2$, which corresponds to the OC-ARPB as shown in Section 6.5, the interaction between the APB and the RPB is maximized. The OC-APRB displays maximum linear momentum, SAM, OAM, and helicity densities. In essence, the phase parameter ψ mediates the interaction between the fields of the APB and the RPB. The OAM and helicity densities originate from the out-of-phase superposition of the APB and the RPB, which is determined by the phase parameter ψ. Notably, the helicity density of the ARPB does not depend on an explicit topological charge l, in contrast with what happens with focused LG beams $u_{l,p}$ [222] whose helicity density depends on l directly. In quantum particle physics, the helicity density is defined as the projection of the spin density onto the linear momentum density [69]. Employing this definition yields identical values for h as utilizing the ARPB helicity density expression in Eq. (6.16).

Moreover, the ARPB displays an exceptional spatial separation between the longitudinal and transverse fields, which vanish on the beam axis. As a consequence, the energy u, linear momentum $\mathbf{p}$, SAM $\boldsymbol{\sigma}$, longitudinal OAM l_z, and helicity h densities describe an annular ring in the transverse plane. On the z axis, only the contribution of the longitudinal fields to the energy and helicity densities, shown respectively in Eqs. (6.11) and (6.16), persist.

6.5 Optimally chiral ARPB

It was demonstrated in Ref. [70] that the helicity density of a chiral monochromatic field is locally bounded by its energy density as

$$-\frac{u}{\omega} \le h \le \frac{u}{\omega}. \tag{6.17}$$

By definition, OCL is a local descriptor that monochromatic structured light reaches the upper or lower bound of the helicity density. It occurs for fields whose phasors locally satisfy $\mathbf{E} = \pm i\eta_0\mathbf{H}$, which is referred to as the optimal chirality condition [70]. This is equivalent to the condition that the field phasors of OCL must satisfy

$$\begin{aligned} \nabla \times \mathbf{E} &= \pm k\mathbf{E}, \\ \nabla \times \mathbf{H} &= \pm k\mathbf{H}. \end{aligned} \tag{6.18}$$

Thus, for OCL, the magnitude of the cycle-averaged optical chirality density C in Eq. (6.1), reaches its upper bound $|C| = ku$.

In this paper, we find it convenient to use the normalized (and dimensionless) helicity density $\hat{h} = h\omega/u$, whose magnitude is bounded by unity, i.e., $-1 \le \hat{h} \le 1$. It is naturally split into the components that stem from the transverse $\hat{h}_\perp = h_\perp\omega/u$ and longitudinal $\hat{h}_z = h_z\omega/u$ field components, with $|\hat{h}_\perp + \hat{h}_z| \le 1$. The normalized helicity density $\hat{h}^{\mathrm{ARPB}}$ of the ARPB is reduced to

$$\hat{h}^{\mathrm{ARPB}} = \frac{2\hat{V}}{1+\hat{V}^2}\sin(\psi), \tag{6.19}$$

which does not depend on the parameters of the beam or on the position where the field is evaluated. This result is confirmed in Figure 6.4(a), which shows the normalized helicity density (computed as $h\omega/u$ and evaluated at an arbitrary position with $\rho \leq 20w_0$ and $|z| \leq 10z_R$) versus $\hat{V}$ and ψ. The respective maximum and minimum normalized helicity densities are found for $\hat{V} = 1$, $\psi = \pm\pi/2$ rad. Figure 6.4(b) denotes the vertical cross-section of Figure 6.4(a) for $\hat{V} = 1$, which is identified as the sinusoidal term $\hat{h} = \sin(\psi)$ in Eq. (6.19). Figure 6.4(c) shows the horizontal cross-section of Figure 6.4(a) for $\psi = \pi/2$, described by $\hat{h} = 2V/(1 + V^2)$. The ARPB is optimally chiral ($\hat{h} = \pm 1$) when the APB leads or lags the RPB by a quarter of a period and the beams have amplitudes of the same magnitude, i.e., $V_A = \pm iV_R$, in agreement with what was observed in Ref. [70]. This condition is equivalent to the optimal chirality condition $\mathbf{E} = \pm i\eta_0\mathbf{H}$. Indeed, the fields of an ARPB with $V_A = \pm iV_R$ are

$$\begin{aligned}
\mathbf{E}_\perp &= \tfrac{\rho}{w^2} f V_R \left[(A_\rho + iB_\rho)\ \hat{\boldsymbol{\rho}} \pm i\,\hat{\boldsymbol{\varphi}} \right], \\
\mathbf{H}_\perp &= \mp i\mathbf{E}_\perp/\eta_0, \\
E_z &= \tfrac{2i}{kw^2} f V_R \left(A_z + iB_z \right), \\
H_z &= \mp iE_z/\eta_0.
\end{aligned} \tag{6.20}$$

Even though the OC-ARPB attains its maximum helicity density on an annular ring around the beam axis (with the same topology as the energy density u), the relation $\mathbf{E} = \pm i\eta_0\mathbf{H}$, and therefore $\hat{h} = \hat{h}_\perp + \hat{h}_z = 1$, hold locally everywhere in space. Indeed, an OC-ARPB is approximately circularly polarized at the beam focus ($z = 0$, where $B_\rho = 0$) when $A_\rho \approx 1$, which occurs for collimated ARPBs, with $w_0 >> \lambda$. For details, see the Supplementary Information, Section C. Note that structured light does not need to be circularly polarized to be optimally chiral. Certainly, the transverse electric field in Eq. (6.20) is elliptically polarized and still $\mathbf{E}_\perp$ and $\mathbf{H}_\perp$ constitute optimally chiral light.

As discussed in Section 6.3, when w_0 decreases, the relative increase in the magnitude of the longitudinal fields compared to the transverse fields becomes more pronounced. Therefore, focusing an ARPB through a lens increases its energy density, and consequently, the upper bound of its chirality. Figure 6.4 illustrates this behavior by comparing the energy densities and the normalized helicity densities of three OC-ARPBs of 1 mW power with $w_0 = \lambda$, $w_0 = 2\lambda$, and $w_0 = 5\lambda$, where $\lambda = 400$ nm. Figures 6.4(a) and (b) show the energy density u of the three beams, at the focus and on the z axis, respectively. Focusing the ARPB by decreasing the ratio w_0/λ increases the energy density and, consequently, the helicity density. Figure 6.4(c) displays the components of the normalized helicity densities caused by the transverse $\hat{h}_\perp$ and longitudinal $\hat{h}_z$ field components. Although the most focused OC-ARPB has a larger helicity density, the region where it stems mostly from the longitudinal field components remains roughly the same, at approximately $\rho \approx 0.225\lambda$. These results indicate that enhancing the chiral light-matter interactions that depend on the helicity density is achievable by focusing the ARPB. However, in practice, the dominance of the helicity density caused by the longitudinal field components, i.e., $|h_z| > |h_\perp|$ is confined to a small spatial region regardless of the size of the beam. This limitation considerably constraints the size of the chiral sample to be probed, compared to standard paraxial optics measurements with CPL. The ARPB offers superior discrimination in chirality measurements due to its axial chirality density that stems from purely longitudinal fields, which makes a measurement insensitive to the anisotropic transverse electric or magnetic polarizability of a chiral particle. However, the limitation on the size of the chiral sample to be probed restricts the overall strength of the chiral responses.

As a result of the collinearity between the electric and magnetic field phasors, OCL displays an exceptional electric-magnetic symmetry in its energy and spin densities, i.e., $u_e = u_m$ and $\boldsymbol{\sigma}_e = \boldsymbol{\sigma}_m$ [70]. The Poynting vector $\mathbf{S}^{\text{OC-ARPB}}$ of an OC-ARPB is

$$\mathbf{S}^{\text{OC-ARPB}} = S_0 \left[\, 2B_z \hat{\boldsymbol{\rho}} \mp 2\left(A_\rho A_z + B_\rho B_z\right) \hat{\boldsymbol{\varphi}} + k\rho A_\rho \hat{\boldsymbol{z}} \,\right], \tag{6.21}$$

which is real-valued globally and, consequently, all the energy flux density contributes to the linear momentum density; an OC-ARPB has no reactive energy flux density. Moreover, the Poynting vector of an OC beam is collinear with its SAM density, as demonstrated in the Supplementary Information of Ref. [70]. For an OC-ARPB, the spin density $\boldsymbol{\sigma}^{\text{OC-ARPB}}$ is

$$\boldsymbol{\sigma}^{\text{ARPB}} = \sigma_0 \left[\, \pm 2B_z \hat{\boldsymbol{\rho}} - 2\left(A_\rho A_z + B_\rho B_z\right) \hat{\boldsymbol{\varphi}} \pm k\rho A_\rho \hat{\boldsymbol{z}} \,\right]. \tag{6.22}$$

As demonstrated here for the OC-ARPB, although it is easily verified that it applies for all OCL, $\mathbf{S} = \pm\omega c\boldsymbol{\sigma}$. Since the spin density is a real quantity, OCL has a purely real energy flux density $\mathbf{S} \in \Re$, and therefore a maximized linear momentum density $\mathbf{p} = \pm k\boldsymbol{\sigma}$, which changes sign for $\psi = +\pi/2$ or $\psi = -\pi/2$. The normalization constants of the Poynting vector and the spin density of the ARPB also follow the same relation $S_0 = \omega c\sigma_0$. Figure 6.5 displays the magnitudes of the (a) azimuthal and (b) longitudinal components of the Poynting vector of an OC-ARPB $\mathbf{S}^{\text{OC-ARPB}}$ on the transverse plane at the beam focus ($z = 0$). Its radial component S_ρ is approximately zero near the beam's focus (see Eq. (6.21), where $B_z \approx 0$). The azimuthal component S_φ has a peak described by a small ring around the beam axis. This occurs because it is partly associated with the longitudinal fields of the OC-ARPB, which peak on the beam axis. The longitudinal component of the Poynting vector S_z is associated with the transverse fields and therefore describes a bigger ring around the beam axis.

In summary, the OC-ARPB displays the enhanced chirality-probing capabilities characteristic of OCL, together with an exceptional spatial separation between the longitudinal and transverse field quantities. Unlike CPL, which only measures the transverse components of the chiral polarizability of a sample, the ARPB measures exclusively the chirality of the sample due to its longitudinal chiral polarizability along the beam axis, making it prefer-able because chirality measurements in the transverse plane can be mistaken for the sample electric or magnetic anisotropic polarizability [186, 72]. In the case of a particle with an anisotropic chiral response (i.e., with anisotropic chiral dipolar polarizability), both measurements are complementary and enable a more comprehensive characterization of the chirality of the sample [72] than standard chirality measurements. Using the ARPB beam as well as some other beams with an axial chirality density that stems from purely longitudinal fields, such as those discussed in Refs. [218, 219, 220, 221, 222, 223], eliminates the issues of the chiral-versus-anisotropy polarizability ambiguity by only measuring the longitudinal component of the chiral polarizability of a particle located on the beam axis. Recent studies on the optical chirality density of tightly-focused vortex beams [189, 241] shed light on the complex interplay between different tunable parameters of the vortex beams, such as the topological charge l, the degree of polarization, the ellipticity of the paraxial beam prior to tight-focusing, and the radial index of the vortex beam. In contrast, the ARPB has an extremely simple expression for the helicity density, which depends in a very straightforward manner on the tunable parameters of this beam, namely ψ and $\hat{V}$, as shown in Eq (6.16) and in Fig. 6.3. Additionally, the versatility of the ARPB extends to the ability to achieve optimal chirality, a feature not necessarily shared by other beams with an optical chirality density that originates from purely longitudinal fields.

6.6 ARPB generation

We show an optical setup that generates an ARPB with arbitrary $\hat{V}$ and ψ from an arbitrarily polarized laser source. An option to transform familiar wave polarization types (such as linear, circular, and elliptical) into vector modes (such as radial or azimuthal) is the use of an S-waveplate (SWP). The SWP is a combination of half-wave plate (HWP) segments whose slow axis is changed to maintain an azimuthal angle with respect to a reference axis [242], and can produce an APB, an RPB, or a combination of both by selective input polarization [214]. Its Jones matrix is [243]

$$\underline{\mathbf{H}}_S = \begin{pmatrix} \cos\varphi & \sin\varphi \\ \sin\varphi & -\cos\varphi \end{pmatrix}. \tag{6.23}$$

Table 6.1: SWP relevant input and output pairs. It provides the inputs required to obtain an RPB, an APB, and an ARPB with $\hat{V} = 1$ and arbitrary ψ, respectively. The superscript T denotes the transpose operator and φ is the azimuthal coordinate.

$\mathbf{J}_{in}$	$\to$	$\mathbf{J}_{out} = \underline{\mathbf{H}}_S \mathbf{J}_{in}$
$(1,\ 0)^T$	$\to$	$\mathbf{J}_{RPB} = (\cos(\varphi),\ \sin(\varphi))^T$
$(0,\ -1)^T$	$\to$	$\mathbf{J}_{APB} = (-\sin(\varphi),\ \cos(\varphi))^T$
$\frac{1}{\sqrt{2}}\left(1,\ -e^{i\psi}\right)^T$	$\to$	$\mathbf{J}_{ARPB} = \mathbf{J}_{RPB} + e^{i\psi}\mathbf{J}_{APB},$

The Jones vectors for relevant input/output pairs are summarized in Table 6.1 and depicted in Figure 6.6. In particular, Figure 6.6(a) shows that an x-polarized beam becomes an RPB, and Figure 6.6(b) that a y-polarized beam becomes an APB. Figure 6.6(c) and (d) illustrate the conversion of linearly polarized beams at angles $\theta = \mp\pi/4$ with respect to the x axis into achiral ARPBs with $\hat{V} = 1$ and either $\psi = 0$ or $\psi = \pi$, respectively. An ARPB with arbitrary $\hat{V}$ and ψ can be obtained by setting a linear polarizer at an angle θ from the x axis and adding a phase delay equal to ψ on the y-polarized component through a delay arm of length L, as shown in Figure 6.7. In this arrangement, the amplitude ratio $\hat{V}$ between the APB and the RPB is controlled by the angle θ of the linear polarizer relative to the x axis, which is given by

$$\hat{V} = |\tan(\theta)|. \tag{6.24}$$

To obtain $\hat{V} = 1$, the linear polarizer must be set to $\theta = \pm\pi/4$, where choosing the minus sign removes a 180° phase from the resulting APB upon conversion by the SWP. The length L of the delay arm sets the phase parameter ψ, and the two are related by the equation

$$kL - \tan^{-1}\left(\frac{L}{z_R}\right) = \psi, \tag{6.25}$$

which depends on λ and w_0.

An alternative method for introducing the phase delay ψ between the y- and x-polarized components of a linearly polarized beam relies on using a HWP and a quarter-wave plate (QWP). The Jones matrix of a HWP at angle θ_h with respect to the x axis is [244]

$$\underline{\mathbf{HWP}}(\theta_h) = \begin{pmatrix} -\cos(2\theta_h) & -\sin(2\theta_h) \\ -\sin(2\theta_h) & \cos(2\theta_h) \end{pmatrix}, \tag{6.26}$$

and that of a QWP at angle θ_Q is

$$\underline{\mathbf{QWP}}(\theta_q) = \begin{pmatrix} i\cos^2\theta_q + \sin^2\theta_q & (i-1)\cos\theta_q\sin\theta_q \\ (i-1)\cos\theta_q\sin\theta_q & i\sin^2\theta_q + \cos^2\theta_q \end{pmatrix}. \tag{6.27}$$

The resulting transformation reads

$$\mathbf{J}_{out} = \underline{\mathbf{HWP}}(\theta_h)\underline{\mathbf{QWP}}(\theta_q)\mathbf{J}_{in}. \tag{6.28}$$

The angle combinations that provide the ψ phase delay depend on the initial and final position of the polarization on the Poincaré sphere (see Ref. [244] for details). Replacing the delay arm in Figure 6.7 with the HWP and the QHP, as depicted in Figure 6.8, indicates that the incident polarization is $\mathbf{J}_{in} = (1,\ 1)^T$ and the final is $\mathbf{J}_{out} = (1,\ e^{i\psi})^T$. Examples of angle combinations for the most relevant ψ values for this transformation are shown in Table 6.2.

Table 6.2: Examples of angle combinations that provide the most relevant phase delay ψ values for the polarization transformation of a beam with $\mathbf{J}_{in} = (1,\ 1)^T$ into a beam with $\mathbf{J}_{out} = (1,\ e^{i\psi})^T$.

ψ (rad)	θ_H (rad)	θ_Q (rad)
0	$7\pi/4$	$5\pi/4$
$\pi/2$	0	0
π	$3\pi/2$	$5\pi/4$
$-\pi/2$	0	$-\pi/2$

Using two cascaded HWPs at angles $\theta_1 = \delta/2$ and $\theta_2 = 0$ rotates the polarization by an angle δ with respect to the input vector [245]. The Jones matrix of the resulting polarization rotator, i.e., $\underline{\mathbf{PR}}(\delta) = \underline{\mathbf{HWP}}(\delta/2)\underline{\mathbf{HWP}}(0)$, is

$$\underline{\mathbf{PR}}(\delta) = \begin{pmatrix} \cos\delta & -\sin\delta \\ \sin\delta & \cos\delta \end{pmatrix}. \tag{6.29}$$

This device can be adapted for a variety of purposes. For example, a radial-to-azimuthal polarization rotator is obtained by setting $\delta = \pi/2$, as depicted in Fig. 6.9. The order of the HWPs is inverted in Ref. [246], which adds a π phase to the resulting APB. Whilst this phase difference is not relevant in measurements, it may affect light manipulation. Using the polarization rotator with $\delta = \pi$ instead changes the handedness of an incident OC-ARPB.

Although the main focus in this section is on generating both configurations of the OC-ARPB for chirality probing and enantioseparation purposes, the setups depicted in Figure 6.7 and 6.8 can also be used to smoothly adjust the OAM density of the ARPB, either by varying the length L of the delay arm or the angles of the wave plates, which has practical applications in conducting OAM-related experiments.

6.7 Conclusion

We have investigated the properties of the ARPB and derived the analytical expressions for its field quantities. An in-phase superposition of an APB and an RPB results in an achiral ARPB. An out-of-phase superposition, however, results in a chiral ARPB with larger linear momentum and spin densities (both in terms of magnitude and number of components) than those of achiral beams. Moreover, a chiral ARPB carries a longitudinal OAM density despite having no azimuthal phase dependence, which can be continuously adjusted by varying the phase delay ψ between the APB and the RPB.

The ARPB can be *optimally chiral* and exhibits maximum linear momentum, angular momentum, and helicity densities. We have demonstrated that local circular polarization on the transverse plane is not a prerequisite for achieving optimal chirality. Indeed, optimal chirality is not merely a generalization of circularly polarized light; rather, it represents a broader concept, with CPL and the ARPB being specific subsets. It is particularly significant that, the transverse fields of the ARPB vanish on the beam axis, and therefore the same occurs to its linear and angular momentum densities, where only the energy and helicity densities associated with the longitudinal fields persist. Therefore, on its axis, the ARPB has a helicity density that stems solely from the longitudinal E_z and H_z field components. This feature can be used to probe the chirality of nanoparticles without caring about their geometrical anisotropy that leads to their electric or magnetic anisotropic polarizability.

We have shown that focusing an ARPB through a lens boosts its longitudinal fields more than the transverse ones, which results in an enhanced axial chirality density. Therefore, the ARPB provides a controlled environment that may be used to trap and probe chiral nanoparticles. Accordingly, the next step would be to calculate the photoinduced forces on a chiral dipolar particle illuminated by an ARPB with an emphasis on the optimally chiral configuration, similarly to what was done in Ref. [247] for a tightly-focused APB. To aid future research experiments, we have also provided the schematics for an optical setup that generates an ARPB and provided a polarization rotator that changes the handedness of an OC-ARPB.

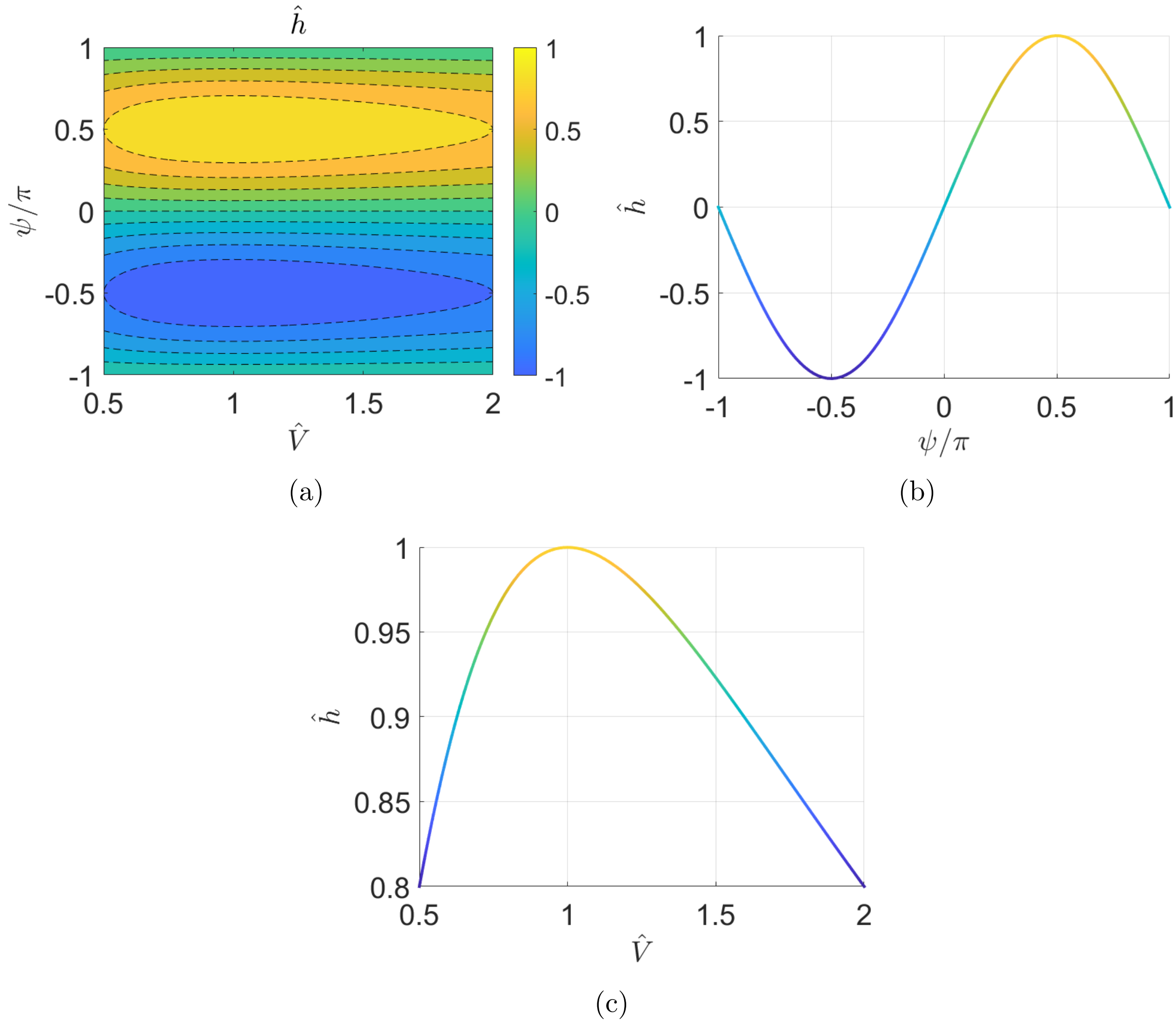

Figure 6.3: Normalized helicity density $\hat{h}$ of an ARPB in terms of $\hat{V}$ and ψ, calculated as $\hat{h} = hu/\omega$. (a) Colormap of $\hat{h}$ for $\hat{V} \in [0, 2]$ and $\psi \in [-\pi, \pi]$. The maximum magnitude for the normalized helicity density occurs for OC-ARPBs that is $V_A = \pm iV_R$. (b) The normalized helicity density for $\hat{V} = 1$ and $\psi \in [-\pi, \pi]$. The maximum values are found for $\psi = \pm\pi/2$. (c) The normalized helicity density for $\psi = \pi/2$ and $\hat{V} \in [0, 2]$. The magnitude of the normalized helicity density reaches unity ($\hat{h} = 1$) for $\hat{V} = 1$ and $\psi = \pm\pi/2$, i.e., $V_A = \pm iV_R$.

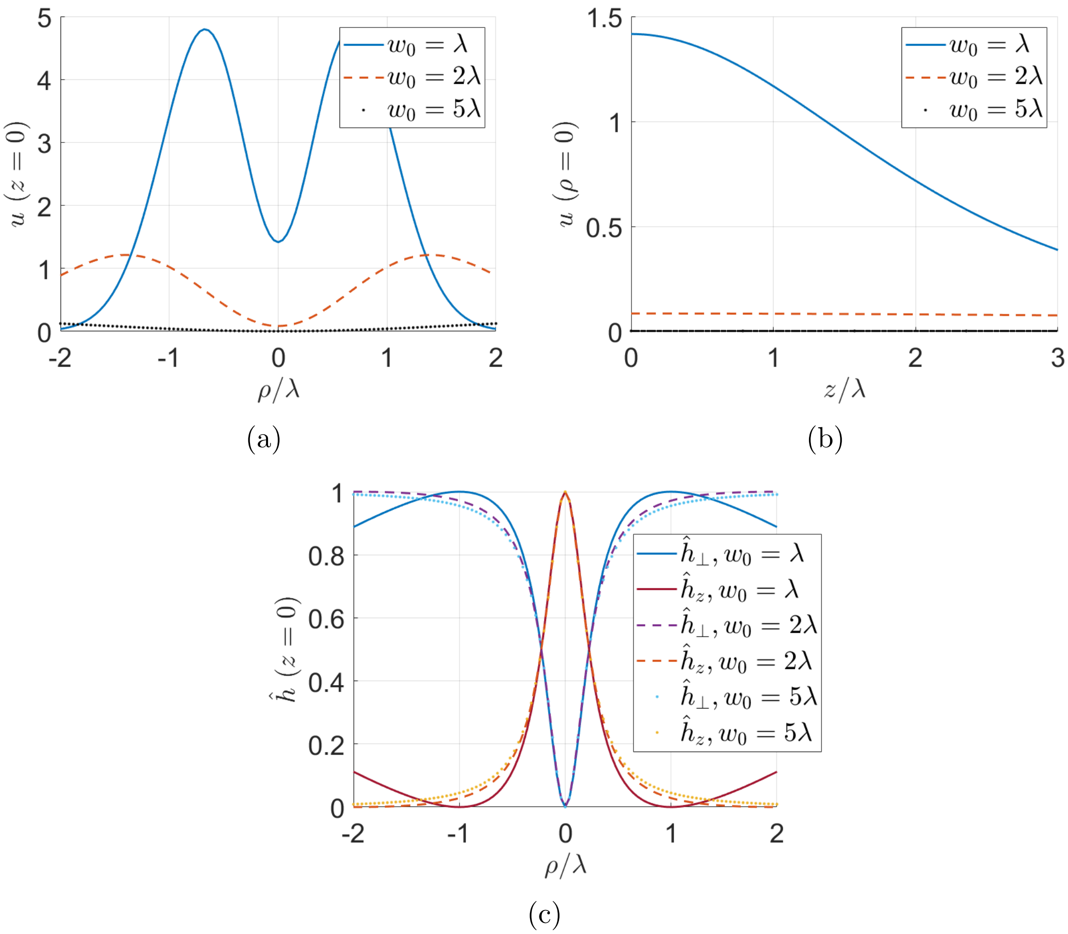

Figure 6.4: Comparison of the energy u and helicity h densities of an OC-ARPB (of 1 mW power) with $w_0 = \lambda$, $w_0 = 2\lambda$, and $w_0 = 5\lambda$. (a) Depicts the energy density at focus in the transverse plane and (b) shows the energy density on the beam axis. In both figures, the energy density increases as the ratio w_0/λ decreases. (c) Depicts the components of the normalized helicity density that stem from the transverse $\hat{h}_\perp$ and longitudinal $\hat{z}$ field components of the three OC-ARPB. Even though the focused ARPB has a higher helicity density, the region of space where it stems mostly due to the longitudinal field components remains approximately constant at $\rho \approx 0.225\lambda$.

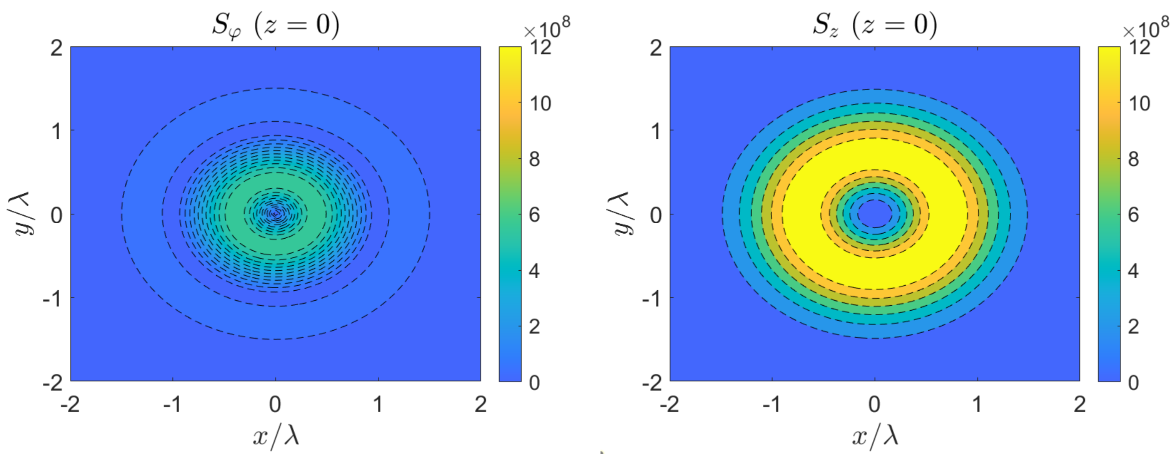

(a) (b)

Figure 6.5: Magnitudes of the (a) azimuthal and (b) longitudinal components of the Poynting vector $\mathbf{S}$ of an OC-ARPB (of 1 mW power at $\lambda = 400$ nm) in the transverse plane at the focus of the beam, i.e., $z = 0$. The radial component S_ρ has not been plotted since it is practically zero at the focus of the beam. The azimuthal component S_φ peaks in a small ring close to the beam axis, since it is associated with the radial and longitudinal fields. The longitudinal component S_z is the largest of them since it is only associated with the transverse fields, which are significantly larger than the longitudinal components. Due to azimuthal symmetry and vanishing transverse fields on the beam axis, the components of the Poynting vector describe an annular ring around it.

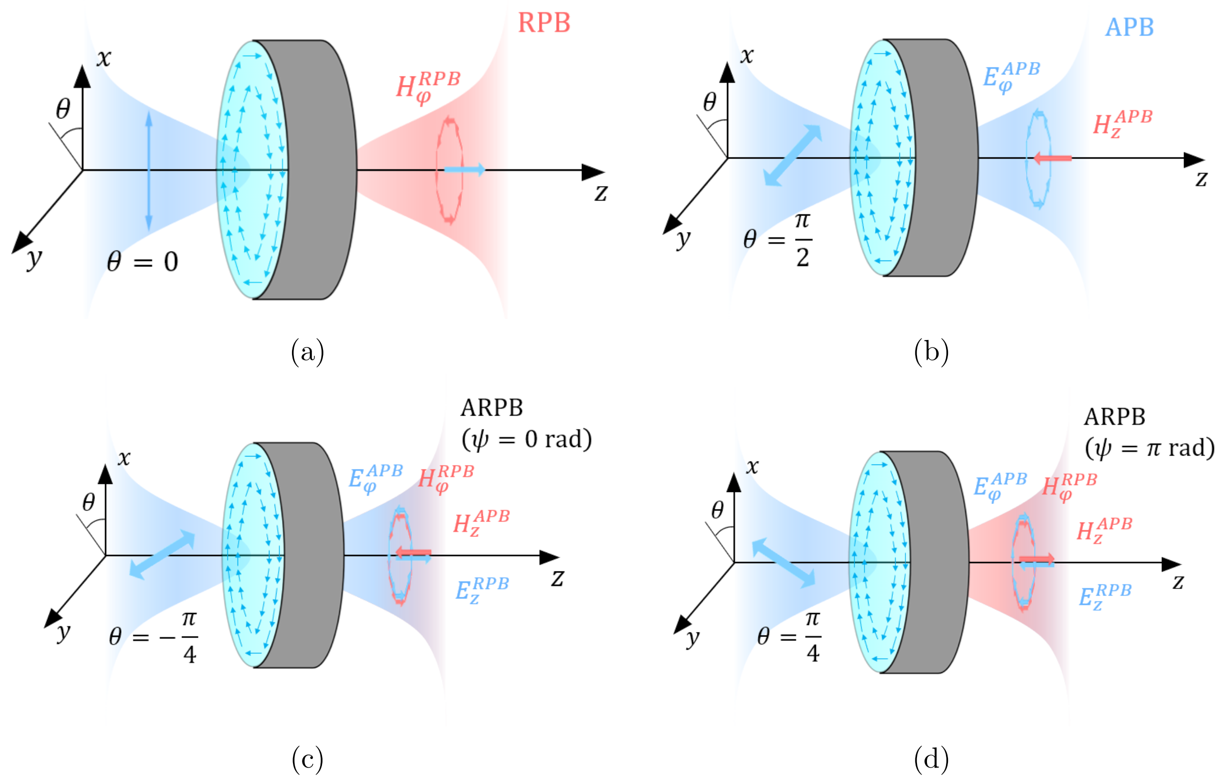

Figure 6.6: Schematic of a linearly polarized beam traveling through an SWP. (a) An x-polarized beam is transformed into an RPB. (b) An y-polarized beam is transformed into an APB. (c) A beam polarized at $\theta = -\pi/4$, with θ the angle between the x and y axis, is transformed into the sum of an RPB and an APB with the same phase. (d) A beam polarized at $\theta = \pi/4$ is transformed into a sum of an RPB and an APB with opposite phases.

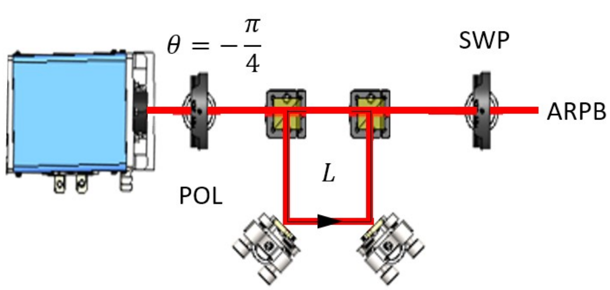

Figure 6.7: Optical setup to obtain an ARPB with $\hat{V} = 1$ and arbitrary ψ. The beam is polarized at an angle $\theta = -\pi/4$ with respect to the x-axis, and the y-component is added a phase-shift ψ using a delay arm of length L. The resulting beam travels through an SWP, resulting in the desired ARPB.

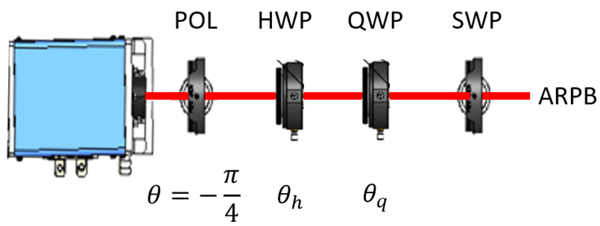

Figure 6.8: Optical setup to obtain an ARPB with $\hat{V} = 1$ and arbitrary ψ using a QWP and a HWP at angles θ_q and θ_h, respectively, instead of the delay arm from Figure 6.7. Possible angle combinations that provide the most relevant ψ values are shown in Table 6.2.

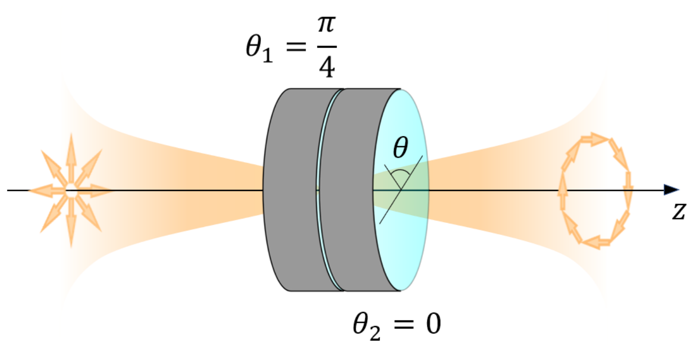

Figure 6.9: Schematic for a radial-to-azimuthal polarization rotator using two HWPs with an angle difference of $\theta_1 - \theta_2 = \pi/4$.

Chapter 7

Experimental Generation of Optimally Chiral Azimuthally-Radially Polarized Beams

In this chapter, we demonstrate the experimental generation and characterization of the optimally chiral ARPB using vectorial light shaping with dual spatial light modulators. We verify that the helicity density can be tuned across its full range by varying a single phase parameter and confirm that optimal chirality occurs even without circular polarization, validating the theoretical predictions under the paraxial approximation.

7.1 Introduction

Part of this study was inspired by the work of Prof. Federico Capasso, to whom this special issue is dedicated. The many topics Prof. Capasso worked on include helicity, chirality of light and the interaction with chiral matter, most notably in Refs. [223, 206, 189]. Some of the material of this paper was presented and discussed during the 2024 NanoPlasm Conference in Cetraro (IT) where Prof. Capasso's 75th birthday was celebrated.

The study of structured light is important for various applications, including the detection of chiral nanoparticles [223, 206, 189]. Chirality is a property of objects that are not superimposable with their mirror image [177]. Importantly, many biologically relevant molecules exist in chiral pairs, known as enantiomers [186]. Traditionally, the "handedness" of circularly polarized light has been associated with the chirality of light, but here we show that the chirality of light is much more general than the simple concept of handedness. The chiral nature of electromagnetic fields can be described using helicity density [69, 248, 222]. For monochromatic beams with the implicit time dependence $e^{-i\omega t}$, where ω is the angular frequency of light, the time-average helicity density is [190, 70, 71]

$$h = \frac{1}{2\omega c}\Im(\mathbf{E} \cdot \mathbf{H}^*), \tag{7.1}$$

where $\mathbf{E}$ and $\mathbf{H}$ represent the electric and magnetic field phasors of light, respectively. The term $c = 1/\sqrt{\varepsilon_0\mu_0}$ is the speed of light in vacuum.

In Ref. [70], it was shown that the magnitude of the helicity density of a monochromatic field, at a given time-average energy density $u = \varepsilon_0|\mathbf{E}|^2/4 + \mu_0|\mathbf{H}|^2/4$ [230], has an upper bound, i.e., $|h| \leq u/\omega$ always. Light fields that reach the upper bound $|h| = u/\omega$ are known as optimal chiral light (OCL). Circularly polarized light (CPL) is the most intuitive example of OCL [186], and the sign of h is related to the handedness of CPL. The same upper bound for the magnitude of the helicity density was stated in Ref. [249] involving fields whose Fourier spectrum representation contains only plane waves with one circular polarization. However, the concepts of helicity density and optimal chirality hold true for any kind of monochromatic structured light, including cases where the magnetic and electric fields are polarized along a single (e.g., the beam's longitudinal) direction, and the concept of handedness cannot be applied. The necessary and sufficient condition for fields to be locally optimally chiral is

$$\mathbf{E} = \pm i\eta_0 \mathbf{H}, \tag{7.2}$$

where $\eta_0 = \sqrt{\mu_0/\varepsilon_0}$ is the intrinsic impedance of free space [70]. This condition, referred to as the optimal chirality condition, stipulates that optimally chiral fields are those whose electric and magnetic field phasors have balanced magnitudes and a quarter-period phase delay between them. Fields that satisfy this condition also display a remarkable electric-magnetic symmetry in their energy and spin densities [70]. Under this optimal chirality condition, one has $h = \pm\mu_0|\mathbf{H}|^2/(2\omega) = \pm\varepsilon_0|\mathbf{E}|^2/(2\omega)$.

The concepts of optimal chirality and self-duality are equivalent for monochromatic beams. Self-duality refers to fields that are unchanged by the the duality transformation $\mathbf{E} \to \mathbf{B}$ and $\mathbf{B} \to -\mathbf{E}$ [249, 250]. These fields are eigenvectors of the curl [251], i.e., $\nabla \times \mathbf{E} = k\mathbf{E}$. As shown in Ref. [252] without connecting the concepts of optimal chirality and self-duality, monochromatic fields satisfying the optimal chirality condition from Eq. (7.2) are eigenvectors of the curl operator, and therefore self-dual fields. Here we use the concept of optimal chirality instead of self-duality because we focus on the chirality features of the beam, rather than on the broader electromagnetic symmetries displayed by self-dual beams.

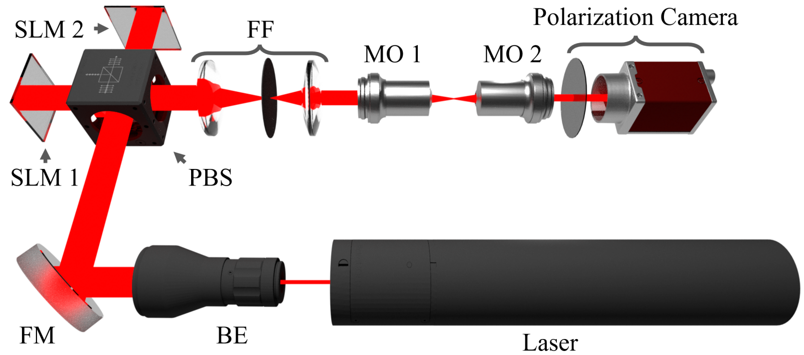

Figure 7.1: Diagram illustrating the experimental setup used to generate the ARPBs with variable ψ. A diagonally polarized He-Ne laser is first collimated and expanded by a beam expander (BE), then aligned by folding mirrors (FM) before vertical and horizontal polarizations are separated by a polarized beam splitter (PBS) onto two twin spatial light modulators (SLM1 and SLM2). Each SLM dynamically modulates the power and phase of the beam returning through the PBS. Separate calculated phases are applied to the orthogonally polarized beams before recombination at the PBS. The beam is then Fourier filtered (FF), and focused using a 0.25NA objective (MO 1). Polarization imaging is performed with a 0.85NA objective (MO 2) in the focal plane of the ARPB, which is captured using a Kiralux Polarization Camera. Updating the ARPB with a new value of ψ simply involves displaying holograms generated with the modified transverse electric field components on the SLMs.

Additionally, few self-dual fields seem to have been studied experimentally [253].

Optimally chiral structured beams are important because they combine two powerful effects: vectorially shaped light and maximized chirality density at a given energy density. This combination is advantageous because it allows for the control of enhanced interaction of the beam with chiral matter. As a result, optimally chiral structured beams open new possibilities for controlled sensing and manipulation of chiral particles. Moreover, the topology of tailored beams enables creative designs for chirality-discriminating optical traps [254], which aim at trapping an enantiomer while repelling its mirror image [255, 256, 257, 184, 71, 223].

The unprecedented control over the amplitude and phase of structured light [230, 258] also results in an exceptional ability to finely tune the helicity density h of a probing beam. This precise control allows one to tune the interaction between a chiral particle and an illuminating field by adjusting h [186] and it leads to a more detailed characterization of the interactions between the chiral sample and the fields, even beyond the commonly used dipolar approximation (the dipolar photoinduced chiral forces are described in Ref. [197]). The importance of higher-order multipoles on chiral interactions is investigated in Ref. [259]. Additionally, the control over the helicity density enables rapid changes in its sign (similar to reversing the "handedness" of circularly polarized light), facilitating the creation of dynamic optical potentials [260, 261] for enantioseparation and the experimental investigation of the chiral effects of higher-order multipoles.

However, the ability to generate optimally chiral structured beams is constrained. One must design an optical beam that satisfies the optimal chirality condition from Eq. (7.2) and effectively generate it. Here we implement a previously proposed example of a structured beam that displays optimal chirality: the azimuthally-radially polarized beam (ARPB) [72, 226, 70]. The ARPB consists of a phase-shifted combination of an azimuthally polarized beam and a radially polarized beam. It has been theoretically studied in the past, see Refs. [72, 70, 73, 74], and most comprehensively in Ref. [252]. The optimally chiral ARPB (OC-ARPB) combines the extraordinary properties of OCL with the spatial separation between its transverse fields, which vanish on the beam axis, and the longitudinal fields. OCL is present along the beam axis, solely due to E_z and H_z. Consequently, the ARPB has the potential to be used for controlled, on-axis separation of enantiomers or for enantiomer detection. The ARPB has also been recently studied in Refs. [215] and [262], without focusing on the chiral features of the ARPB.

Our work presents an experimental implementation of the ARPB, with a focus on characterizing its chirality and demonstrating its ability to achieve optimal chirality [70, 252]. By employing advanced vectorial shaping techniques, we have overcome limitations to the field's stability and local polarization control to successfully generate a paraxial APRB with precise manipulation over its features, validating theoretical predictions. Importantly, we show that the helicity density of the ARPB can be tuned across its full range of possible values by varying a single beam parameter. While our findings are confined to studying the chirality density in the transverse plane, they demonstrate the potential of optimally chiral structured light for designing enantioseparating optical traps and advancing practical schemes for the sensing and manipulation of chiral particles. Additionally, we show in Section 7.4 that if the transverse fields of a beam satisfy the optimal chirality condition from Eq. (7.2), the longitudinal fields satisfy it as well.

7.2 Methods

7.2.1 Helicity Density

The field phasors of the ARPB are [252]

$$\begin{aligned}\mathbf{E} &= \tfrac{fV}{kw^2}\left[k\rho\left(A_\rho + iB_\rho\right)\hat{\boldsymbol{\rho}} + k\rho\hat{V}e^{i\psi}\,\hat{\boldsymbol{\varphi}} + 2i\left(A_z + iB_z\right)\hat{\boldsymbol{z}}\right],\\ \mathbf{H} &= -\tfrac{fV}{kw^2\eta_0}\left[k\rho\hat{V}e^{i\psi}\left(A_\rho + iB_\rho\right)\hat{\boldsymbol{\rho}} - k\rho\,\hat{\boldsymbol{\varphi}} + 2i\hat{V}e^{i\psi}\left(A_z + iB_z\right)\hat{\boldsymbol{z}}\right],\end{aligned} \tag{7.3}$$

where V is a complex amplitude with units of Volts. The parameters $\hat{V}$ and ψ represent the relative amplitude and phase between the electric and magnetic azimuthal components, respectively, normalized by the characteristic impedance η_0. This relationship is expressed as $E_\varphi/(\eta_0 H_\varphi) = \hat{V}e^{i\psi}$. The dimensionless shorthand parameters f, A_ρ, B_ρ, A_z, and B_z are

$$
\begin{aligned}
f &= \tfrac{2}{\sqrt{\pi}} e^{-(\rho/w)^2 \zeta} e^{-2i\tan^{-1}(z/z_{\mathrm{R}})} e^{ikz}, \\
A_\rho &= 1 + \tfrac{1}{kz_R}\tfrac{\rho^2 - 2w_0^2}{w^2} + \left(\tfrac{2z\rho}{w^2 kz_R}\right)^2, \\
B_\rho &= -\tfrac{4}{(kw)^2}\tfrac{z}{z_R}\left(1 - \tfrac{\rho^2}{w^2}\right), \\
A_z &= 1 - \tfrac{\rho^2}{w^2}, \\
B_z &= \tfrac{z}{z_R}\tfrac{\rho^2}{w^2},
\end{aligned}
\tag{7.4}
$$

where w is the beam radius, defined as $w = w_0\sqrt{1 + (z/z_R)^2}$, and w_0 is defined as half the beam waist parameter at $z = 0$. The Gouy phase is $\zeta = 1 - iz/z_R$, and the Rayleigh range is denoted as $z_R = \pi w_0^2/\lambda$, where λ is the wavelength in free space. The wavenumber is $k = 2\pi/\lambda$. While f is a complex scalar, the other parameters A_ρ, B_ρ, A_z, and B_z in Eq. (7.4) are real valued.

Adjusting the phase-shift ψ (referred to as the phase parameter of the ARPB) and the relative amplitude $\hat{V}$ enables the creation of an ARPB that meets the optimal chirality condition described in Eq. (7.2). This specific configuration occurs for $\psi = \pm\pi/2$ and $\hat{V} = 1$ [70, 252]. Note that the OC-ARPB is a structured, monochromatic, and self-dual beam.

Most notably, the ARPB has transverse fields that vanish on the beam axis ($\rho = 0$), where the longitudinal fields persist [72, 70, 73, 74]. This spatial separation between the transverse and longitudinal components of the beam results in vanishing linear and angular momentum densities on the beam axis [252], where only the energy and helicity densities (u and h respectively) associated with the longitudinal fields persist. For the ARPB, the time-average energy and helicity densities across the entire beam are [252]

$$
\begin{aligned}
u &= u_0 D(1+\hat{V}^2)/2, \\
h &= h_0 D\hat{V}\sin\psi,
\end{aligned}
\tag{7.5}
$$

where

$$
D = (k\rho)^2\left(1 + A_\rho^2 + B_\rho^2\right) + 4\left(A_z^2 + B_z^2\right), \tag{7.6}
$$

and $u_0 = \frac{\varepsilon_0}{2k^2w^4}|f|^2|V|^2$ and $h_0 = \frac{\varepsilon_0}{2\omega k^2 w^4}|f|^2|V|^2$ are normalization constants with units of energy density (J/m^3) and helicity density (Ns/m^2), respectively. They are related as $h_0 = u_0/\omega$, leading to

$$
h = \frac{u}{\omega}\frac{2\hat{V}}{1+\hat{V}^2}\sin\psi. \tag{7.7}
$$

7.2.2 Vectorial Beam Shaping

The paraxial ARPB is produced experimentally using spatial light modulators (SLMs), which introduce a digitally controlled spatially variable phase shift $\phi(x, y)$ to an incident optical field. The pixelated liquid crystal cells in an SLM differentially delay the phase of incident fields according to the voltage applied over each pixel. The SLM is controlled via a desktop computer (Dell XPS). For a calculated scalar field E, the hologram is produced by mapping the required phase values to voltages applied over the SLM screen. Since these are typically

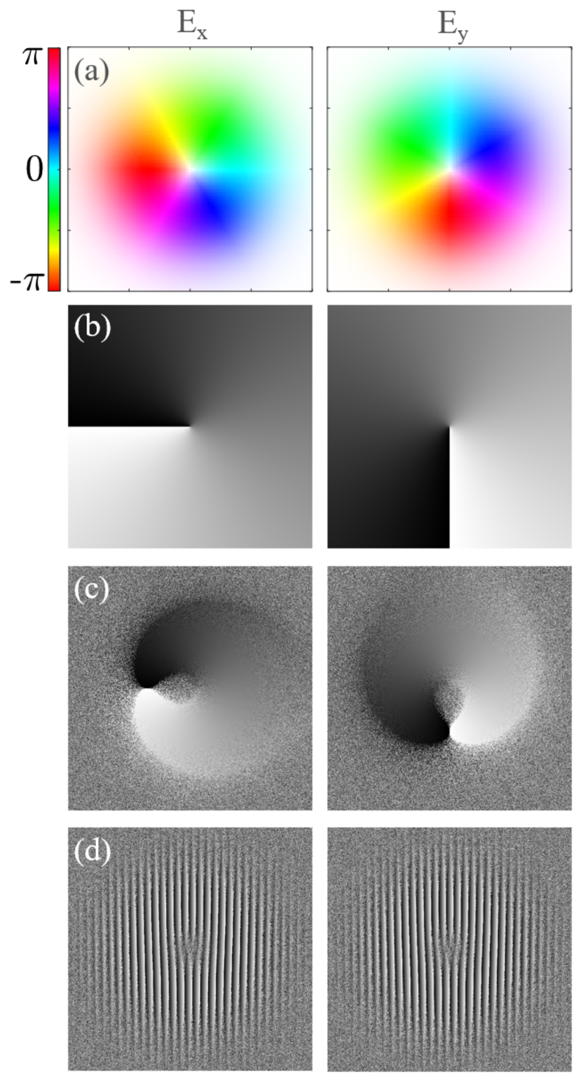

Figure 7.2: Hologram generation process at each step for the separate orthogonal polarization components of an ARPB with ψ =$\pi/2$: E_x(left), and E_y(right); (a) calculated phase and amplitude of ARPB components; (b) conversion of phase to grayscale; (c) addition of amplitude modulation; (d) addition of a Blazed grating. The final holograms (d) are displayed on the orthogonal SLMs to shape the beams immediately followed by recombination using a polarized beam splitter to create the final complex wave.

input into the SLM as 8-bit grayscale values, a pre-calibrated a lookup table is used to ensure a linear phase shift.

To ensure the desired wave function is accurately reproduced by the SLM, each phase we wish to imprint on a beam must be processed such that the desired phase and amplitude information are imparted to the beam while filtering unwanted intensity and diffraction orders. Although amplitude modulation is not directly available with a phase-only SLM, pseudo-amplitude modulation is possible. Amplitude modulation can be created using a scattering mask; The inverse amplitude, given by $1-|\mathbf{E}|^2/\max|\mathbf{E}|^2$, is multiplied by a matrix of random integers and then applied to the grayscale phase hologram (see Fig. 7.2 (c)). This modulation redistributes unwanted power into higher spatial frequency components in k-space (see Ref. [263] for details). It is pertinent to understand that the radially symmetric intensity profile appears asymmetric in Fig. 7.2 (c); however, this is only a visual artifact arising from the use of a noncyclical grayscale map that must be used when displaying holograms on an SLM. The perceived asymmetry is a result of phase differences at the edge of the range which roll over into the adjacent wavefront appearing high contrast, where the same difference away from the bounds appears relatively low contrast. Lastly, a blazed grating is applied (see Fig. 7.2 (d)) to tilt the shaped beam and preferentially directs power into the first-order diffraction spot [264]. The first order is then Fourier-filtered (FF), as shown in Figure 7.1, to eliminate non-diffracted light (in the zero order) and unwanted higher harmonics. Once set up, this holography process may remain static across all datasets and has a negligible impact on processing time.

Most commonly, SLMs are used to produce scalar waves with a constant polarization direction. Here, however, we use two SLMs to produce a vectorially shaped beam. The paraxial ARPB is generated using a twin SLM setup illustrated in Figure 7.1, initially introduced in Ref. [258] to generate obscured bottle beams. This method uses the twin SLMs to holographically control the beam's transverse field components, E_x and E_y, separately.

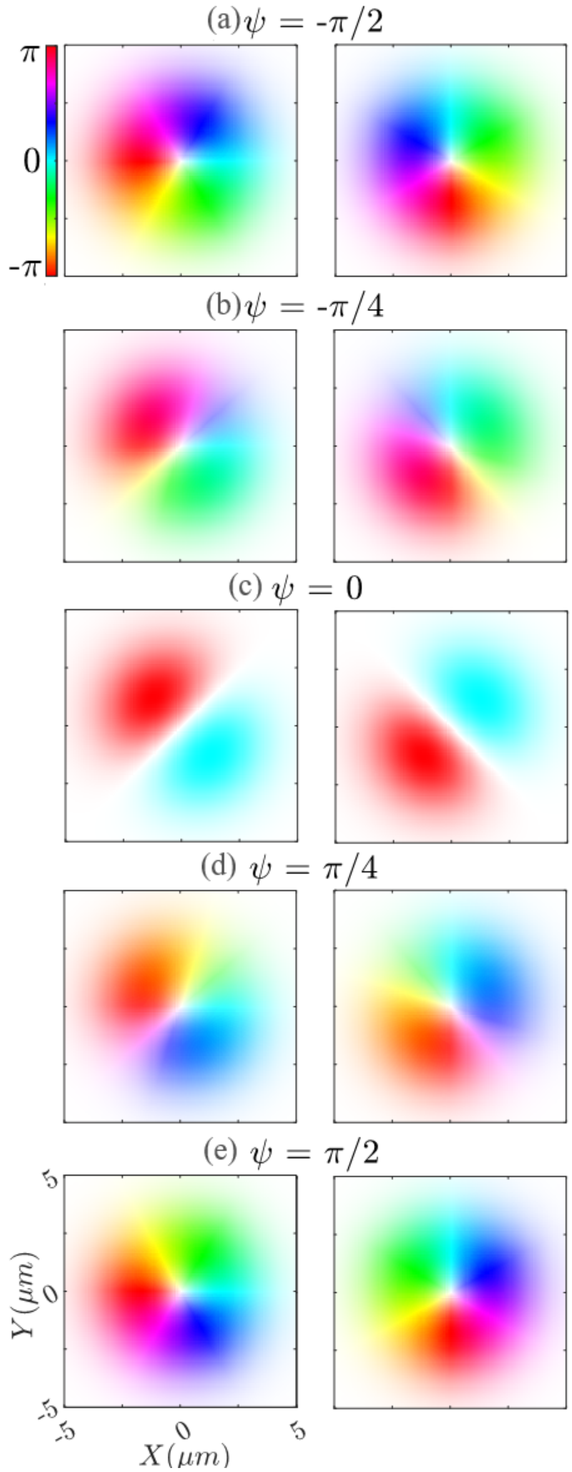

Figure 7.3: Calculated phase for the separate orthogonal polarization components of the ARPB for varying ψ values from $-\pi/2$ to $\pi/2$: E_x(left), and E_y(right). The color represents phase and saturation represents the intensity. Comparisons between phase values at a given point on an orthogonal pair reveal the resulting ellipticity upon combination.

To create such vectorially shaped beams, we first extract the complex field components of the corresponding Jones vector

$$\mathbf{E} = \begin{pmatrix} E_x \\ E_y \end{pmatrix} = \begin{pmatrix} |E_x|e^{i\phi_x} \\ |E_y|e^{i\phi_y} \end{pmatrix},$$

and then independently convert each component into a hologram. The phases of the E_x and E_y components of an ARPB with ψ ranging from $-\pi/2$ to $\pi/2$ are shown in the plots of Figure 7.3. Phases are processed into a hologram and displayed on two corresponding orthogonally aligned SLMs, which are aligned to match the polarization of the field component they display. The SLMs in this configuration provide control of phase and intensity of E_x and E_y individually, resulting in control of the local polarization state of the structured beam. The difference in amplitude modulation on each SLM rotates the orientation angle of the polarization according to $\arctan(|E_y|^2/|E_x|^2)$, while phase shifting ϕ_x relative to ϕ_y controls the ellipticity of the polarization state. The combination of these methods allows for local control of phase, amplitude, and polarization of the beam concurrently [265]. It is notable that to maintain system stability, a fixed optical path length must be preserved between each SLM. Although relative phase or position changes will not cause interference between the orthogonal field components, such changes can alter the outgoing polarization angle and ellipticity. Therefore, the system has been engineered to maximize rigidity.

In this paper, we produce five different paraxial ARPBs (which are assumed to have ($E_z = 0$) under the zeroth-order approximation [266]), with unity relative amplitude $\hat{V} = 1$ and a phase parameter ψ ranging from $-\pi/2$ to $\pi/2$. Generating or updating ARPBs with a new value of ψ simply involves processing holograms with the appropriate electric field components for display on the SLMs.

(a) $\psi = -\pi/2$ (b) $\psi = -\pi/4$ (c) $\psi = 0$ (d) $\psi = \pi/4$ (e) $\psi = \pi/2$

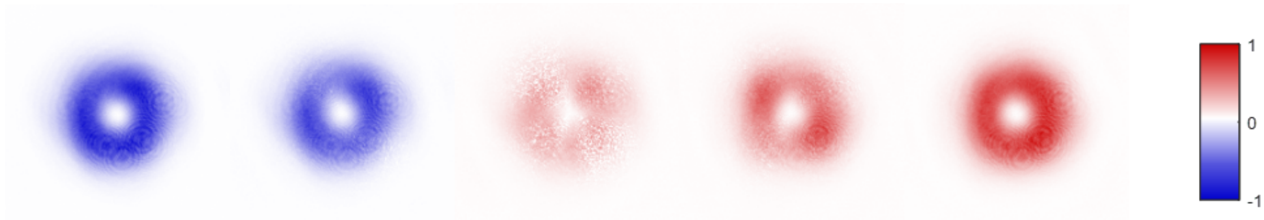

(f) $\psi = -\pi/2$ (g) $\psi = -\pi/4$ (h) $\psi = 0$ (i) $\psi = \pi/4$ (j) $\psi = \pi/2$

Figure 7.4: Predicted (above) and experimental (below) third normalized Stokes parameter s_3 on the transverse plane for ARPBs with $\psi = -\pi/2, -\pi/4, 0, \pi/4, \pi/2$ (and unity relative amplitude $\hat{V} = 1$). The first row, (a)-(e), displays theoretical S_3 at focus, while the second row, (f)-(j), presents the experimental results. As indicated by the colorbars on the right side of the figure, blue denotes a negative s_3, while red indicates a positive s_3. For the experimental results, the sign of $s_3 = \pm|s_3|$ has been chosen to better visually represent the change in the s_3 of an ARPB with ψ.

7.2.3 Helicity and Stokes Parameters

For each beam we simultaneously record the intensities I for the horizontal x, vertical y, diagonal d, and anti-diagonal a polarizations by using a polarization-sensitive camera (Thorlabs, Kiralux). These polarizations are at $0°, 90°, 45°, -45°$ with respect to the horizontal x axis, respectively. From the polarized intensity measurements we calculate the Stokes parameters S_0, S_1, and S_2 [267, 268], i.e.,

$$
\begin{aligned}
S_0 &= (I_x + I_y) = (I_d + I_a)\,, \\
S_1 &= (I_x - I_y)\,, \\
S_2 &= (I_d - I_a)\,.
\end{aligned}
\tag{7.8}
$$

The intensity is defined herein as the squared of the field amplitudes [269, 270], i.e., $I = |\mathbf{E}|^2$. Here we define the normalized Stokes parameters as $s_i = S_i/S_0$ for $i = 1, 2, 3$. For monochromatic beams, they are related as [271]

$$s_1^2 + s_2^3 + s_3^2 = 1, \tag{7.9}$$

where $S_3 = I_{LCP} - I_{RCP}$ is the difference between the intensity of left-handed and right-handed CPL, and $s_3 = S_3/S_0$. Therefore, we can extract the magnitude of the third normalized Stokes parameter $|s_3| = 1 - s_1^2 - s_2^3$ from linear polarization measurements. This normalized Stokes parameter is directly related to the helicity density of paraxial beams whose longitudinal fields are neglected (see Appendix A for details)

$$s_3 = h\omega/u. \tag{7.10}$$

The concept of optimal chirality states that the magnitude of the helicity density h for any kind of monochromatic structured light has the upper bound of u/ω, as demonstrated in Ref. [73]. Therefore, we find it convenient to use the concept of the normalized helicity density $\hat{h} = h\omega/u$, as in Ref. [252], whose value is bounded by $-1 \leq \hat{h} \leq 1$. We conclude that under the paraxial approximation, $s_3 = \hat{h}$, and that $|s_3| \leq 1$ is consistent with the concept of OCL that states that for any structured light $|\hat{h}| \leq 1$.

For the ARPB, the normalized helicity density is

$$\hat{h} = \frac{2\hat{V}}{1+\hat{V}^2}\sin\psi, \tag{7.11}$$

and when we use unity relative amplitude, $\hat{V} = 1$, we have $\hat{h} = \sin\psi$. In this work, we restrict our analysis to paraxial beams with negligible longitudinal fields, for which the normalized helicity density is equivalent to the third normalized Stokes parameters, $\hat{h} = s_3$. In Section 7.3, we will experimentally verify that $h = s_3 = \sin\psi$ for the paraxial ARPB. For non-paraxial beams, which have a helicity density with a contribution from the non-negligible longitudinal fields, $\hat{h} \neq s_3$.

7.3 Experimental Results

The main result presented herein is the characterization of the magnitude of the third normalized Stokes parameter $|s_3|$ of a paraxial ARPB with unity relative amplitude, $\hat{V} = 1$, and different values of the phase parameter ψ. The figures in Fig. 7.4 depict the predicted and experimental values of $|s_3|$ on the transverse plane for ARPBs with $\psi = -\pi/2, -\pi/4, 0, \pi/4, \pi/2$. The first row, (a)-(e), illustrates the theoretical s_3 of an ARPB at focus, while the second row, (f)-(j), presents its magnitude, $|s_3|$, calculated via experimental results. The colorbars on the right of the figures illustrate that blue represents a negative s_3 value, and red signifies a positive one. In the experimental data, the sign of s_3 is selected to more effectively display the variation in s_3 for an ARPB as ψ changes. The theoretical predictions display an annular ring around the beam center, with maximum absolute values for $\psi = \pm\pi/2$, and zero for $\psi = 0$. Intermediate values are observed for ARPBs with $\psi = \pm\pi/4$. The experimental results align consistently with the theoretical predictions, particularly for $\psi = \pm\pi/2$ and $\psi = \pm\pi/4$. Although we anticipated $|s_3|$ to be null across the transverse plane for an ARPB with $\psi = 0$, a residual $|s_3|$ is evident in experimental measurements, albeit at much lower intensities than those at $\psi = \pm\pi/4$. We speculate that this residue stems from the unwanted presence of small anisotropic effects within the optical setup shown in Fig. 7.1. These additional phase shifts between the x and y field components result in non-zero contributions to the third normalized Stokes parameter s_3.

To confirm that the measured residue for the $\psi = 0$ ARPB does not indicate a real chirality density in the transverse plane, we add a quarter-wave plate (QWP) with the fast axis on the horizontal (x) axis before the polarization camera in the setup from Figure 7.1. The QWP transforms left/right-handed circularly polarized light into anti/diagonally polarized light. Therefore, in the new analysis, the normalized helicity density of the paraxial ARPB is proportional to the second normalized Stokes parameter s_2 in the imaging plane. This behavior is depicted in Figure 7.5, which displays the measured s_2 after a quarter-wave plate (QWP) with the fast axis at 0° for an ARPB with $\psi = 0$. Indeed, it is shown in Figure 7.5 that $s_2 \approx 0$ on average, and that the residue shown in Fig. 7.4(h) is not indicative of a non-zero helicity density but rather of small anisotropic effects within the optical setup that distort the local polarization of the field. This notion is supported by the fact that the sign of the helicity density of the ARPB is independent of the position (ρ, φ, z) where it is evaluated, as shown in Eq. (7.7). The measured s_2 after the QWP (equivalent to s_3 without it), however, changes with the position where the field is measured. The ideal ARPB has azimuthal symmetry and the faint residual $|s_3|$, shown as s_2 after-QWP in Figure 7.5, does not display. This suggests the residual helicity is due to sub-wavelength curvature imbalance between the two SLMs.

Figure 7.6 illustrates the relationship between the normalized helicity density $\hat{h}$ and the phase parameter ψ of an ARPB with $\hat{V} = 1$. The theoretical values, represented by a black line, follow the sinusoidal dependence from Eq. (7.11). The calculated values of $|\hat{h}|$ are obtained by normalizing the experimental $|S_3|$ by their respective S_0 (as shown in Fig. 7.4), where the

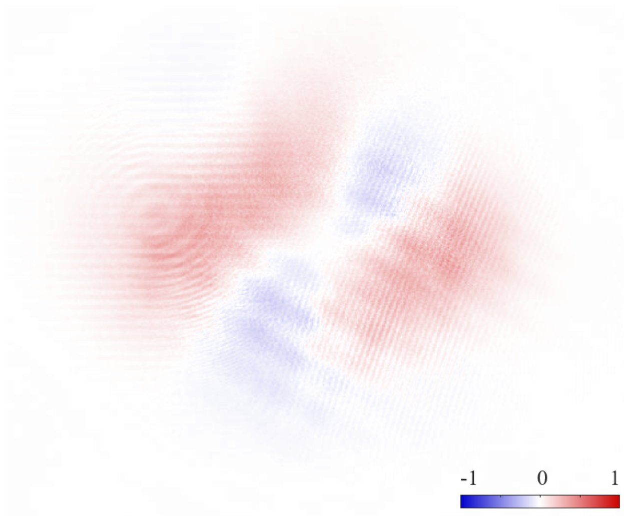

Figure 7.5: Second normalized Stokes parameters s_2 of an ARPB with $\hat{V} = 1$ and $\psi = 0$ after a QWP, equivalent to s_3 without the QWP. On average, $s_2 \approx 0$, confirming the lack of chirality of ARPBs with $\psi = 0$.

values of S_0 below a certain threshold are neglected to avoid division by zero outside of the beam.

The average of the resulting values of $|\hat{h}|$ is denoted by a blue circle, with vertical blue lines indicating the standard deviations of the filtered $|\hat{h}|$ for each value of ψ. In the figures presented, we depicted the quantity $\hat{h}$ (and equivalently s_3) under the assumption that we have knowledge of its sign. This assumption is made for illustrative purposes to visually represent the change in the normalized helicity density of the experimental ARPB with respect to the value of its phase parameter ψ.

The local polarization of structured light can be visualized using polarization textures where the angle and ellipticity of the electric field at a point are represented by projecting the arrows (normalized) pointing from the center of the Poincaré sphere to the direction of the respective polarization state on the Poincaré sphere. Linear polarization is represented as arrows fully in the x, y plane, circular polarization as arrows on the z axis (so only a dot is visible), and elliptical polarization is represented as arrows outside of the x, y plane (projected arrows are shorter than those representing linear polarization that have full length). These

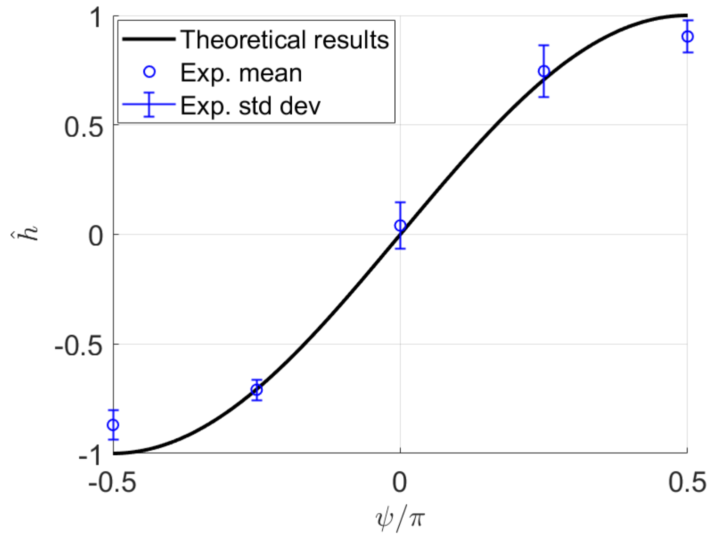

Figure 7.6: Normalized helicity density $\hat{h}$ plotted against phase parameter ψ for an ARPB with $\hat{V} = 1$. The black line shows theoretical values computed from Eq. (7.11), while the blue circles represent averaged experimental values, and the vertical blue lines indicate their standard deviations. The sign of the experimental s_3 has been included for illustrative purposes. Varying ψ it is possible to obtain any value of helicity density.

arrows are then plotted at various points in the transverse x, y plane of the beam, revealing the texture. The polarization textures of the implemented ARPBs are shown in Figure 7.7, with theoretical predictions on the left and experimental results on the right. The figures are organized in pairs with the same value of ψ enclosed in bordered boxes, and arranged vertically in increasing order of ψ, ranging from $-\pi/2$ to $\pi/2$. We observe that the theoretical OC-ARPBs with $\psi = \pm\pi/2$, (shown in the left of Figure 7.7(a) and (e)) exhibit local (left and right, respectively) circular polarization away from the beam edges. As the phase parameter ψ approaches zero, these chiral polarizations transition to linear polarizations. The lack of circularly polarized components for an ARPB with $\psi = 0$ is proof of its lack of chirality. Indeed, we see that the degree of circular polarization away from the center and edges of the beam reaches a maximum for ARPBs with $\psi = \pm\pi/2$, and a minimum for $\psi = 0$. These results reinforce the demonstration of optimally chiral structured light discussed in relation to Figures 7.4 and 7.6. By comparing the right and left columns in Figure 7.7, we can appreciate that the experimental results largely agree with the theoretical predictions, particularly away from the beam edges, where the experimental polarization textures show some variability.

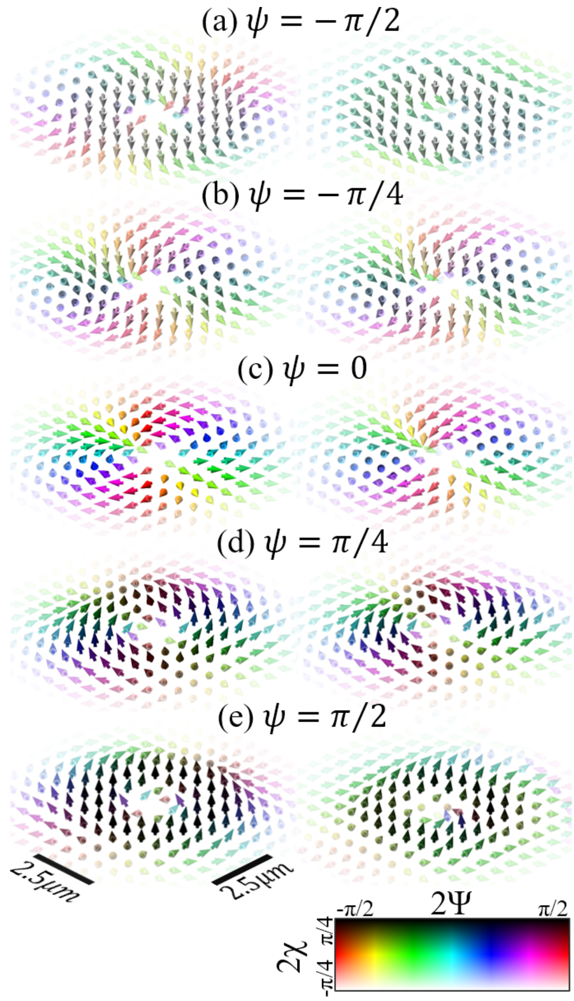

Figure 7.7: Theoretical (left) and experimental (right) polarization textures of the transverse electric fields at the focus of an ARPB varying the phase parameter ψ. The figures are arranged in order of increasing ψ from $-\pi/2$ to $\pi/2$. Arrow color represents local position on the Poincaré sphere according to polarization angle 2Ψ (not to be confused with phase parameter ψ seen throughout this paper) and ellipticity 2χ. By varying ψ is is possible to change the handedness of the ARPB's chirality, seen as the circularly polarized regions gradually flip from $2\chi = -\pi/4$ in (a), to $2\chi = \pi/4$ in (e).

7.4 Relevant properties of OCL

The results presented in the previous sections are important because they have demonstrated precise control over the helicity density of the ARPB by only tuning the phase parameter ψ. These investigations were conducted under the paraxial approximation [266]. Since the ratio w_0/λ is significantly larger than unity, the longitudinal fields are effectively smaller than the transverse ones in most of the transverse focal plane (see Ref. [207] for details). Furthermore, the measurement setup shown in Fig. 7.1 only distinguishes fields polarized in the transverse plane. Consequently, the excellent agreement between the theoretical and experimental normalized helicity densities shown in Section 7.3 further validates the use of the paraxial approximation and the neglecting of the longitudinal fields of an ARPB with a large beam waist parameter compared to the wavelength. Here, we expand on this aspect by showing that any field (it does not need to be a beam) that satisfies the optimal chirality condition from Eq. (7.2) in the *transverse* plane, i.e., $\mathbf{E}_\perp = \pm i\eta_0\mathbf{H}_\perp$, is a total OC field. To establish this, we use Maxwell's equations to derive the expressions for the longitudinal fields in terms of the transverse fields:

$$\begin{aligned} H_z &= \tfrac{-i}{\omega\mu_0}(\nabla \times \mathbf{E}_\perp)\cdot\mathbf{z}, \\ E_z &= \tfrac{i}{\omega\varepsilon_0}(\nabla \times \mathbf{H}_\perp)\cdot\mathbf{z}. \end{aligned} \tag{7.12}$$

Assuming the field exhibits optimal chirality in the transverse plane, i.e., $\mathbf{E}_\perp = \pm i\eta_0\mathbf{H}_\perp$, and substituting this relationship into Eq. (7.12), it follows that $E_z = \pm i\eta_0 H_z$. The longitudinal fields display the same magnitude ratio and phase shift between the electric and magnetic fields as the transverse fields. This calculation shows that optimal chirality in the transverse plane necessarily extends to the longitudinal direction as well.

For an ARPB, all field components display the same phase shift between the electric and magnetic fields regardless of whether it is optimally chiral. This is observed by following Ref. [252], where the helicity density was decomposed into its component contributions as $h = h_\rho + h_\varphi + h_z$, where each component is $h_n = \Im(E_n H_n^*)/(2\omega c)$, for $n = \rho, \varphi, z$. Specifically, for the ARPB we have

$$
\begin{aligned}
h_\rho &= h_0 (k\rho)^2 \left(A_\rho^2 + B_\rho^2\right) \hat{V} \sin\psi, \\
h_\varphi &= h_0 (k\rho)^2 \hat{V} \sin\psi, \\
h_z &= 4 h_0 \left(A_z^2 + B_z^2\right) \hat{V} \sin\psi.
\end{aligned}
\tag{7.13}
$$

The parameters A_ρ, A_z, B_ρ, B_z from Eq. (7.4) and $\hat{V}$ are real-valued, and therefore the sign of each helicity density component h_n is solely determined by the term $\sin\psi$. This means that for an ARPB, all components h_n share the same sign of helicity density, hence they all contribute constructively to having a specific helicity sign.

Additionally, optimally chiral structured light can be obtained without circular polarization, as it happens for a focused OC-ARPB [252]. Therefore, circular polarization is not a necessary condition for three-dimensional light to be optimally chiral.

Here, we further demonstrate that an optimally chiral beam under the paraxial approximation is necessarily circularly polarized. This latter statement is demonstrated by combining the optimal chirality condition, $\mathbf{E} = \pm i\eta_0 \mathbf{H}$, with the Faraday equation, leading to

$$
\nabla \times \mathbf{E} = \pm k \mathbf{E}, \tag{7.14}
$$

which is a necessary and sufficient condition to having optimal chiral light [252]. Eq. (7.14) shows that optimally chiral light has fields that are eigenvectors of the curl operator [253]. Therefore, monochromatic optimally chiral beams are self-dual [251].

For a three-dimensional field, using cartesian coordinates, i.e., $\mathbf{E} = E_x\hat{\mathbf{x}} + E_y\hat{\mathbf{y}} + E_z\hat{\mathbf{z}}$, we have

$$\begin{aligned} &\tfrac{\partial E_z}{\partial y} - \tfrac{\partial E_y}{\partial z} = \pm k E_x, \\ &\tfrac{\partial E_x}{\partial z} - \tfrac{\partial E_z}{\partial x} = \pm k E_y, \\ &\tfrac{\partial E_y}{\partial x} - \tfrac{\partial E_x}{\partial y} = \pm k E_z. \end{aligned} \tag{7.15}$$

Under the paraxial approximation, $\frac{\partial}{\partial z} >> \frac{\partial}{\partial y}, \frac{\partial}{\partial y}$ [272] (where the authors show the phase variation along an axis in terms of the wavenumber), and assuming that the field propagates along z as $\mathbf{E} \propto e^{ikz}$, the equations in Eq. (7.15) are simplified to

$$\begin{aligned} &-ikE_y = \pm k E_x, \\ &ikE_x = \pm k E_y, \\ &|E_z|/|\mathbf{E}_\perp| << 1, \end{aligned} \tag{7.16}$$

implying that the field is circularly polarized, i.e., $E_y = \pm i E_x$, wherein the two transverse components have equal magnitudes and a $\pi/2$ phase delay between them. Analogous proof holds for the transverse magnetic field that is also circularly polarized. For paraxial fields whose longitudinal fields are negligible compared to the transverse field components (for intermediate radial distance from the beam axis), the concept of optimally chiral light is equivalent to that of circular polarization on the focal plane, and only for intermediate radial distance as discussed for the ARPB in the next section. However, upon the introduction of structured light with considerable longitudinal fields, optimal chirality can be obtained without circular polarization.

7.5 Discussion

The presented results not only provide the first experimental analysis and confirmation of the realizability of an optimally chiral structured beam, the OC-ARPB, but also contribute to the limited experimental investigations of self-dual fields. While the primary focus of this paper is not on self-duality, our work aligns with observations in Ref. [253], where monochromatic self-dual electromagnetic fields are identified as eigenvectors of the curl operator.

The experiments described in this work demonstrate precise control over the helicity density of the ARPB via the tuning of the phase parameter ψ, following the relation $\hat{h} = \sin\psi$ when $\hat{V} = 1$. Therefore, we have shown that the helicity density of the ARPB can be tuned across its full range of possible values, namely, $-u/\omega \leq h \leq u/\omega$, by only varying the single beam parameter ψ (with $\hat{V} = 1$). Modifying other beam parameters, such as w_0 and λ, shapes the topology of the beam instead. For example, reducing the w_0/λ ratio leads to higher energy and helicity densities at the beam focus ($z = 0$), as shown in Ref. [252].

Additionally, we have been able to verify the local polarization of the paraxial ARPBs on the transverse plane with the polarization textures shown in Figure 7.7. The paraxial OC-ARPBs (i.e., when $\psi = \pm\pi/2$ and $\hat{V} = 1$) exhibit the highest degree of local circular polarization. The experimental results are in agreement with what was discussed after Eq. (20) in Ref. [252] that paraxial OC-ARPBs are primarily circularly polarized at the beam focal plane $z = 0$. The transverse fields of an OC-ARPB are

$$
\begin{aligned}
\mathbf{E}_\perp = \tfrac{\rho}{w^2} f V \left[(A_\rho + i B_\rho)\, \hat{\boldsymbol{\rho}} \pm i\, \hat{\boldsymbol{\varphi}} \right], \\
\mathbf{H}_\perp = \mp i \mathbf{E}_\perp / \eta_0.
\end{aligned}
\tag{7.17}
$$

Here, we further observe from Eq. (7.4) that for OC-ARPBs with a large waist relative to the wavelength ($w_0 \gg \lambda$) on the focal plane $z = 0$, one has $A_\rho \approx 1$ and $B_\rho = 0$, resulting in circular polarization in the transverse plane. Note that however when $\rho \gg w_0$, then A_ρ is not close to unity anymore. Therefore we do not have circular polarization at the edges of the beam, as shown in Figure 7.7 in both theory and experiment.

Additionally, the transverse circular polarization of paraxial OC-ARPB is also lost near the beam axis. This result is appreciated in Figure 7.7(a), where the local polarization of the theoretical OC-ARPB becomes elliptical near the beam axis. When $\rho \ll w_0$, the longitudinal fields cannot be neglected. This occurs when the term A_z is no longer much less than $k\rho A_\rho$ at $z = 0$. Consequently, near the beam axis $\hat{h} \neq s_3$, in agreement with the property of structured OC fields displaying optimal chirality ($|\hat{h}| = 1$) without being circularly polarized ($|s_3| = 1$). This result is consistent with the discussion in Ref. [251] stating that transversely finite beams which are circularly polarized everywhere in a fixed plane do not exist.

In summary, while circular polarization is a sufficient condition to attain optimal chirality, it is not a necessary one since a *focused* OC-ARPB displays optimal chirality without circular polarization. Even when the OC-ARPB has a large beam waist ($w_0 \gg \lambda$), it still displays optimal chirality without circular polarization near the axis and far away from it.

Our investigation has directly verified the optimal chirality of the paraxial OC-ARPB with $\hat{V} = 1$ and $\psi = \pm\pi/2$ only in the transverse plane, and at distances that are not near the axis nor far away from it. Even though our setup, illustrated in Figure 7.1, cannot differentiate the longitudinal components of light, the OC features of E_z and H_z have been theoretically demonstrated by using Maxwell's equations. The ARPB is expected to show exceptional promise in the control and manipulation of chiral molecules in the Rayleigh regime, where the size of the particle is significantly smaller than the beam's wavelength. This regime is well characterized in the context of electromagnetic scattering [273]. Subwavelength-sized particles can be trapped in the region surrounding the beam axis where the longitudinal fields dominate. In that region, the energy and helicity densities dominate over the linear and angular momentum densities as discussed in Ref. [252], leading to enhanced control over the forces exerted on dipolar chiral molecules. The photoinduced forces exerted on chiral dipolar particles from structured light fields are described in Ref. [197].Since the ARPB offers promising avenues for precise probing and manipulation of chiral particles, future research will explore the optical helicity of non-paraxial ARPBs that display strong longitudinal fields on the beam axis.

7.6 Conclusion

We have successfully generated an ARPB using a versatile optical setup with two SLMs employing orthogonal polarizations (x and y). By adjusting the phase parameter ψ, we demonstrated the ability to manipulate the chirality density of the ARPB across its full range of possible values. Notably, we found that the paraxial ARPB can achieve optimal chirality for $\psi = \pm\pi/2$, showcasing the existence of optimally chiral structured light.

While the experiments realized herein are restricted to the transverse plane, we have also theoretically shown that three-dimensional fields whose transverse components satisfy the optimal chirality condition are optimally chiral in all directions. Additionally, we have demonstrated that circular polarization is a sufficient but not necessary condition for structured fields to be optimally chiral, and that it is equivalent to the concept of optimal chirality only under the paraxial approximation and when the longitudinal fields are negligible compared to the transverse field components. We found that the local polarization of the OC-ARPB is circular away from the center or edges of the beam. In those regions, the local circular polarization is lost even though optimal chirality is maintained.

Additionally, we have shown that monochromatic optimally chiral fields are self-dual since their electric and magnetic fields are the eigenvectors of the curl operator, leading to maximal chirality density among other self-dual electromagnetic features. The OC-ARPB generated in this work represents an example of a structured self-dual monochromatic beam, of which few have been studied experimentally.

Importantly, the results of this study verify the first practical implementation of an OC structured beam, of which the OC-ARPB is only a specific example. This new tool provides unprecedented control over fundamental chiral light-matter interactions, with future applications of enhanced sensing and manipulation of chiral particles. Given the ubiquity and importance of chirality in biology, the development of precise tools to characterize and control chiral molecules is of supreme importance in the field of biophotonics and single-isomer drug discovery. The ability to dynamically control the helicity density of the ARPB allows for the innovative design of dynamic, enantioselective optical traps. Considering the importance of the polarization of the chiral field components on light-matter interactions, future research might explore chirality of non-paraxial ARPBs on the beam axis, which is solely attributed to the chiral longitudinal fields.

Bibliography

[1] Albert Herrero-Parareda, Ilya Vitebskiy, Jacob Scheuer, and Filippo Capolino. Frozen mode in an asymmetric serpentine optical waveguide. *Advanced Photonics Research*, page 2100377, 2021.

[2] Mohamed Y. Nada, Tarek Mealy, Md. Shafiqul Islam, Ilya Vitebskiy, Ricky Gibson, Robert Bedford, Ozdal Boyraz, and Filippo Capolino. Design of a modified coupled resonators optical waveguide supporting a frozen mode. *arXiv:2211.01408*, Nov 2022.

[3] Alex Figotin and Ilya Vitebskiy. Slow light in photonic crystals. *Waves in Random and Complex Media*, 16(3):293–382, 2006.

[4] Alex Figotin and Ilya Vitebskiy. Slow wave phenomena in photonic crystals. *Laser & Photonics Reviews*, 5(2):201–213, MAR 2011.

[5] Mohamed Y. Nada, Mohamed A. K. Othman, and Filippo Capolino. Theory of coupled resonator optical waveguides exhibiting high-order exceptional points of degeneracy. *Physical Review B*, 96(18):184304, NOV 22 2017.

[6] Dmitry Oshmarin, Farshad Yazdi, Mohamed A.K. Othman, Jeff Sloan, Mohammad Radfar, Michael M. Green, and Filippo Capolino. New oscillator concept based on band edge degeneracy in lumped double-ladder circuits. *IET Circuits, Devices and Systems*, 13(7):950–957, jul 2019, doi: 10.1049/iet-cds.2018.5048.

[7] Ahmed F Abdelshafy, Dmitry Oshmarin, Mohamed AK Othman, Michael M Green, and Filippo Capolino. Distributed degenerate band edge oscillator. *IEEE Transactions on Antennas and Propagation*, 69(3):1821–1824, 2020.

[8] Dmitry Oshmarin, Ahmed F Abdelshafy, Alireza Nikzamir, Michael M Green, and Filippo Capolino. Experimental demonstration of a new oscillator concept based on degenerate band edge in microstrip circuit. *arXiv:2109.07002*, 2021.

[9] Mohamed AK Othman, Mehdi Veysi, Alexander Figotin, and Filippo Capolino. Low starting electron beam current in degenerate band edge oscillators. *IEEE Transactions on Plasma Science*, 44(6):918–929, 2016.

[10] Ahmed F Abdelshafy, Mohamed AK Othman, Farshad Yazdi, Mehdi Veysi, Alexander Figotin, and Filippo Capolino. Electron-beam-driven devices with synchronous multi-

ple degenerate eigenmodes. *IEEE Transactions on Plasma Science*, 46(8):3126–3138, 2018.

[11] Banaful Paul, Niru K Nahar, and Kubilay Sertel. Frozen mode in coupled silicon ridge waveguides for optical true time delay applications. *JOSA B*, 38(5):1435–1441, 2021.

[12] John L Volakis and Kubilay Sertel. Narrowband and wideband metamaterial antennas based on degenerate band edge and magnetic photonic crystals. *Proceedings of the IEEE*, 99(10):1732–1745, 2011.

[13] Venkata Ananth Tamma, Alexander Figotin, and Filippo Capolino. Concept for pulse compression device using structured spatial energy distribution. *IEEE Transactions on Microwave Theory and Techniques*, 64(3):742–755, 2016.

[14] Mohamed AK Othman, Farshad Yazdi, Alex Figotin, and Filippo Capolino. Giant gain enhancement in photonic crystals with a degenerate band edge. *Physical Review B*, 93(2):024301, 2016.

[15] Hamidreza Ramezani, S Kalish, I Vitebskiy, and Tsampikos Kottos. Unidirectional lasing emerging from frozen light in nonreciprocal cavities. *Physical Review Letters*, 112(4):043904, 2014.

[16] Mehdi Veysi, Mohamed AK Othman, Alexander Figotin, and Filippo Capolino. Degenerate band edge laser. *Physical Review B*, 97(19):195107, 2018.

[17] Alex Figotin and Ilya Vitebskiy. Frozen light in photonic crystals with degenerate band edge. *Physical Review E*, 74(6, 2):066613, Dec 2006.

[18] Mohamed A. K. Othman and Filippo Capolino. Theory of exceptional points of degeneracy in uniform coupled waveguides and balance of gain and loss. *IEEE Trans. Antennas Propag.*, 65(10):5289–5302, OCT 2017.

[19] Ahmed F. Abdelshafy, Mohamed A. K. Othman, Dmitry Oshmarin, Ahmad T. Almutawa, and Filippo Capolino. Exceptional points of degeneracy in periodic coupled waveguides and the interplay of gain and radiation loss: Theoretical and experimental demonstration. *IEEE Trans. Antennas Propag.*, 67(11):6909–6923, Nov 2019.

[20] M I Vishik and L A Lyusternik. The solution of some perturbation problems for matrices and selfadjoint or non-selfadjoint differential equations i. *Russian Mathematical Surveys*, 15(3):1–73, jun 1960, doi: 10.1070/rm1960v015n03abeh004092.

[21] P. Lancaster. On eigenvalues of matrices dependent on a parameter. *Numerische Mathematik*, 6(1):377–387, dec 1964, doi: 10.1007/bf01386087.

[22] Alexander P. Seyranian. Sensitivity analysis of multiple eigenvalues. *Journal of Structural Mechanics*, 21(2):261–284, jan 1993, doi: 10.1080/08905459308905189.

[23] Tosio Kato. *Perturbation Theory for Linear Operators*. Springer-Verlag New York Inc., New York, 1966, doi: 10.1007/978-3-662-12678-3.

[24] Michael V Berry. Physics of nonhermitian degeneracies. *Czechoslovak Journal of Physics*, 54(10):1039–1047, 2004.

[25] Carl M Bender and Stefan Boettcher. Real spectra in non-Hermitian Hamiltonians having PT symmetry. *Physical Review Letters*, 80(24):5243, 1998.

[26] Carl M Bender. Making sense of non-hermitian hamiltonians. *Reports on Progress in Physics*, 70(6):947, 2007.

[27] Ali Mostafazadeh. Exact pt-symmetry is equivalent to hermiticity. *Journal of Physics A: Mathematical and General*, 36(25):7081, 2003.

[28] Viktar S Asadchy, Mohammad Sajjad Mirmoosa, Ana Díaz-Rubio, Shanhui Fan, and Sergei A Tretyakov. Tutorial on electromagnetic nonreciprocity and its origins. *Proceedings of the IEEE*, 108(10):1684–1727, 2020.

[29] A Ruschhaupt, F Delgado, and JG Muga. Physical realization of-symmetric potential scattering in a planar slab waveguide. *Journal of Physics A: Mathematical and General*, 38(9):L171, 2005.

[30] R El-Ganainy, KG Makris, DN Christodoulides, and Ziad H Musslimani. Theory of coupled optical PT-symmetric structures. *Optics Letters*, 32(17):2632–2634, 2007.

[31] A Guo, GJ Salamo, D Duchesne, R Morandotti, M Volatier-Ravat, V Aimez, GA Siviloglou, and DN Christodoulides. Observation of PT symmetry breaking in complex optical potentials. *Physical Review Letters*, 103(9):093902, 2009.

[32] Mohamed AK Othman, Vincenzo Galdi, and Filippo Capolino. Exceptional points of degeneracy and p t symmetry in photonic coupled chains of scatterers. *Physical Review B*, 95(10):104305, 2017.

[33] R. Seydel. *Practical Bifurcation and Stability Analysis*. Springer-Verlag New York Inc., New York, 1994.

[34] David G Schaeffer and Ian Stewart. *Singularities and groups in bifurcation theory*. Berlin, Germany: Springer-Verlag, 1985.

[35] E Hernández, A Jáuregui, A Mondragón, and L Nellen. Degeneracy of resonances: Branch point and branch cuts in parameter space. *International Journal of Theoretical Physics*, 46(6):1666–1701, 2007.

[36] E Hernández, A Jáuregui, and A Mondragón. Exceptional points and non-hermitian degeneracy of resonances in a two-channel model. *Physical Review E*, 84(4):046209, 2011.

[37] Alexander B Yakovlev and George W Hanson. On the nature of critical points in leakage regimes of a conductor-backed coplanar strip line. *IEEE Transactions on Microwave Theory and Techniques*, 45(1):87–94, 1997.

[38] George W Hanson and Alexander B Yakovlev. An analysis of leaky-wave dispersion phenomena in the vicinity of cutoff using complex frequency plane singularities. *Radio Science*, 33(4):803–819, 1998.

[39] Alexander B Yakovlev and George W Hanson. Analysis of mode coupling on guided-wave structures using morse critical points. *IEEE Transactions on Microwave Theory and Techniques*, 46(7):966–974, 1998.

[40] Alexander B Yakovlev and George W Hanson. Fundamental modal phenomena on isotropic and anisotropic planar slab dielectric waveguides. *IEEE Transactions on Antennas and Propagation*, 51(4):888–897, 2003.

[41] George W Hanson, Alexander B Yakovlev, Mohamed AK Othman, and Filippo Capolino. Exceptional points of degeneracy and branch points for coupled transmission lines—Linear-algebra and bifurcation theory perspectives. *IEEE Transactions on Antennas and Propagation*, 67(2):1025–1034, 2019.

[42] Tarek Mealy, Ahmed F. Abdelshafy, and Filippo Capolino. The degeneracy of the dominant mode in rectangular waveguide. In *Proceedings USNC/URSI National Radio Science Meeting*. Boulder, Colorado, USA, Jan. 2019.

[43] Alexander Figotin and Ilya Vitebskiy. Electromagnetic unidirectionality in magnetic photonic crystals. *Physical Review B*, 67(16):165210, 2003.

[44] Alex Figotin and Ilya Vitebskiy. Slow light in photonic crystals. *Waves in Random and Complex Media*, 16(3):293–382, 2006.

[45] Alex Figotin and Ilya Vitebskiy. Slow wave phenomena in photonic crystals. *Laser & Photonics Reviews*, 5(2):201–213, 2011.

[46] Mohamed Y. Nada, Tarek Mealy, and Filippo Capolino. Frozen mode in three-way periodic microstrip coupled waveguide. *IEEE Microwave and Wireless Components Letters*, 31(3):229–232, MAR 2021.

[47] Nadav Gutman, C. Martijn de Sterke, Andrey A. Sukhorukov, and Lindsay C. Botten. Slow and frozen light in optical waveguides with multiple gratings: Degenerate band edges and stationary inflection points. *Physical Review A*, 85(3):033804, MAR 7 2012.

[48] Alex Figotin and Ilya Vitebskiy. *Electromagnetic Unidirectionality in Magnetic Photonic Crystals*, pages 35–50. Springer Berlin Heidelberg, Berlin, Heidelberg, 2013.

[49] Huanan Li, Ilya Vitebskiy, and Tsampikos Kottos. Frozen mode regime in finite periodic structures. *Phys. Rev. B*, 96(18):180301, Nov 8 2017.

[50] Matthew B Stephanson, Kubilay Sertel, and John L Volakis. Frozen modes in coupled microstrip lines printed on ferromagnetic substrates. *IEEE Microwave and Wireless Components Letters*, 18(5):305–307, 2008.

[51] Gokhan Mumcu, Kubilay Sertel, and John L Volakis. Lumped circuit models for degenerate band edge and magnetic photonic crystals. *IEEE Microwave and Wireless Components Letters*, 20(1):4–6, 2009.

[52] Mohamed Y Nada, Tarek Mealy, and Filippo Capolino. Frozen mode in three-way periodic microstrip coupled waveguide. *IEEE Microwave and Wireless Components Letters*, 31(3):229–232, 2020.

[53] Mohamed Y Nada, Mohamed AK Othman, and Filippo Capolino. Theory of coupled resonator optical waveguides exhibiting high-order exceptional points of degeneracy. *Physical Review B*, 96(18):184304, 2017.

[54] Raed Almhmadi and Kubilay Sertel. Frozen-light modes in 3-way coupled silicon ridge waveguides. In *2019 United States National Committee of URSI National Radio Science Meeting (USNC-URSI NRSM)*, pages 1–2, Boulder, CO, USA, 2019.

[55] Mohamed AK Othman, Xuyuan Pan, Georgios Atmatzakis, Christos G Christodoulou, and Filippo Capolino. Experimental demonstration of degenerate band edge in metallic periodically loaded circular waveguide. *IEEE Transactions on Microwave Theory and Techniques*, 65(11):4037–4045, 2017.

[56] Ahmed F Abdelshafy, Mohamed AK Othman, Dmitry Oshmarin, Ahmad T Almutawa, and Filippo Capolino. Exceptional points of degeneracy in periodic coupled waveguides and the interplay of gain and radiation loss: Theoretical and experimental demonstration. *IEEE Transactions on Antennas and Propagation*, 67(11):6909–6923, 2019.

[57] Tarek Mealy and Filippo Capolino. General conditions to realize exceptional points of degeneracy in two uniform coupled transmission lines. *IEEE Transactions on Microwave Theory and Techniques*, 68(8):3342–3354, 2020.

[58] Justin R. Burr, Michael G. Wood, and Ronald M. Reano. Experimental verification of degenerate band edge dispersion in silicon photonic integrated circuits. *IEEE Photonics Journal*, 8(6):1–10, 2016.

[59] Lars H Frandsen, Andrei V Lavrinenko, Jacob Fage-Pedersen, and Peter I Borel. Photonic crystal waveguides with semi-slow light and tailored dispersion properties. *Optics express*, 14(20):9444–9450, 2006.

[60] Andrey A Sukhorukov, Andrei V Lavrinenko, Dmitry N Chigrin, Dmitry E Pelinovsky, and Yuri S Kivshar. Slow-light dispersion in coupled periodic waveguides. *JOSA B*, 25(12):C65–C74, 2008.

[61] Claudius Locker, Kubilay Sertel, and John L Volakis. Emulation of propagation in layered anisotropic media with equivalent coupled microstrip lines. *IEEE Microwave and Wireless Components Letters*, 16(12):642–644, 2006.

[62] Justin R Burr, Nadav Gutman, C Martijn de Sterke, Ilya Vitebskiy, and Ronald M Reano. Degenerate band edge resonances in coupled periodic silicon optical waveguides. *Optics Express*, 21(7):8736–8745, 2013.

[63] Alexander Figotin and Ilya Vitebskiy. Oblique frozen modes in periodic layered media. *Physical Review E*, 68(3):036609, 2003.

[64] Alex Figotin and Ilya Vitebskiy. Gigantic transmission band-edge resonance in periodic stacks of anisotropic layers. *Physical Review E*, 72(3):036619, 2005.

[65] Alex Figotin and Ilya Vitebskiy. Frozen light in photonic crystals with degenerate band edge. *Physical Review E*, 74(6):066613, 2006.

[66] Mehdi Veysi, Mohamed A. K. Othman, Alexander Figotin, and Filippo Capolino. Degenerate band edge laser. *Physical Review B*, 97(19):195107, MAY 7 2018.

[67] Hossein Hodaei, Absar U Hassan, Steffen Wittek, Hipolito Garcia-Gracia, Ramy El-Ganainy, Demetrios N Christodoulides, and Mercedeh Khajavikhan. Enhanced sensitivity at higher-order exceptional points. *Nature*, 548(7666):187–191, 2017.

[68] Mohamed A. K. Othman, Farshad Yazdi, Alex Figotin, and Filippo Capolino. Giant gain enhancement in photonic crystals with a degenerate band edge. *Physical Review B*, 93(2):024301, JAN 11 2016.

[69] F. Alpeggiani, K. Y. Bliokh, F. Nori, and L. Kuipers. Electromagnetic helicity in complex media. *Phys. Rev. Lett.*, 120:243605, JUN 15 2018.

[70] Mina Hanifeh, Mohammad Albooyeh, and Filippo Capolino. Optimally chiral light: Upper bound of helicity density of structured light for chirality detection of matter at nanoscale. *ACS Photonics*, 7:2682–2691, Oct 2020.

[71] Liang Fang and Jian Wang. Optical trapping separation of chiral nanoparticles by subwavelength slot waveguides. *Physical Review Letters*, 127(23), DEC 1 2021.

[72] Mohammad Kamandi, Mohammad Albooyeh, Mehdi Veysi, Mohsen Rajaei, Jinwei Zeng, H. Kumar Wickramasinghe, and Filippo Capolino. Unscrambling structured chirality with structured light at the nanoscale using photoinduced force. *ACS Photonics*, 5:4360–4370, Nov 2018.

[73] Mina Hanifeh, Mohammad Albooyeh, and Filippo Capolino. Helicity maximization below the diffraction limit. *Phys. Rev. B*, 102:165419, Oct 2020.

[74] Mina Hanifeh and Filippo Capolino. Theory of vector beams for chirality and magnetism detection of subwavelength particles. In *Electromagnetic Vortices*, chapter 13, pages 401–421. John Wiley & Sons, Ltd, 2021.

[75] P. Lancaster. On eigenvalues of matrices dependent on a parameter. *Numerische Mathematik*, 6(1):377–387, December 1964.

[76] Tosio Kato. *Perturbation theory for linear operators*, chapter 2. Springer-Verlag New York Inc., New York, 1966.

[77] Alexander P. Seyranian. Sensitivity analysis of multiple eigenvalues. *Mech. Based Des. Struct. Mach.*, 21(2):261–284, 1993.

[78] WD Heiss. Exceptional points of non-hermitian operators. *J. Phys. A Math. Theor.*, 37(6):2455–2464, FEB 13 2004.

[79] Christian E. Rueter, Konstantinos G. Makris, Ramy El-Ganainy, Demetrios N. Christodoulides, Mordechai Segev, and Detlef Kip. Observation of parity-time symmetry in optics. *Nat. Phys.*, 6(3):192–195, MAR 2010.

[80] W. Heiss. The physics of exceptional points. *Journal of Physics A Mathematical and Theoretical*, 45(44, SI):444016, NOV 9 2012.

[81] Hamidreza Ramezani, Tsampikos Kottos, Ramy El-Ganainy, and Demetrios N. Christodoulides. Unidirectional nonlinear $\mathcal{PT}$-symmetric optical structures. *Phys. Rev. A*, 82:043803, Oct 2010.

[82] Joseph Schindler, Ang Li, Mei C. Zheng, F. M. Ellis, and Tsampikos Kottos. Experimental study of active lrc circuits with pt symmetries. *Phys. Rev. A*, 84(4):040101, OCT 13 2011.

[83] James Gear, Fu Liu, S. T. Chu, Stefan Rotter, and Jensen Li. Parity-time symmetry from stacking purely dielectric and magnetic slabs. *Phys. Rev. A*, 91(3):033825, MAR 20 2015.

[84] A Figotin and I Vitebskiy. Electromagnetic unidirectionality in magnetic photonic crystals. *Physical Review B*, 67(16):165210, APR 15 2003.

[85] Matthew B. Stephanson, Kubilay Sertel, and John L. Volakis. Frozen modes in coupled microstrip lines printed on ferromagnetic substrates. *IEEE Microw Wirel Compon Lett*, 18(5):305–307, MAY 2008.

[86] Gokhan Mumcu, Kubilay Sertel, and John L. Volakis. Lumped circuit models for degenerate band edge and magnetic photonic crystals. *IEEE Microw Wirel Compon Lett*, 20(1):4–6, JAN 2010.

[87] Nil Apaydin, Lanlin Zhang, Kubilay Sertel, and John L. Volakis. Experimental validation of frozen modes guided on printed coupled transmission lines. *IEEE Trans Microw Theory Tech*, 60(6, 1):1513–1519, JUN 2012.

[88] Nadav Gutman, W. Hugo Dupree, Yue Sun, Andrey A. Sukhorukov, and C. Martijn de Sterke. Frozen and broadband slow light in coupled periodic nanowire waveguides. *Optics Express*, 20(4):3519–3528, FEB 13 2012.

[89] H. Ramezani, S. Kalish, I. Vitebskiy, and T. Kottos. Unidirectional lasing emerging from frozen light in nonreciprocal cavities. *Phys. Rev. Lett.*, 112(4):043904, JAN 28 2014.

[90] Ilya A Volkov and Roman S Savelev. Unidirectional coupling of a quantum emitter to a subwavelength grating waveguide with an engineered stationary inflection point. *Phys Rev B*, 104(24):245408, 2021.

[91] Banaful Paul, Niru K. Nahar, and Kubilay Sertel. Frozen mode in coupled silicon ridge waveguides for optical true time delay applications. *Journal of the Optical Society of America B - Optical Physics*, 38(5):1435–1441, MAY 1 2021.

[92] William Tuxbury, Rodion Kononchuk, and Tsampikos Kottos. Non-resonant exceptional points as enablers of noise-resilient sensors. *Commun. Phys.*, 5(1):210, AUG 16 2022.

[93] A Figotin and I Vitebskiy. Oblique frozen modes in periodic layered media. *Phys. Rev. E*, 68(3, 2):036609, SEP 2003.

[94] JP Dowling, M Scalora, MJ Bloemer, and CM Bowden. The photonic band-edge laser - a new approach to gain enhancement. *Journal of Applied physics*, 75(4):1896–1899, FEB 15 1994.

[95] Jacob Scheuer and Ori Weiss. The serpentine optical waveguide: engineering the dispersion relations and the stopped light points. *Optics Express*, 19(12):11517–11528, JUN 6 2011.

[96] Anthony E. Siegman. *Lasers*, chapter 2. Univ. Science books, Mill Valley, Calif, 1986.

[97] Kerry Vahala. *Optical Microcavities*, volume 5 of *Advanced Series in Applied Physics*, chapter 4. World Scientific, December 2004.

[98] Amnon Yariv, Pochi Yeh, and Amnon Yariv. *Photonics: optical electronics in modern communications*, chapter 12. The Oxford series in electrical and computer engineering. Oxford University Press, New York, 6th edition, 2007.

[99] A Figotin and I Vitebskiy. Gigantic transmission band-edge resonance in periodic stacks of anisotropic layers. *Physical Review E*, 72(3, 2):036619, Sep 2005.

[100] Joseph Thomas. Verdeyen. *Laser electronics*, chapter 6. Prentice-Hall series in solid state physical electronics. Prentice Hall, Englewood Cliffs, NJ, 3rd edition, 1995.

[101] Jure Grgic, Johan Raunkjr Ott, Fengwen Wang, Ole Sigmund, Antti-Pekka Jauho, Jesper Mork, and N. Asger Mortensen. Fundamental limitations to gain enhancement in periodic media and waveguides. *Physical Review Letters*, 108(18):183903, MAY 4 2012.

[102] Ilya V. Doronin, Alexander A. Zyablovsky, Evgeny S. Andrianov, Alexander A. Pukhov, Yurii E. Lozovik, and Alexey P. Vinogradov. Universal lasing condition. *Sci. Rep.*, 11(1):4197, FEB 18 2021.

[103] Mohamed Y. Nada and Filippo Capolino. Exceptional point of sixth-order degeneracy in a modified coupled-resonator optical waveguide. *Journal of the Optical Society of America B - Optical Physics*, 37(8):2319–2328, AUG 1 2020.

[104] J Ballato, A Ballato, A Figotin, and I Vitebskiy. Frozen light in periodic stacks of anisotropic layers. *Phys. Rev. E*, 71(3, 2):036612, MAR 2005.

[105] Aaron Welters. On explicit recursive formulas in the spectral perturbation analysis of a jordan block. *SIAM Journal on Matrix Analysis and Applications*, 32(1):1–22, 2011.

[106] Farshad Yazdi, Mohamed A. K. Othman, Mehdi Veysi, Alexander Figotin, and Filippo Capolino. A new amplification regime for traveling wave tubes with third-order modal degeneracy. *IEEE Trans Plasma Sci*, 46(1):43–56, JAN 2018.

[107] Zhi Ming Gan, Huanan Li, and Tsampikos Kottos. Effects of disorder in frozen-mode light. *Opt. Lett.*, 44(11):2891–2894, Jun 2019.

[108] W. Tuxbury, L. J. Fernandez-Alcazar, I. Vitebskiy, and T. Kottos. Scaling theory of absorption in the frozen mode regime. *Opt. Lett.*, 46(13):3053–3056, Jul 2021.

[109] Yan Xu, Baojian Wu, Xinrui Jiang, Haomiao Guo, and Feng Wen. Experimental measurement of absorption coefficients for effective erbium-doping concentration to optimize few-mode erbium-doped fiber amplifiers with low differential mode gain. *Photonics*, 8(6):185, JUN 2021.

[110] M Sumetsky. Uniform coil optical resonator and waveguide: transmission spectrum, eigenmodes, and dispersion relation. *Optics Express*, 13(11):4331–4340, 2005.

[111] Toshihiko Baba and Daisuke Mori. Slow light engineering in photonic crystals. *Journal of Physics D: Applied Physics*, 40(9):2659, 2007.

[112] Jacob Scheuer and Mikhail Sumetsky. Optical-fiber microcoil waveguides and resonators and their applications for interferometry and sensing. *Laser & Photonics Reviews*, 5(4):465–478, Jul 2011.

[113] Justin R. Burr, Nadav Gutman, C. Martijn de Sterke, Ilya Vitebskiy, and Ronald M. Reano. Degenerate band edge resonances in coupled periodic silicon optical waveguides. *Opt. Express*, 21(7):8736–8745, Apr 2013.

[114] Banaful Paul, Kubilay Sertel, and Niru K Nahar. Experimental demonstration of frozen-mode enabled slow-wave photonic device in coupled silicon ridge waveguides. *Journal of Lightwave Technology*, 2024.

[115] Banaful Paul, Kubilay Sertel, and Niru K Nahar. Photonic beamforming for 5g and beyond: A review of true time delay devices enabling ultra-wideband beamforming for mmwave communications. *IEEE Access*, 10:75513–75526, 2022.

[116] A. Herrero-Parareda, N. Furman, T. Mealy, R. Gibson, R. Bedford, I. Vitebskiy, and F. Capolino. Lasing at a stationary inflection point. *Opt. Mater. Express*, 13(5):1290–1306, May 2023.

[117] Nathaniel Furman, Albert Herrero-Parareda, Ilya Vitebskiy, Ricky Gibson, Bradley Thompson, Robert Bedford, and Filippo Capolino. Impact of fabrication disorder on lasing near a stationary inflection point. *J. Opt. Soc. Am. B*, 42(4):879–889, Apr 2025.

[118] Kessem Zamir-Abramovich, Nathaniel Furman, Albert Herrero-Parareda, Filippo Capolino, and Jacob Scheuer. Low-threshold lasing with a stationary inflection point in a three-coupled-waveguide structure. *Physical Review A*, 108(6):063504, 2023.

[119] Nathaniel Furman, Tarek Mealy, Md Shafiqul Islam, Ilya Vitebskiy, Ricky Gibson, Robert Bedford, Ozdal Boyraz, and Filippo Capolino. Frozen mode regime in an optical waveguide with a distributed Bragg reflector. *Journal of the Optical Society of America B*, 40(5):966, May 2023.

[120] Yonathan Dattner and Orly Yadid-Pecht. Analysis of the effective refractive index of silicon waveguides through the constructive and destructive interference in a mach–zehnder interferometer. *IEEE Photonics Journal*, 3(6):1123–1132, 2011.

[121] Nicholas M. Fahrenkopf, Colin McDonough, Gerald L. Leake, Zhan Su, Erman Timurdogan, and Douglas D. Coolbaugh. The aim photonics mpw: A highly accessible cutting edge technology for rapid prototyping of photonic integrated circuits. *IEEE Journal of Selected Topics in Quantum Electronics*, 25(5):1–6, 2019.

[122] Robert Marosi, Tarek Mealy, Alexander Figotin, and Filippo Capolino. Three-way serpentine slow wave structures with stationary inflection point and enhanced interaction impedance. *IEEE Transactions on Plasma Science*, 50(12):4820–4833, 2022.

[123] Makoto Okai. Spectral characteristics of distributed feedback semiconductor lasers and their improvements by corrugation-pitch-modulated structure. *Journal of Applied Physics*, 75(1):1–29, 01 1994.

[124] John E Carroll, James Whiteaway, Dick Plumb, et al. *Distributed feedback semiconductor lasers.* IET, 1998.

[125] H. Ghafouri-Shiraz. *An Introduction to Optical Communication Systems*, chapter 1, pages 1–30. John Wiley& Sons, Ltd, 2003.

[126] Geert Morthier and Patrick Vankwikelberge. *Handbook of distributed feedback laser diodes, Second Ed.* Artech House, 2013.

[127] W.H. Loh and R.I. Laming. 1.55 µm phase-shifted distributed feedback fibre laser. *Electronics Letters*, 31:1440–1442, 1995.

[128] H. Ghafouri-Shiraz. *Structural Impacts on the Solutions of Coupled Wave Equations: An Overview*, chapter 3, pages 79–100. John Wiley& Sons, Ltd, 2003.

[129] H. Ghafouri-Shiraz. *Principles of Distributed Feedback Semiconductor Laser Diodes: Coupled Wave Theory*, chapter 2, pages 31–78. John Wiley& Sons, Ltd, 2003.

[130] Jingsi Li, Huan Wang, Xiangfei Chen, Zuowei Yin, Yuechun Shi, Yanqing Lu, Yitang Dai, and Hongliang Zhu. Experimental demonstration of distributed feedback semiconductor lasers based on reconstruction-equivalent-chirp technology. *Opt. Express*, 17(7):5240–5245, Mar 2009.

[131] Tarek Mealy and Filippo Capolino. Degenerate distributed feedback photonic structure with two gratings exhibiting degenerate band edge. *IEEE Photon. Technol. Lett.*, 35(4):187–190, FEB 15 2023.

[132] Michael G. Wood, Justin R. Burr, and Ronald M. Reano. Degenerate band edge resonances in periodic silicon ridge waveguides. *Opt. Lett.*, 40(11):2493–2496, Jun 2015.

[133] Mohamed Y. Nada, Ohamed A. K. Othman, Ozdal Boyraz, and Filippo Capolino. Giant resonance and anomalous quality factor scaling in degenerate band edge coupled resonator optical waveguides. *Journal of Lightwave Technology*, 36(14):3030–3039, JUL 15 2018.

[134] Mohamed A. K. Othman, Xuyuan Pan, Georgios Atmatzakis, Christos G. Christodoulou, and Filippo Capolino. Experimental demonstration of degenerate band edge in metallic periodically loaded circular waveguide. *IEEE Transactions on Microwave Theory and Techniques*, 65(11):4037–4045, 2017.

[135] Dmitry Oshmarin, Farshad Yazdi, Mohamed AK Othman, Jeff Sloan, Mohammad Radfar, Michael M Green, and Filippo Capolino. New oscillator concept based on band edge degeneracy in lumped double-ladder circuits. *IET Circuits, Devices & Systems*, 13(7):950–957, 2019.

[136] Ahmed F. Abdelshafy, Dmitry Oshmarin, Mohamed A. K. Othman, Michael M. Green, and Filippo Capolino. Distributed degenerate band edge oscillator. *IEEE Transactions on Antennas and Propagation*, 69(3):1821–1824, 2021.

[137] Dmitry Oshmarin, Ahmed F. Abdelshafy, Alireza Nikzamir, Michael M. Green, and Filippo Capolino. Experimental demonstration of a new oscillator concept based on degenerate band edge in microstrip circuit. *arXiv 2109.07002*, 2021.

[138] M. L. Povinelli, Steven G. Johnson, and J. D. Joannopoulos. Slow-light, band-edge waveguides for tunable time delays. *Opt. Express*, 13(18):7145–7159, Sep 2005.

[139] Pierre Pottier, Marco Gnan, and Richard M. De La Rue. Efficient coupling into slow-light photonic crystal channel guides using photonic crystal tapers. *Opt. Express*, 15(11):6569–6575, May 2007.

[140] P. Velha, J. P. Hugonin, and P. Lalanne. Compact and efficient injection of light into band-edge slow-modes. *Opt. Express*, 15(10):6102–6112, May 2007.

[141] Lawrence Carin and Leopold B Felsen. Time harmonic and transient scattering by finite periodic flat strip arrays: Hybrid (ray)-(floquet mode)-(mom) algorithm. *IEEE Transactions on Antennas and Propagation*, 41(4):412–421, 1993.

[142] F Capolino and Matteo Albani. Truncation effects in a semi-infinite periodic array of thin strips: A discrete wiener-hopf formulation. *Radio Science*, 44(02):1–14, 2009.

[143] C. A. Barrios, B. Sánchez, K. B. Gylfason, A. Griol, H. Sohlström, M. Holgado, and R. Casquel. Demonstration of slot-waveguide structures on silicon nitride / silicon oxide platform. *Opt. Express*, 15(11):6846–6856, May 2007.

[144] H Kogelnik and CV Shank. Coupled-wave theory of distributed feedback lasers. *Journal of Applied Physics*, 43(5):2327, 1972.

[145] Salih Yarga, Kubilay Sertel, and John L. Volakis. Degenerate band edge crystals for directive antennas. *IEEE Transactions on Antennas and Propagation*, 56(1):119–126, 2008.

[146] Nadav Gutman, Lindsay C. Botten, Andrey A. Sukhorukov, and C. Martijn de Sterke. Degenerate band edges in optical fiber with multiple grating: efficient coupling to slow light. *Opt. Lett.*, 36(16):3257–3259, Aug 2011.

[147] Mohamed A. K. Othman, Venkata Ananth Tamma, and Filippo Capolino. Theory and new amplification regime in periodic multimodal slow wave structures with degeneracy interacting with an electron beam. *IEEE Transactions on Plasma Science*, 44(4):594–611, 2016.

[148] Junping Geng, Richard W. Ziolkowski, Sawyer Cambell, Ronghong Jin, and Xianling Liang. Studies of nanometer antennas incorporating gain material using CST. In *2011 IEEE International Symposium on Antennas and Propagation (APSURSI)*, pages 1624–1627, 2011.

[149] Kessem Zamir-Abramovich, Nathaniel Furman, Albert Herrero-Parareda, Filippo Capolino, and Jacob Scheuer. Low-threshold lasing with a stationary inflection point in a three-coupled-waveguide structure. *Phys. Rev. A*, 108:063504, Dec 2023.

[150] Ehsan Mobini, Daniel H. G. Espinosa, Kaustubh Vyas, and Ksenia Dolgaleva. Algaas nonlinear integrated photonics. *Micromachines*, 13(7), 2022.

[151] Robert W. Boyd. *Nonlinear Optics, Third Edition.* Academic Press, Inc., USA, 3rd edition, 2008.

[152] B. Shi, Z. M. Jiang, and Xun Wang. Defective photonic crystals with greatly enhanced second-harmonic generation. *Opt. Lett.*, 26(15):1194–1196, Aug 2001.

[153] Marco Liscidini, Andrea Locatelli, Lucio Claudio Andreani, and Costantino De Angelis. Maximum-exponent scaling behavior of optical second-harmonic generation in finite multilayer photonic crystals. *Phys. Rev. Lett.*, 99:053907, Aug 2007.

[154] Luca Carletti, Kirill Koshelev, Costantino De Angelis, and Yuri Kivshar. Giant nonlinear response at the nanoscale driven by bound states in the continuum. *Phys. Rev. Lett.*, 121:033903, Jul 2018.

[155] Momchil Minkov, Dario Gerace, and Shanhui Fan. Doubly resonant χ(2) nonlinear photonic crystal cavity based on a bound state in the continuum. *Optica*, 6(8):1039–1045, Aug 2019.

[156] Fan Ye, Yue Yu, Xiang Xi, and Xiankai Sun. Second-harmonic generation in etchless lithium niobate nanophotonic waveguides with bound states in the continuum. *Laser & Photonics Reviews*, 16(3):2100429, 2022.

[157] Yu Qiu, Dexian Yan, Xiangjun Li, Le Zhang, and Jining Li. Highly efficient second harmonic generation assisted by the quasi-bound states in the continuum from algaas meta-gratings. *Optics Communications*, 546:129772, 2023.

[158] Ran Hao, Bilin Ye, Jinhong Xu, and Yonggang Zou. Performance optimization of planar photonic crystal bound states in the continuum cavities: Mitigating finite-size effects. *Frontiers of Optoelectronics*, 18(1):3, March 2025.

[159] Christelle Monat, Christian Grillet, Bill Corcoran, David J. Moss, Benjamin J. Eggleton, Thomas P. White, and Thomas F. Krauss. Investigation of phase matching for third-harmonic generation in silicon slow light photonic crystal waveguides using fourier optics. *Opt. Express*, 18(7):6831–6840, Mar 2010.

[160] Tarek Mealy, Mohamed Y. Nada, Ahmed F. Abdelshafy, Ehsan Hafezi, and Filippo Capolino. Exceptional points of degeneracy in electromagnetic periodic waveguides and the role of symmetries. In *2022 16th European Conference on Antennas and Propagation (EuCAP)*, pages 1–4, 2022.

[161] S. Adachi. *GaAs and Related Materials: Bulk Semiconducting and Superlattice Properties*. G - Reference,Information and Interdisciplinary Subjects Series. World Scientific, 1994.

[162] Konstantinos Papatryfonos, Todora Angelova, Antoine Brimont, Barry Reid, Stefan Guldin, Peter Raymond Smith, Mingchu Tang, Keshuang Li, Alwyn J. Seeds, Huiyun Liu, and David R. Selviah. Refractive indices of MBE-grown AlxGa(1-x)As ternary alloys in the transparent wavelength region. *AIP Advances*, 11(2):025327, February 2021.

[163] K.D. Choquette, K.M. Geib, C.I.H. Ashby, R.D. Twesten, O. Blum, H.Q. Hou, D.M. Follstaedt, B.E. Hammons, D. Mathes, and R. Hull. Advances in selective wet oxidation of algaas alloys. *IEEE Journal of Selected Topics in Quantum Electronics*, 3(3):916–926, 1997.

[164] Jon M. Bendickson, Jonathan P. Dowling, and Michael Scalora. Analytic expressions for the electromagnetic mode density in finite, one-dimensional, photonic band-gap structures. *Phys. Rev. E*, 53:4107–4121, Apr 1996.

[165] Thomas Christopoulos, Odysseas Tsilipakos, Georgios Sinatkas, and Emmanouil E. Kriezis. On the calculation of the quality factor in contemporary photonic resonant structures. *Opt. Express*, 27(10):14505–14522, May 2019.

[166] Tao Chen, Junqiang Sun, Linsen Li, and Jianguan Tang. Proposal for efficient terahertz-wave difference frequency generation in an algaas photonic crystal waveguide. *Journal of Lightwave Technology*, 30(13):2156–2162, 2012.

[167] D. Duchesne, K. A. Rutkowska, M. Volatier, F. Légaré, S. Delprat, M. Chaker, D. Modotto, A. Locatelli, C. De Angelis, M. Sorel, D. N. Christodoulides, G. Salamo, R. Arès, V. Aimez, and R. Morandotti. Second harmonic generation in algaas photonic wires using low power continuous wave light. *Opt. Express*, 19(13):12408–12417, Jun 2011.

[168] Stuart May, Michael Kues, Matteo Clerici, and Marc Sorel. Second-harmonic generation in algaas-on-insulator waveguides. *Opt. Lett.*, 44(6):1339–1342, Mar 2019.

[169] X. Yu, L. Scaccabarozzi, J. S. Harris, P. S. Kuo, and M. M. Fejer. Efficient continuous wave second harmonic generation pumped at 1.55 μm in quasi-phase-matched algaas waveguides. *Opt. Express*, 13(26):10742–10748, Dec 2005.

[170] Iännis Roland, Marco Ravaro, Stéphan Suffit, Pascal Filloux, Aristide Lemaître, Ivan Favero, and Giuseppe Leo. Second-harmonic generation in suspended algaas waveguides: A comparative study. *Micromachines*, 11(2), 2020.

[171] Eric J. Stanton, Jeff Chiles, Nima Nader, Galan Moody, Nicolas Volet, Lin Chang, John E. Bowers, Sae Woo Nam, and Richard P. Mirin. Efficient second harmonic generation in nanophotonic gaas-on-insulator waveguides. *OPTICS EXPRESS*, 28(7):9521–9532, MAR 30 2020.

[172] C. Q. Xu, K. Takemasa, K. Nakamura, K. Shinozaki, H. Okayama, and T. Kamijoh. Device length dependence of optical second-harmonic generation in AlGaAs quasiphase matched waveguides. *Applied Physics Letters*, 70(12):1554–1556, March 1997.

[173] Payam Abolghasem, Junbo Han, Bhavin J. Bijlani, Arghavan Arjmand, and Amr S. Helmy. Highly efficient second-harmonic generation in monolithic matching layer enhanced al$_x$ ga$_{1-x}$ as bragg reflection waveguides. *IEEE Photonics Technology Letters*, 21(19):1462–1464, 2009.

[174] M. Savanier, A. Andronico, A. Lemaître, E. Galopin, C. Manquest, I. Favero, S. Ducci, and G. Leo. Large second-harmonic generation at 1.55μmin oxidized algaas waveguides. *Opt. Lett.*, 36(15):2955–2957, Aug 2011.

[175] Paul G. Kwiat, Klaus Mattle, Harald Weinfurter, Anton Zeilinger, Alexander V. Sergienko, and Yanhua Shih. New high-intensity source of polarization-entangled photon pairs. *Phys. Rev. Lett.*, 75:4337–4341, Dec 1995.

[176] W. Bogaerts, P. De Heyn, T. Van Vaerenbergh, K. De Vos, S. Kumar Selvaraja, T. Claes, P. Dumon, P. Bienstman, D. Van Thourhout, and R. Baets. Silicon microring resonators. *Laser & Photonics Reviews*, 6(1):47–73, 2012.

[177] Laurence David Barron. True and false chirality and absolute enantioselection. *Rend. Lincei.-Sci. Fis. Nat.*, 24:179–189, Sep 2013.

[178] Cláudia Ribeiro, Cristiana Santos, Valter Gonçalves, Ana Ramos, Carlos Afonso, and Maria Elizabeth Tiritan. Chiral drug analysis in forensic chemistry: An overview. *Molecules*, 23:262, 2018.

[179] Sachin Mane. Racemic drug resolution: a comprehensive guide. *Anal. Methods*, 8:7567–7586, 2016.

[180] P. O. Carvalho, Q. B. Cass, S. A. Calafatti, F. J. Contesini, and R. Bizaco. Review - alternatives for the separation of drug enantiomers: Ibuprofen as a model compound. *Braz. J. Chem. Eng.*, 23:291–300, JUL-SEP 2006.

[181] W. Z. Jia and L. F. Wei. Probing molecular chirality by coherent optical absorption spectra. *Phys. Rev. A*, 84:053849, Nov 2011.

[182] Lisa V. Poulikakos, Philipp Gutsche, Kevin M. McPeak, Sven Burger, Jens Niegemann, Christian Hafner, and David J. Norris. Optical chirality flux as a useful far-field probe of chiral near fields. *ACS Photonics*, 3:1619–1625, Sep 2016.

[183] Yang Zhao, Amr A. E. Saleh, Marie Anne van de Haar, Brian Baum, Justin A. Briggs, Alice Lay, Olivia A. Reyes-Becerra, and Jennifer A. Dionne. Nanoscopic control and quantification of enantioselective optical forces. *Nat. Nanotechnol.*, 12:1055–1059, NOV 2017.

[184] Manman Li, Shaohui Yan, Yanan Zhang, Peng Zhang, and Baoli Yao. Enantioselective optical trapping of chiral nanoparticles by tightly focused vector beams. *J. Opt. Soc. Am. B-Opt. Phys.*, 36:2099–2105, AUG 1 2019.

[185] Michelle L. Solomon, Amr A. E. Saleh, Lisa V. Poulikakos, John M. Abendroth, Loza F. Tadesse, and Jennifer A. Dionne. Nanophotonic platforms for chiral sensing and separation. *Accounts Chem. Res.*, 53:588–598, Mar 2020.

[186] Andrew Lininger, Giovanna Palermo, Alexa Guglielmelli, Giuseppe Nicoletta, Madhav Goel, Michael Hinczewski, and Giuseppe Strangi. Chirality in light–matter interaction. *Advanced Materials*, page 2107325, May 2022.

[187] Yiqiao Tang and Adam E. Cohen. Optical chirality and its interaction with matter. *Phys. Rev. Lett.*, 104:163901, Apr 2010.

[188] Konstantin Y. Bliokh and Franco Nori. Characterizing optical chirality. *Phys. Rev. A*, 83:021803, Feb 2011.

[189] Kayn A. Forbes and Dale Green. Customized optical chirality of vortex structured light through state and degree-of-polarization control. *Phys. Rev. A*, 107:063504, Jun 2023.

[190] Robert P. Cameron, Stephen M. Barnett, and Alison M. Yao. Optical helicity, optical spin and related quantities in electromagnetic theory. *New Journal of Physics*, 14:053050, May 2012.

[191] N. Mackinnon. On the differences between helicity and chirality. *J Opt.*, 21:125402, DEC 2019.

[192] José L Trueba and Antonio F Rañada. The electromagnetic helicity. *Eur. J. Phys.*, 17:141–144, may 1996.

[193] J. Enrique Vázquez-Lozano and Alejandro Martínez. Optical chirality in dispersive and lossy media. *Phys. Rev. Lett.*, 121:043901, Jul 2018.

[194] Konstantin Y. Bliokh and Franco Nori. Transverse and longitudinal angular momenta of light. *Physics Reports*, 592:1–38, 2015.

[195] S.A. Tretyakov and F. Mariotte. Maxwell garnett modeling of uniaxial chiral composites with bianisotropic inclusions. *Journal of Electromagnetic Waves and Applications*, 9:1011–1025, 1995.

[196] Laurence D. Barron. Molecules in electric and magnetic fields. In *Molecular Light Scattering and Optical Activity*, chapter 2, pages 53–122. Cambridge University Press, Cambridge, 2004.

[197] Amaury Hayat, J. P. Balthasar Mueller, and Federico Capasso. Lateral chirality-sorting optical forces. *Proc. Natl. Acad. Sci. U. S. A.*, 112:13190–13194, Oct 27 2015.

[198] Michelle L. Solomon, Jack Hu, Mark Lawrence, Aitzol Garcia-Etxarri, and Jennifer A. Dionne. Enantiospecific optical enhancement of chiral sensing and separation with dielectric metasurfaces. *ACS Photonics*, 6:43–49, JAN 2019.

[199] Ershad Mohammadi, Ahad Tavakoli, Parisa Dehkhoda, Yasaman Jahani, Kosmas L. Tsakmakidis, Andreas Tittl, and Hatice Altug. Accessible superchiral near-fields driven by tailored electric and magnetic resonances in all-dielectric nanostructures. *ACS Photonics*, 6:1939–1946, AUG 2019.

[200] Jingang Li, Mingsong Wang, Zilong Wu, Huanan Li, Guangwei Hu, Taizhi Jiang, Jianhe Guo, Yaoran Liu, Kan Yao, Zhihan Chen, Jie Fang, Donglei Fan, Brian A. Korgel, Andrea Alu, and Yuebing Zheng. Tunable chiral optics in all-solid-phase reconfigurable dielectric nanostructures. *Nano Lett.*, 21:973–979, JAN 27 2021.

[201] Martin Schaferling, Daniel Dregely, Mario Hentschel, and Harald Giessen. Tailoring enhanced optical chirality: Design principles for chiral plasmonic nanostructures. *Phys. Rev. X*, 2:031010, Aug 2012.

[202] Ventsislav K. Valev, Jeremy J. Baumberg, Concita Sibilia, and Thierry Verbiest. Chirality and chiroptical effects in plasmonic nanostructures: Fundamentals, recent progress, and outlook. *Advanced Materials*, 25:2517–2534, 2013.

[203] Yang Luo, Cheng Chi, Meiling Jiang, Ruipeng Li, Shuai Zu, Yu Li, and Zheyu Fang. Plasmonic chiral nanostructures: Chiroptical effects and applications. *Advanced Optical Materials*, 5:1700040, 2017.

[204] Marco Finazzi, Paolo Biagioni, Michele Celebrano, and Lamberto Duò. Quasistatic limit for plasmon-enhanced optical chirality. *Phys. Rev. B*, 91:195427, May 2015.

[205] D. Beutel, P. Scott, M. Wegener, C. Rockstuhl, and I. Fernandez-Corbaton. Enhancing the optical rotation of chiral molecules using helicity preserving all-dielectric metasurfaces. *Applied Physics Letters*, 118:221108, 06 2021.

[206] Carmelo Rosales-Guzman, Karen Volke-Sepulveda, and Juan P. Torres. Light with enhanced optical chirality. *Opt. Lett.*, 37:3486–3488, SEP 1 2012.

[207] Mehdi Veysi, Caner Guclu, and Filippo Capolino. Focused azimuthally polarized vector beam and spatial magnetic resolution below the diffraction limit. *J. Opt. Soc. Am. B-Opt. Phys.*, 33:2265–2277, NOV 1 2016.

[208] Caner Guclu, Mehdi Veysi, and Filippo Capolino. Photoinduced magnetic nanoprobe excited by an azimuthally polarized vector beam. *ACS Photonics*, 3:2049–2058, Nov 2016.

[209] Jinwei Zeng, Mahsa Darvishzadeh-Varcheie, Mohammad Albooyeh, Mohsen Rajaei, Mohammad Kamandi, Mehdi Veysi, Eric O. Potma, Filippo Capolino, and H. K. Wickramasinghe. Exclusive magnetic excitation enabled by structured light illumination in a nanoscale mie resonator. *ACS Nano*, 12:12159–12168, DEC 2018.

[210] Jinwei Zeng, Fei Huang, Caner Guclu, Mehdi Veysi, Mohammad Albooyeh, H. Kumar Wickramasinghe, and Filippo Capolino. Sharply focused azimuthally polarized beams with magnetic dominance: Near-field characterization at nanoscale by photoinduced force microscopy. *ACS Photonics*, 5:390–397, FEB 2018.

[211] Manuel Blanco, Ferran Cambronero, M. Teresa Flores-Arias, Enrique Conejero Jarque, Luis Plaja, and Carlos Hernandez-Garcia. Ultraintense femtosecond magnetic nanoprobes induced by azimuthally polarized laser beams. *ACS Photonics*, 6:38–42, JAN 2019.

[212] Qiwen Zhan. Cylindrical vector beams: from mathematical concepts to applications. *Adv. Opt. Photon.*, 1:1–57, Jan 2009.

[213] Guanghao Rui and Qiwen Zhan. Trapping of resonant metallic nanoparticles with engineered vectorial optical field. *Nanophotonics*, 3:351–361, DEC 2014.

[214] Di Lin, J. M. O. Daniel, M. Gecevicius, M. Beresna, P. G. Kazansky, and W. A. Clarkson. Cladding-pumped ytterbium-doped fiber laser with radially polarized output. *Opt. Lett.*, 39:5359–5361, Sep 2014.

[215] Jörg S. Eismann, Martin Neugebauer, and Peter Banzer. Exciting a chiral dipole moment in an achiral nanostructure. *Optica*, 5:954–959, Aug 2018.

[216] Franco Gori. Polarization basis for vortex beams. *J. Opt. Soc. Am. A*, 18:1612–1617, Jul 2001.

[217] Albert Herrero-Parareda and Filippo Capolino. Optimally chiral optical trapping. In Kishan Dholakia and Gabriel C. Spalding, editors, *Optical Trapping and Optical Micromanipulation XX*, volume 12649, page 126490G. International Society for Optics and Photonics, SPIE, 2023.

[218] K. Koksal, M. Babiker, and V. E. Lembessis. Optical characteristics of radially-polarised twisted light. *Journal of Optics*, 25:065501, Jun 1 2023.

[219] K. Koksal, M. Babiker, V. E. Lembessis, and J. Yuan. Hopf index and the helicity of elliptically polarized twisted light. *J. Opt. Soc. Am. B*, 39:459–466, Feb 2022.

[220] M. Babiker, J. Yuan, V.E. Lembessis, and K. Koksal. The zero helicity and chirality of optical vortices. *Optics Communications*, 525:128846, 2022.

[221] Pawel Wozniak, Israel De Leon, Katja Hoeflich, Gerd Leuchs, and Peter Banzer. Interaction of light carrying orbital angular momentum with a chiral dipolar scatterer. *Optica*, 6:961–965, AUG 20 2019.

[222] Kayn A. Forbes. Optical helicity of unpolarized light. *Phys. Rev. A*, 105:023524, Feb 2022.

[223] Kayn A. Forbes and Dale Green. Enantioselective optical gradient forces using 3D structured vortex light. *Optics Communications*, 515:128197, July 2022.

[224] Lyuzhou Ye, Longqing Yang, Xiao Zheng, and Shaul Mukamel. Enhancing circular dichroism signals with vector beams. *Phys. Rev. Lett.*, 126:123001, Mar 2021.

[225] Jiaan Cao, Lyuzhou Ye, Dawei He, Xiao Zheng, and Shaul Mukamel. Magnet-free time-resolved magnetic circular dichroism with pulsed vector beams. *The Journal of Physical Chemistry Letters*, 13:11300–11306, 2022.

[226] Mina Hanifeh and Filippo Capolino. Helicity maximization in a planar array of achiral high-density dielectric nanoparticles. *J. Appl. Phys.*, 127:093104, Mar 7 2020.

[227] L. Allen, M. W. Beijersbergen, R. J. C. Spreeuw, and J. P. Woerdman. Orbital angular momentum of light and the transformation of laguerre-gaussian laser modes. *Phys. Rev. A*, 45:8185–8189, Jun 1992.

[228] Jinwei Zeng, Yajuan Dong, Yu Wang, Jinrun Zhang, and Jian Wang. Optical imaging using orbital angular momentum: Interferometry, holography and microscopy. *Journal of Lightwave Technology*, 41(7):2025–2040, 2023.

[229] Cyriaque Genet. Chiral light-chiral matter interactions: an optical force perspective. *ACS Photonics*, 9:319–332, Feb 16 2022.

[230] Oleg V. Angelsky, Aleksandr Y. Bekshaev, Steen G. Hanson, Claudia Yu Zenkova, Igor I. Mokhun, and Zheng Jun. Structured light: Ideas and concepts. *Frontiers in Physics*, 8:114, MAY 13 2020.

[231] Konstantin Y. Bliokh, Aleksandr Y. Bekshaev, and Franco Nori. Extraordinary momentum and spin in evanescent waves. *Nat. Commun*, 5:3300, MAR 2014.

[232] J Leach, M R Dennis, J Courtial, and M J Padgett. Vortex knots in light. *New Journal of Physics*, 7:55, feb 2005.

[233] L Allen and M.J Padgett. The poynting vector in laguerre–gaussian beams and the interpretation of their angular momentum density. *Optics Communications*, 184:67–71, 2000.

[234] Fiona C. Speirits and Stephen M. Barnett. Do waves carrying orbital angular momentum possess azimuthal linear momentum? *Phys. Rev. Lett.*, 111:103602, Sep 2013.

[235] Stephen M Barnett, L Allen, Robert P Cameron, Claire R Gilson, Miles J Padgett, Fiona C Speirits, and Alison M Yao. On the natures of the spin and orbital parts of optical angular momentum. *Journal of Optics*, 18:064004, apr 2016.

[236] Andrea Rubano, Filippo Cardano, Bruno Piccirillo, and Lorenzo Marcucci. Q-plate technology: a progress review. *J. Opt. Soc. Am. B-Opt. Phys.*, 36:70–87, May 2019.

[237] Andrew Forbes, Angela Dudley, and Melanie McLaren. Creation and detection of optical modes with spatial light modulators. *Adv. Opt. Photon.*, 8:200–227, Jun 2016.

[238] Peter Schemmel, Giampaolo Pisano, and Bruno Maffei. Modular spiral phase plate design for orbital angular momentum generation at millimetre wavelengths. *Opt. Express*, 22:14712–14726, Jun 2014.

[239] M.W. Beijersbergen, L. Allen, H.E.L.O. van der Veen, and J.P. Woerdman. Astigmatic laser mode converters and transfer of orbital angular momentum. *Optics Communications*, 96:123–132, 1993.

[240] MJ Padgett and L Allen. Orbital angular momentum exchange in cylindrical-lens mode converters. *J. opt., B Quantum semiclass.*, 4:S17–S19, APR 2002.

[241] Dale Green and Kayn A. Forbes. Optical chirality of vortex beams at the nanoscale. *Nanoscale*, 15:540–552, 2023.

[242] B. S. Bhargava Ram, Paramasivam Senthilkumaran, and Anurag Sharma. Polarization-based spatial filtering for directional and nondirectional edge enhancement using an s-waveplate. *Appl. Optics*, 56:3171–3178, APR 10 2017.

[243] Aidas Matijosius, Paulius Stanislovaitis, Titas Gertus, and Valerijus Smilgevicius. Formation of optical vortices with topological charge —l—=1 and —l—=1/2 by use of the s-waveplate. *Optics Communications*, 324:1–9, 2014.

[244] Theocaris Pericles S. and Gdoutos E. E. Passage of polarized light through optical elements. In *Matrix theory of photoelasticity*, chapter 4, pages 45–80. Springer-Verlag Berlin, New York City, New York, 1979.

[245] David C. Lay, Steven R. Lay, Judi J. McDonald. Linear equations in linear algebra. In *Linear Algebra and Its Applications*, chapter 1, pages 1–97. Pearson, Boston, MA, 2016.

[246] Ignacio Moreno, Jorge Albero, Jeffrey A. Davis, Don M. Cottrell, and Johnathan B. Cushing. Polarization manipulation of radially polarized beams. *Opt. Eng.*, 51:128003, DEC 2012.

[247] Manman Li, Xu Chen, Shaohui Yan, Yanan Zhang, and Baoli Yao. Enatioselective rotation of chiral particles by azimuthally polarized beams. *Advanced Photonics Research*, 3:2200117, 2022.

[248] Lisa V. Poulikakos, Jennifer A. Dionne, and Aitzol García-Etxarri. Optical helicity and optical chirality in free space and in the presence of matter. *Symmetry*, 11(9), 2019.

[249] Konstantin Y Bliokh, Aleksandr Y Bekshaev, and Franco Nori. Dual electromagnetism: helicity, spin, momentum and angular momentum. *New Journal of Physics*, 15(3):033026, Mar 2013.

[250] Ivan Fernandez-Corbaton and Gabriel Molina-Terriza. *Introduction to Helicity and Electromagnetic Duality Transformations in Optics*, chapter 11, pages 341–362. John Wiley & Sons, Ltd, 2015.

[251] John Lekner. Chirality of self-dual electromagnetic beams. *Journal of Optics*, 21(3):035402, Feb 2019.

[252] Albert Herrero-Parareda and Filippo Capolino. The combination of the azimuthally and radially polarized beams: Helicity and momentum densities, generation, and optimal chiral light. *Advanced Photonics Research*, 5:2300265, 2024.

[253] John Lekner. Self-dual electromagnetic fields. *Proceedings of the Royal Society A: Mathematical, Physical and Engineering Sciences*, 480:20230657, 2024.

[254] Albert Herrero-Parareda and Filippo Capolino. Optimally chiral optical trapping. In Kishan Dholakia and Gabriel C. Spalding, editors, *Optical Trapping and Optical Micromanipulation XX*, volume 12649, page 126490G. International Society for Optics and Photonics, SPIE, 2023.

[255] Georgiy Tkachenko and Etienne Brasselet. Helicity-dependent three-dimensional optical trapping of chiral microparticles. *Nat. Commun.*, 5:4491, JUL 2014.

[256] David S. Bradshaw, Kayn A. Forbes, Jamie M. Leeder, and David L. Andrews. Chirality in optical trapping and optical binding. *Photonics*, 2:483–497, JUN 2015.

[257] Tianhang Zhang, Mahdy Rahman Chowdhury Mahdy, Yongmin Liu, Jing Hua Teng, Chwee Teck Lim, Zheng Wang, and Cheng-Wei Qiu. All-optical chirality-sensitive sorting via reversible lateral forces in interference fields. *Acs Nano*, 11(4):4292–4300, Apr 2017.

[258] Nicolas Perez and Daryl Preece. Enhanced optical vector bottle beams with obscured nodal surfaces. *Opt. Express*, 32(8):14010–14017, Apr 2024.

[259] Jungho Mun and Junsuk Rho. Importance of higher-order multipole transitions on chiral nearfield interactions. *Nanophotonics*, 8(5):941–948, 2019.

[260] D. Cojoc, S. Cabrini, E. Ferrari, R. Malureanu, M.B. Danailov, and E. Di Fabrizio. Dynamic multiple optical trapping by means of diffractive optical elements. *Microelectronic Engineering*, 73-74:927–932, 2004.

[261] James S. Bennett, Lachlan J. Gibson, Rory M. Kelly, Emmanuel Brousse, Bastian Baudisch, Daryl Preece, Timo A. Nieminen, Timothy Nicholson, Norman R. Heckenberg, and Halina Rubinsztein-Dunlop. Spatially-resolved rotational microrheology with an optically-trapped sphere. *Scientific Reports*, 3:1759, May 2013.

[262] Ram Nandan Kumar, Jeeban Kumar Nayak, Subhasish Dutta Gupta, Nirmalya Ghosh, and Ayan Banerjee. Probing dual asymmetric transverse spin angular momentum in tightly focused vector beams in optical tweezers. *Laser & Photonics Reviews*, 18:2300189, 2024.

[263] Alexander B. Stilgoe, Anatolii V. Kashchuk, Daryl Preece, and Halina Rubinsztein-Dunlop. An interpretation and guide to single-pass beam shaping methods using slms and dmds. *Journal of Optics*, 18(6):065609, Jun 2016.

[264] J. Liesener, M. Reicherter, T. Haist, and H.J. Tiziani. Multi-functional optical tweezers using computer-generated holograms. *Optics Communications*, 185(1):77–82, Sep 2000.

[265] Daryl Preece, Stephen Keen, Elliot Botvinick, Richard Bowman, Miles Padgett, and Jonathan Leach. Independent polarisation control of multiple optical traps. *Opt. Express*, 16(20):15897–15902, Sep 2008.

[266] Melvin Lax, William H. Louisell, and William B. McKnight. From maxwell to paraxial wave optics. *Phys. Rev. A*, 11:1365–1370, Apr 1975.

[267] W. H. McMaster. Polarization and the stokes parameters. *American Journal of Physics*, 22:351–362, 1954.

[268] H. G. Berry, G. Gabrielse, and A. E. Livingston. Measurement of the stokes parameters of light. *Appl. Opt.*, 16(12):3200–3205, Dec 1977.

[269] Irshaad Fatadin, David Ives, and Martin Wicks. Accurate magnified near-field measurement of optical waveguides using a calibrated ccd camera. *J. Lightwave Technol.*, 24(12):5067–5074, Dec 2006.

[270] Rongqing Hui and Maurice O'Sullivan. Basic instrumentation for optical measurement. In Rongqing Hui and Maurice O'Sullivan, editors, *Fiber Optic Measurement Techniques*, chapter 2, pages 129–258. Academic Press, Boston, 2009.

[271] M Born and E Wolf. Basic properties of the electromagnetic field. In *Principles of Optics: Electromagnetic Theory of Propagation, Interference and Diffraction of Light*, chapter 1, pages 1–6. Cambridge University Press, 1999.

[272] Chandroth P. Jisha and Alessandro Alberucci. Paraxial light beams in structured anisotropic media. *Journal of the Optical Society of America A: Optics, Image Science, and Vision*, 34(11):2019–2024, Nov 2017.

[273] Hans Moosmüller and W. Patrick Arnott. Particle optics in the rayleigh regime. *Journal of the Air & Waste Management Association*, 59(9):1028–1031, 2009.